Title

NON-INVASIVE MEASUREMENTS OF MUSCLE MICROSTRUCTURE USING DIFFUSION TENSOR IMAGING IN ACTIVE-DUTY MARINES

Author

Berry, David Barnes

Publication Date

2017

Peer reviewed|Thesis/dissertation

UNIVERSITY OF CALIFORNIA, SAN DIEGO

NON-INVASIVE MEASUREMENTS OF MUSCLE MICROSTRUCTURE USING DIFFUSION TENSOR IMAGING IN ACTIVE-DUTY MARINES

A dissertation submitted in partial satisfaction of the

requirements for the degree Doctor of Philosophy

in

Bioengineering

by

David Barnes Berry

Committee in charge:

Professor Samuel R. Ward, Chair
Professor Robert L. Sah, Co-Chair
Professor Shaochen Chen
Professor Lawrence Frank
Professor Andrew McCulloch

2017

The dissertation of David Barnes Berry is approved, and it is acceptable in quality and form for publication on microfilm and electronically:

_____

_____

_____

_____
Co-Chair

_____
Chair

University of California, San Diego

2017

DEDICATION

For my grandparents Michael and Bernice Messinger, Merle and Phyllis Berry. Thank you for your unwavering unconditional love and support.

EPIGRAPH

If we knew what it was we were doing, it wouldn't be called 'research,' would it?

-Albert Einstein

TABLE OF CONTENTS

LIST OF ABBREVIATIONS

ANOVA	Analysis of Variance
BMI	Body Mass Index
DLP	Digital Light Procession
DMD	Digital Micromirror Device
DT	Diffusion Tensor
DTI	Diffusion Tensor Imaging
ECM	Extracellular Matrix
FA	Fractional Anisotropy
FLASH	Fast Low Angle Shot
IVD	Intervertebral Disc
LAP	Lithium Phenyl-2,4,6-trimethylbenzoylphosphinate
LBP	Low Back Pain
LS	Lumbar Spine
MD	Mean Diffusivity
MRI	Magnetic Resonance Imaging
PBS	Phosphate Buffered Saline
PCA	Principle Components Analysis
PEG-DA	Polyethylene Glycol Diacrylate
T2	Transverse Relaxation
UV	Ultraviolet

LIST OF TABLES

LIST OF FIGURES

ACKNOWLEDGMENTS

During my time in graduate school, I have been fortunate to be supported by a number of individuals who have contributed to my development as a scientist, and as a person. Thank you Sam Ward, your mentorship has driven me to self motivate, be creative, and think critically about the big picture, inside and outside of the laboratory. I am also grateful for the guidance and teaching from Larry Frank and Shaochen Chen. I would also like to acknowledge the members of the Ward Lab who have helped me over the years: Ana Rodriguez-Soto, who taught me so much about mentorship, and how to be successful in endeavors inside and outside academia, Michael Gibbons for letting me bounce ideas off you at any time, helping me hone my ideas and enjoy my time in graduate school, and Bahar Shahidi thank you for helping me keep my questions clinically relevant and always making me laugh when things got stressful. Finally, I would like to thank my fiancé Barbara Williams and my family Sam, Debra, and Peter Berry for all their love, support and believing in me throughout this process.

Chapter 2 is a reprint of the published article, "Lumbar spine postures in Marines during simulated operational positions." Berry DB, Rodriguez-Soto AE, Su J, Gombatto SP, Shahidi B, Palombo L, Chung C, Jensen A, Kelly KR, Ward SR. *Journal of Orthopaedic Surgery,* [E pub ahead of print], 2017. The dissertation author was the primary investigator and author of this paper.

Chapter 3, in full, is currently being prepared for submission for the publication of the material as it may appear in the Journal of Orthopaedic and Sports Physical Therapy, 2017, Berry DB, Shahidi B, Rodriguez-Soto AE, Hughes-Austin JM, Kelly KR, Ward SR. The dissertation author was the primary investigator and author of this paper.

Chapter 4, in full, is currently submitted for the publication of the material as it may appear in the Journal of Magnetic Resonance Imaging in Medicine, 2017, Berry DB,

Regner BM, Gallinsky V, Ward SR, Frank LF. The dissertation author was the primary investigator and author of this paper.

Chapter 5 is a reprint of the published article, “A 3D tissue-printing approach for validation of diffusion tensor imaging in skeletal muscle.” Berry DB, You S, Warner J, Chen S, Ward SR. *Tissue Engineering: Part A,* [E pub ahead of print], 2017. The dissertation author was the primary investigator and author of this paper.

VITA

2012	B.S. in Biomedical Engineering, *cum laude* Boston University, Boston, Massachusetts
2015	M.S., Bioengineering University of California, San Diego, La Jolla, California
2017	Ph.D., Bioengineering University of California, San Diego, La Jolla, California

Teaching Experience

University of California, San Diego
Biomedical Optics and Imaging
Principles of Biomaterials Design
Senior Design

Journal Articles

Unnikrishnan GU, Barest G, Berry DB, Hussein AI, Morgan EF. **Effect of specimen-specific anisotropic material models in QCT-based finite element analysis of vertebra.** *Journal of Biomechanical Engineering*, 2013; 135(10).

Berry DB, Rodriguez-Soto AE, Tokunaga JR, Gombatto SP, Ward SR. **An endplate based joint coordinate system for measuring kinematics in normal and abnormally-shaped lumbar vertebrae.** *Journal of Applied Biomechanics,* 2015: 31(6).

Rodriguez-Soto AE, Berry DB, Palombo L, Kelly KR, Ward SR. **The effect of load magnitude and distribution on lumbar spine posture in active-duty Marines.** *Spine.* 2016.

Rodriguez-Soto AE, Berry DB, Jaworski R, Jensen A, Chung CB, Niederburger B, Qadir A, Kelly KR, Ward SR. **The effect of training on lumbar spine kinematics and intervertebral disc degeneration in active-duty Marines**. *Ergonomics.* 2016.

Shahidi BS, Parra CL, Berry DB, Hubbard JC, Gombatto SP, Garfin S, Ward SR. **Contribution of low back pain and age on lumbar spine muscle size and fatty infiltration.** *Spine.* 2016.

Berry DB, Rodriguez-Soto AE, Su J, Gombatto SP, Shahidi B, Palombo L, Chung C, Kelly KR, Ward SR. **Lumbar spine postures in Marines during simulated operational positions.** Journal of Orthopaedic Surgery. 2017.

Berry DB, You S, Warner J, Frank LF, Chen S, Ward SR. **A 3D tissue-printing approach for validation of diffusion tensor imaging in skeletal muscle.** *Tissue Engineering: Part A.* 2017.

Berry DB, Regner BM, Gallinsky V, Ward SR, Frank LF. **The relationships between microstructure and the diffusion tensor in simulated skeletal muscle.** *Submitted: Magnetic Resonance Imaging in Medicine.*

Berry DB, Shahidi B, Rodriguez-Soto AE, Hughes-Austin J, Ward SR. **The relationship between skeletal muscle kinematics and muscle physiology in active duty Marines.** *In preparation.*

Onodera K, Berry DB, Shahidi B, Kelly KR, Ward SR. **Intervertebral disc fragment kinematics in active-duty Marines with and without lumbar spine pathology.** *In preparation*.

Hernandez A, Berry DB, Ward SR, Gombatto SP. **Lumbar spine kinematics assessed by motion capture and upright MRI.** *In preparation.*

Rodriguez-Soto AE, Berry DB, Fithian A, Gibbons M, Singh A, Ward SR. **Diffusion tensor imaging of the human shoulder.** *In preparation.*

Selected Conference Abstracts

Unnikrishnan, GU, Barest, CD, Berry, DB, Hussein, AI, Morgan, EF. **Influence of specimen specific trabecular anisotropy on QCT-based finite element analyses of lumbar vertebra**. ASME Summer Bioengineering Conference, Puerto Rico, 2012.

Berry DB, Rodriguez-Soto AE, Gombatto SP, Jaworski R, Kelly KR, Ward SR. **Lumbar spine postures in Marines during simulated operational conditions.** Word Congress of Biomechanics, Boston, 2014.

Berry DB, Rodriguez-Soto AE, Gombatto SP, Jaworski R, Kelly KR, Ward SR. **Lumbar spine postures in Marines during simulated operational conditions.** Military Health System Research Symposium, Ft. Lauderdale, 2014. *Honorable Mention*.

Berry DB, Rodriguez-Soto AE, Tokunaga JR, Gombatto SP, Ward SR. **An endplate-based joint coordinate system for measuring kinematics in normal and abnormally shaped lumbar vertebrae**. Orthopaedic Research Society, Las Vegas, 2015.

Rubin JL, Berry DB, Ward SR, Gombatto SP. **Lumbar spine kinematics for end-range trunk positions on healthy individuals using upright MRI**. American Society of Biomechanics, Cincinnati, 2015.

Rodriguez-Soto AE, Berry DB, Palombo L, Valaik E, Kelly KR, Ward SR. **The effect of load magnitude and distribution on lumbar spine posture in active-duty Marines**. American Society of Biomechanics, Cincinnati, 2015.

Rodriguez-Soto AE, Stambaugh JR, Su J, Berry DB, Gombatto SP, Kelly KR, Ward SR. **Spinal muscle quality changes in physically active individuals with disc degeneration.** Orthopaedic Research Society, Las Vegas, 2015.

Berry DB, Regner B, Gallinsky V, Frank LR, Ward, SR. **The relationships between microstructure and the diffusion tensor in simulated skeletal muscle**. International Society for Magnetic Resonance in Imaging, Singapore, 2016.

Stambaugh JR, Rodriguez-Soto AE, Berry DB, Parra C, Gombatto SP, Palombo L, Kelly KR, Ward SR. **Structural adaptations of paraspinal musculature in active-duty Marines with intervertebral disc degeneration.** Military Orthopedic Surgeon Society, Olympic Valley, 2016.

Shahidi BJ, Parra C, Berry DB, Ward SR. **Age-related changes in lumbar spine muscle cross sectional area and fatty infiltration in individuals with low back pain**. American Physical Therapy Association, San Antonio, 2017

Berry DB, Rodriguez-Soto AE, Parra C, Stambaugh J, Valaik E, Chung C, Ward SR. **Noninvasive Assessment of Lumbar Muscle Architecture in Active-Duty Marines**. Orthopaedic Research Society Meeting, San Diego, 2017.

Berry DB, Rodriguez-Soto AE, Gombatto S, Shahidi B, Chung C, Ward SR. **Lumbar Spine Postures in Marines During Simulated Operational Positions.** Orthopaedic Research Society Meeting, San Diego, 2017.

Parra C, Berry DB, Shahidi B, Ward SR, Deane KD, Hughes-Austin JM. **Thoracic spine muscle quality and bone mineral density in a population at risk for Rheumatoid Arthritis.** UCSD Public Health Research Day, San Diego, 2017.

Berry DB, You S, Warner J, Frank LR, Chen S, Ward SR. **Quantitation of DTI changes associated with muscle injury using a 3D printed phantom.** International Society for Magnetic Resonance in Imaging, Honolulu, 2017.

Berry DB, Shahidi B, Rodriguez-Soto AE, Hughes-Austin J, Kelly KR, Ward SR. **Lumbar muscle structure predicts operational postures in active duty Marines.** International Society of Biomechanics, Brisbane, 2017.

ABSTRACT OF THE DISSERTATION

NON-INVASIVE MEASUREMENTS OF MUSCLE MICROSTRUCTURE USING DIFFUSION TENSOR IMAGING IN ACTIVE-DUTY MARINES

by

David Barnes Berry

Doctor of Philosophy in Bioengineering

University of California, San Diego, 2017

Professor Samuel R. Ward, Chair
Professor Robert L. Sah, Co-Chair

Low back pain (LBP) is a common musculoskeletal complaint, and is a particularly large problem in the military. Heavy load carriage and unusual postures military members operate under in training and in combat have been implicated as primary causes of LBP. The muscles of the lumbar spine (LS) are crucial for providing stability and maintaining posture; lumbar instability is associated with chronic LBP and can result in injury. With injury and age, degenerative structural changes in muscle tissue are observed in concert with gross alterations in posture, however the relationship between muscle microstructure and posture isn't well understood. The purpose of these

studies was to investigate the predictive capacity of muscle structure on LS posture in active-duty Marines under operationally relevant conditions. Fractional anisotropy, a measure of muscle microstructure made with diffusion tensor imaging (DTI), was found to be a key predictor of LS posture. Trying to translate these findings to physiologic measures of muscle, it became evident that DTI is nonspecific to individual features of muscle microstructure. To address this gap in our understanding of skeletal muscle DTI's capacity to non-invasively quantify muscle microstructure, we sought to establish an accurate and precise, DTI based tool to measure individual components of muscle microstructure. To achieve this goal we used *in silico*-based simulation to create a theoretical framework between DTI and key features of muscle microstructure. A precision engineered, nano-fabricated diffusion phantom was developed and tested to validate this framework in real world experiments. The main findings from these studies were the DT is most sensitive to fiber size under 60μm diameter. Using this framework to interpret the relationship between muscle microstructure and posture, Marines with smaller muscle fibers in the erector spinae muscle group have decreased lumbar lordosis, decreased lumbar extension and decreased sacral slope. Clinically and operationally, these findings are significant because they provide the framework for a non-invasive tool that can be used to measure and predict maladaptive posture in operational conditions from musculoskeletal health, which could allow clinicians to tailor rehabilitation protocols to prevent injury, and potentially be used to predict an individual's risk for LS injury.

CHAPTER 1: INTRODUCTION

1.1 Low back pain in military members

Low back pain (LBP) is one of the most common musculoskeletal complaints, affecting 65%-85% of the general population [1]. LBP is a particularly large problem in the military; in 2013 there were more military medical encounters were due to low back pain than any other major medical condition (975,000) [2]. This yields a large financial burden on the Department of Defense and the Veterans Administration to provide health care to these individuals, costing over $2 billion annually [3, 4]. One of the main causes attributed to the development of LBP in military members is heavy load carriage and unusual postures experienced in training, and in combat [5, 6].

Military members routinely operate under loads exceeding load carriage limit recommendations. The kinematic behavior of the lumbar spine under heavy load carriage has recently been studied by Rodriguez-Soto in active-duty Marines. Under heavy load (50.8kg), decreased lumbar lordosis and increased lumbar flexion was observed, which is not further exacerbated by the duration of load or physical activity (e.g. marching) [7]. By changing the distribution of load to a 50%/50% anterior/posterior configuration, it is possible to reverse postural changes resulting from load [8]. However, the relationship between posture and risk of lumbar injury or LBP is unknown. It has been postulated that increased lordosis and increased lumbosacral flexion results in increased shear forces at the lower lumbar levels, which may lead to injury [9].

LBP can be idiopathic, or due to structural abnormalities virtually anywhere in the spinal column. One of the most common structural pathologies associated with LBP is

intervertebral disc (IVD) degeneration. The IVD is a fibrocartilagenous joint that lies between two adjacent vertebrae, which serves to transfer load from superior to inferior vertebral segments, and acts as a shock absorber for the spine. The IVD is composed of collagenous rings, called the annulus fibrosis, which surrounds a gel like, hydrated tissue called the nucleus pulposus (Figure 1). LBP is commonly related to IVD injury due to its proximity to the spinal cord. Common modes of IVD injury include disc herniation, where the disc protrudes into the vertebral and/or lateral foramen and compresses on the spinal cord or exiting peripheral nerve roots, or disc degeneration, which results in loss of disc height, which can also irritate the nerve roots. The origin of LBP in people with pathology can sometimes be traced to structural abnormalities that mechanically perturb the spinal cord or exiting peripheral nerves. However, pain can also arise from other structures of the spine including the innervated portions of the annulus fibrosis, facet joints, posterior lumbar musculature and surrounding ligaments.

1.2 Maintaining stability of the lumbar spine

The muscles of the lumbar spine are crucial for providing stability and supporting the spine [10]. Lumbar instability is associated with chronic LBP and can result in injury [11-13]. The multifidus muscle is considered the primary stabilizer of the lumbar spine because of its capacity to generate high force over a small fiber length [10]. With injury and age, muscle atrophy, replacement of muscle tissue with adipose and fibrotic tissue is typically observed (Figure 2) [14, 15]. This process decreases the volume fraction of functional contractile tissue within the muscle, which can result in decreased lumbar spine, and therefore, intervertebral joint stability.

The microstructure of muscle is closely related to its performance capacity. For example, larger muscle fibers can produce greater contractile forces, while elevated extra-cellular matrix concentrations (fibrosis) result in increased passive stiffness [9, 15, 16]. Changes in muscle microstructure are typically assessed with histology, which is highly invasive, destructive to the tissue, and requires biopsy or excision in human and animal subjects, which complicates longitudinal examination of disease and recovery. Therefore, most studies of lumbar spine pathology are limited to cadaver or animal models. Noninvasive clinical assessment of lumbar muscle has been limited to techniques such as ultrasound [16], computed tomography [6], and magnetic resonance imaging (MRI) [7]. Ultrasound is of limited utility as it is only sensitive to changes in muscle cross sectional area, and has relatively low spatial resolution. Computer tomography has excellent 3D resolution and is sensitive to muscle volume and fat distributions, however this technique involves harmful ionizing radiation and does not provide great contract between soft tissues in the spine. Of these techniques, MRI provides the best contrast of soft tissues in the lumbar spine and has been shown to be sensitive to measuring muscle volume, fat fraction, fibrotic tissue deposition and restricted diffusion profiles, thought to be related to muscle microstructure.

1.3 Fundamentals of MR Imaging

MRI is a powerful tool, which can be used to image the soft tissues of the body non-invasively and without harmful ionizing radiation. The basic principles of most forms of clinical MRI revolve around nuclear magnetic resonance in the hydrogen molecule. Within the nucleus of a hydrogen molecule is a single proton, which has an

intrinsic angular momentum (*J*), referred to as spin. The angular momentum of a proton is equal to $J = \hbar I$ where I is the spin angular momentum quantum number which equals ±½ for a proton (known as spin-up or spin-down) and $\hbar$ is Planks constant. Fundamental principles of electromagnetism dictate that charged, spinning particles generate a very small magnetic fields, and thus have a magnetic dipole moment (μ). In the presence of a larger magnetic field, such as an MRI scanner, the poles of this magnetic dipole moment will align. Due to it's angular momentum, a proton will precess about the main axis of an external magnetic field at a certain angular frequency known as the Larmour frequency: $\omega = -\gamma B_0$ where B_0 is the magnetic field strength and γ is constant called the gyromagnetic ratio and is equal to $\frac{\mu}{J}$. The gyromagnetic ratio is dependent upon chemical species and for hydrogen equals $2.7*10^8$ rad*s^{-1}*T^{-1}. Therefore, the angular frequency at which a proton precesses is dependent upon both the chemical species of the proton, and the strength of the main magnetic field.

The human body is made up roughly of 70% water, and made up of many trillions of water molecules, which contain 2 protons each. Due to the duplicity of water in the human body, when performing an MRI experiment, the net magnetization of water-bound protons in a tissue is considered rather than on an individual particle level. In the presence of no external magnetic field, the net magnetization of protons molecules within a voxel (three dimensional space over which a MRI experiment may take place) is equal to zero. When a magnetic field is applied, protons can be aligned in one of two directions: parallel to the magnetic field or anti-parallel to the magnetic field, also known as spin-up or spin-down (Figure 3). While both energy states are stable, the spin-down direction requires slightly more energy than the spin-up direction. As net magnetization is

dependent upon the total magnetization of protons pointing up and down, and is a key metric in resolving MRI signal, it is important to understand what factors influence net magnetization.

The net magnetization will lie along the direction of the main magnetic field (z-axis) unless it is perturbed. It is possible to tip the net magnetization vector orthogonal to the z-axis into the x-y-axis of the MR scanner by applying energy in the form of a 90° radiofrequency pulse. After the pulse is applied, the net magnetization vector returns back to it original energy state, releasing energy in the form of radiofrequency waves. The radiofrequency waves can be measured by the small currents they induce in receiver coils. Radiofrequency waves are transmitted at an inherent phase and frequency, which can be modulated by applying magnetic field gradients across an imaging plane. By applying magnetic field gradients at a specific time after the original 90° radiofrequency pulse, it is possible to spatially encode the signal into k-space, a matrix describing the frequency distribution of a signal in 2D. By applying an inverse Fourier Transform to the k-space data, a classic MR Image is formed (Figure 4).

1.4 Fundamentals of Diffusion Tensor Imaging

Diffusion tensor imaging is a version of magnetic resonance imaging that is sensitive to the restricted diffusion of water. In order to understand diffusion tensor imaging, it is first necessary to understand the basic principles of diffusion. Diffusion in fluids occurs as a result of the random motion of particles colliding with each other, called Brownian motion. Robert Brown is credited with the discovery of this phenomenon in 1827, after observing particles of organic and inorganic materials

randomly moving around on the surface of water. In 1905, Albert Einstein described a mathematic framework for describing how particles diffuse and proposed that the mean square displacement of motion a particle can undergo is:

$$\overline{x^2} = 2Dt$$

where D is the diffusion coefficient and t is time [21]. Given as a 1D problem, if some number of water molecules at the same location x=0 were released, statistically, they would begin to move away from the origin in a characteristic bell-shaped curve (Figure 5). If a water molecule reaches an impenetrable barrier, it will reflect back away from the barrier (Figure 5). Given the same problem in 3D, if water molecules are released at a definite point in space, they are free to diffuse in any direction away from the origin (Figure 6). However, if they reach a barrier, their diffusion along that direction will be hindered (Figure 6).

Muscle is a highly organized hierarchical structure, containing layers of column-like muscle fibers, wrapped in layers of connective tissue. Water molecules diffusing within a muscle fiber are generally unable to pass through the sarcolemma (cell wall) of a muscle fiber, and therefore are more likely to diffuse further longitudinally rather than radially across a muscle fiber. Diffusion tensor imaging is an MRI technique able to measure the restricted diffusion profile of water in muscle fibers.

The basic diffusion tensor imaging sequence is a diffusion-weighted, spin-echo echo planar imaging sequence. In a spin-echo pulse sequence, first a 90° radiofrequency pulse is applied to nutate the orientation of the net magnetic vector out of the z-axis and into the x-y axis. As the vector relaxes back into the z-axis, the x-y component of the vector quickly decays, due to phase incoherence arising from inhomogeneities in the

magnetic field. In order to resolve the x-y component of the vector, at a time t after the original pulse, a 180° radiofrequency pulse, also known as a refocusing pulse, can be applied. Then, the x-y vector will refocus at 2*t which is referred to as the echo time (TE). Several additional 180° radiofrequency pulses can be applied at equal TE's after the original excitation in order to measure the transverse relaxation time (T2 relaxation) within a voxel (Figure 7). At the echo time, phase and frequency encoding occurs to spatially encode the MR signal. In diffusion tensor imaging, the only difference from a spin-echo pulse sequence is that magnetic gradients of equal duration and strength are applied on either side of the 180° refocusing pulse (Figure 8). Water particles that move along the direction of the diffusion gradients will be dephased by the first gradient, and will not be rephrased by the second, resulting in signal loss. However, water molecules moving orthogonal to the diffusion gradient will be dephased by the first and rephrased by the second gradient, resulting in a strong overall measured signal. This behavior was mathematically described by Stejskal and Tanner as:

$$S_i = S_0 e^{-bD_i}$$

where S is the measured signal along a diffusion direction (i) or with no diffusion encoding gradients (0), b is a quantitative measure of the strength of the diffusion gradients and D_i is the measured diffusion coefficient along a diffusion direction [22]. From this equation, it is evident that large measured diffusion coefficients (less restricted diffusion) are coincident with relative signal loss and vice-versa.

Several parameters are of important note when performing a diffusion tensor imaging experiment. First, the b-value describes the strength of diffusion-weighting in the experiment, and is equal to:

$$b = \gamma^2 G^2 \delta^2 (\Delta - \frac{\delta}{3})$$

where G is the magnitude of the diffusion gradient, δ is the duration of the diffusion gradient, and Δ is the separation between diffusion gradients before and after the 180° refocusing pulse (Figure 8). The optimal choice of b-value is dependent on the tissue being scanned, the magnetic field strength, and the allowable duration of scan time. Typically, in skeletal muscle, a b-value of 500 s/mm^2 is selected due to the short T2 relaxation time of muscle [23, 24]. However, in tissues such as nerve, b-values of 1000 s/mm^2 or greater are not uncommon as they have longer T2 relaxation rates. Another key factor that muscle be chosen when performing a diffusion tensor imaging experiment is the number of diffusion encoding directions that are chosen. The minimum number of diffusion directions that is required for a 2nd rank tensor is 6. However, by increasing the number of diffusion directions, restricted diffusion is sampled more, which provides a more accurate estimation of the diffusion tensor.

The quantitative output of DTI is a second order tensor, with eigenvalues describing the magnitude of diffusion along their respective eigenvectors. The primary eigenvalue (λ1) describes diffusion along the primary axis of muscle fibers, and the second and third eigenvalues (λ2, λ3) describe diffusion orthogonal to λ1. Additionally, the mean diffusivity (MD) is the average of the eigenvalues and describes average diffusion, and the fractional anisotropy (FA) is the variance of the eigenvalues and describes diffusion anisotropy from 0 (perfectly isotropic) to 1 (perfectly anisotropic). The sarcolemma is thought to be the main barrier to diffusion, and therefore diffusion is greater longitudinally (λ1) than radially (λ2, λ3) across muscle fibers [25, 26]. Additionally,

the diffusion tensor can be used to generate tractography images of tissues, which can be used to approximate fiber bundle length (Figure 9).

1.5 Diffusion Tensor Imaging in Skeletal Muscle

Although DTI is often used to study muscle structure/physiology and pathology, it is sensitive, but not specific to changes in muscle microstructure, and thus remains of limited clinical utility. In order to interpret how the diffusion tensor is related to microstructure and how injury influences diffusion, it is necessary to understand the underlying anatomy and physiology. Skeletal muscle microstructure is hierarchical with both cellular and extra-cellular components playing some role in active and/or passive force generating capacities [18, 27, 28]. Muscle fiber area and isometric force are directly related, and therefore, quantifying fiber area allows for a prediction of isometric active force generating capacity [29]. As $\lambda 2$ and $\lambda 3$ describe radial diffusion orthogonal to the main direction of a muscle fiber, it follows that they are sensitive to fiber size and shape. To explain differences between $\lambda 2$ and $\lambda 3$, Karampinos et al. simulated diffusion experiments on muscle fibers approximated as elliptical cylinders of infinite length [30]. The results indicate that cross-sectional shape only partially explains the difference between $\lambda 2$ and $\lambda 3$. To investigate the effect of increasing or decreasing fiber diameter *in vivo*, studies have looked at diffusion changes in lengthened and shortened plantar flexor muscles. In these studies, FA and MD changed in predictable ways, but fiber areas were never directly measured [31-38]. In addition to the lack of a rigorous control values, the magnitude of fiber size changes required to detect diffusion changes is unknown. In a study comparing plantar flexor muscles before and after exercise in subjects with chronic

exertional compartment syndrome and in healthy volunteers, Sigmund et al. [39] used DTI data in a random permeable barrier model to measure MD and estimate fiber diameter, and fiber permeability. Both volunteers and patients experienced an increase in MD. In healthy volunteers, increased fiber diameter was assumed to be the reason for increased MD, while in patients with compartment syndrome, an increase in permeability was thought to be the reason for increased MD. Similarly, in a mouse model of Duchene muscular dystrophy, after a series of eccentric contractions an increase in Evans blue dye positive fibers was observed, which indicates sarcolemma damage and permeability, consistent with an increase in the MD and decrease in FA [40]. Therefore, the size, shape and integrity of the sarcolemma also appear to influence the diffusion signal, but their relative contributions are unknown. These data highlight non-specificity and the types of assumptions that are made when interpreting DTI data. As an illustration of this lack of specificity, DTI is not routinely used to diagnose, or even track, disease progression in humans or animal models. For example, patients with myositis often undergo open or needle biopsy to make differential diagnoses of polymyositis, inclusion body myositis, or dermatomyositis. Key histopathologic features are; presence and location of inflammation and the presence/extent of degeneration [41]. Polymyositis and inclusion body myositis tend to have intracellular inflammation and degeneration [42-44] and dermatomyositis tends to have perimysial inflammation [45]. Importantly, the treatment strategy for these patients is different, so serial biopsies would be ideal, but not used because they are invasive and can be painful. As such, a sensitive and specific imaging tool would have a profound impact on these patients, and on animal research directed at understanding and treating neuromuscular diseases.

Extra-cellular components of muscle are also affected by injury, and must be considered in the interpretation of the diffusion tensor. For example, immediately after exercise, a decrease in FA and an increase in MD are observed [39, 40, 46-48]. In addition to changes in the permeability of the sarcolemma and size of fibers, these diffusion changes have been attributed to increases in T2, and increased signal to noise ratios, secondary to increased extra-cellular fluid volume. Non-diffusion, MR-relaxometry experiments can uncover these edema-related fluid shifts [49-52], but they are unable to quantify microstructural changes that indicate disease. When muscle is denervated, acute edema is observed, followed by a decrease in fiber area, and a chronic increase in fibrosis [53]. In this case, although fiber area is decreased, a decrease in FA and an increase in MD are observed. However, in chronic denervation when edema has subsided, increased FA and decreased MD are observed, which is consistent with fiber atrophy. This suggests that edema is a major component of the measured diffusion signal in acutely denervated muscle. In fibrotic cardiac muscle, a positive correlation has been found between collagen content and MD [54]. However, the increase in MD may also be due to increased T2 relaxation [55]. In summary, it is evident that changes in the extra-cellular microstructure of muscle must also be understood if DTI data is to be correctly interpreted.

In nearly all diffusion studies of injured muscle, single-echo DTI is used, which does not account for the increased signal from extra-cellular diffusion, biasing interpretation of muscle microstructure [39, 46, 56]. A few groups have studied combining relaxometry and diffusion imaging into a multi-echo DTI acquisition [50, 57, 58]. Ababneh et al. [57] demonstrated bi-exponential analysis could be used to separate and quantify the

diffusion signal from short and long T2 components in a phantom. Fan et al. [59] used a multi-echo DTI sequence and a two-compartment description of diffusion to separate intra- and extra-cellular compartments in a rat model of acute muscle edema induced by an injection of λ-carrageenan. In models of chronic edema, single compartment models of diffusion find an increase in MD and no change in FA, regardless of underlying fiber atrophy [49, 60]. This suggests extra-cellular diffusion is dominating the diffusion signal when there is increased extra-cellular water volume fraction, due to the increase in long T2 relaxation species in the muscle. While the intra- and extra-cellular diffusion model afforded by multi-echo DTI is reasonable, its effectiveness in separating edema from other muscle microstructural changes is unknown. However, even if multi-echo DTI can be proven to separate edema from other muscle microstructural changes in the body, the relationship of the diffusion tensor to individual features of muscle microstructure (i.e. fiber size, fibrosis, and fiber integrity) is currently poorly defined.

1.6 Questions currently unanswered by the literature

Marines have much higher reported rates of low back pain than civilians [61], thought to be related to load carriage and positions military members are required to hold in training and in combat [5, 6]. In particular, it is currently unknown how the effect of operationally relevant positions under minimum operationally relevant load is related to lumbar spine posture in Marines with or without LBP or IVD degeneration. Understanding this relationship has the potential to provide the framework for possible postural interventions aimed at reducing LBP, and perhaps, risk factors for LBP in Marines during operational tasks. Currently, it is believed that there is some relationship

between low back pain, intervertebral disc health, and muscle quality in maintaining lumbar posture. A non-invasive tool that can be used to measure and predict maladaptive posture in operational conditions from musculoskeletal health would allow clinicians to tailor rehabilitation protocols to prevent injury, and could potentially be used to predict individuals at risk for lumbar spine injury. MRI has been used as a non-invasive tool to measure muscle volume, muscle fat fraction, muscle microstructure, IVD health and lumbar posture individually, and therefore has the potential to be used to solve this problem.

As muscle is considered the main stabilizer of lumbar posture, the ability to noninvasively monitor muscle health is of interest. DTI has been proposed as a noninvasive MRI technique capable of monitoring changes in muscle microstructure associated with injury, pathology, or recovery. Many studies have used DTI to measure changes in diffusion in injured skeletal muscle, and have theorized how microstructure relates to the diffusion model [24, 32, 62]. However, these relationships have never been explicitly tested nor carefully validated because the necessary experiments are complicated and difficult to rigorously control. In order to validate DTI as a tool to measure muscle microstructure it is necessary to describe, with a series of highly controlled experiments, the direct relationship between muscle microstructure and anisotropic diffusion of water, assessed by DTI. These contributions would be significant as they will shed light onto the complex relationships between the diffusion of water in muscle and the underlying muscle microstructure. These data can yield a more contemporary framework for relating DTI to muscle injury and repair.

Therefore, the aims of this dissertation are:

1. To compare differences in lumbar spine posture in operationally relevant conditions in Marines with and without intervertebral disc degeneration and with and without low back pain.
2. To investigate the predictive capacity of muscle structure, IVD health and anthropometric measures on lumbar spine posture in active duty Marines
3. To compare the ability of single- vs. multi-echo DTI to measure simulated intra- and extra-cellular muscle microstructural changes associated with injury.
4. To relate and uncouple individual microstructural changes in a precision engineering phantom of muscle injury to the diffusion tensor in high-field strength MRI experiments.

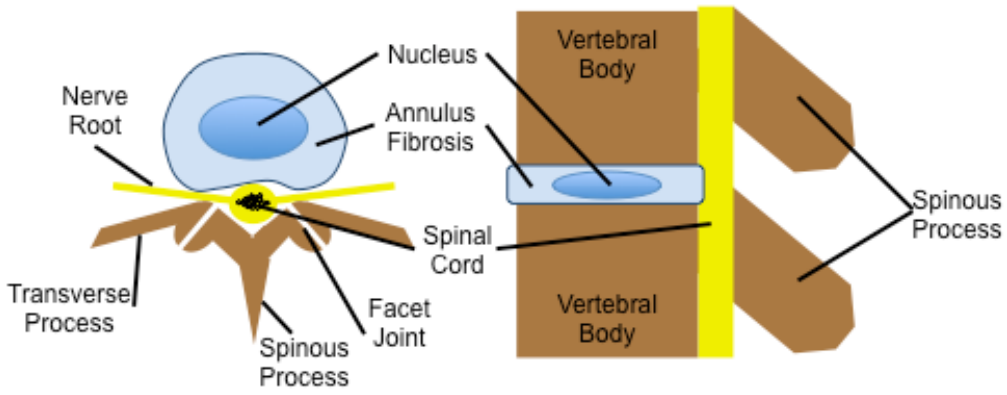

Figure 1-1. Axial (left) and sagittal (right) views of the intervertebral disc (IVD).

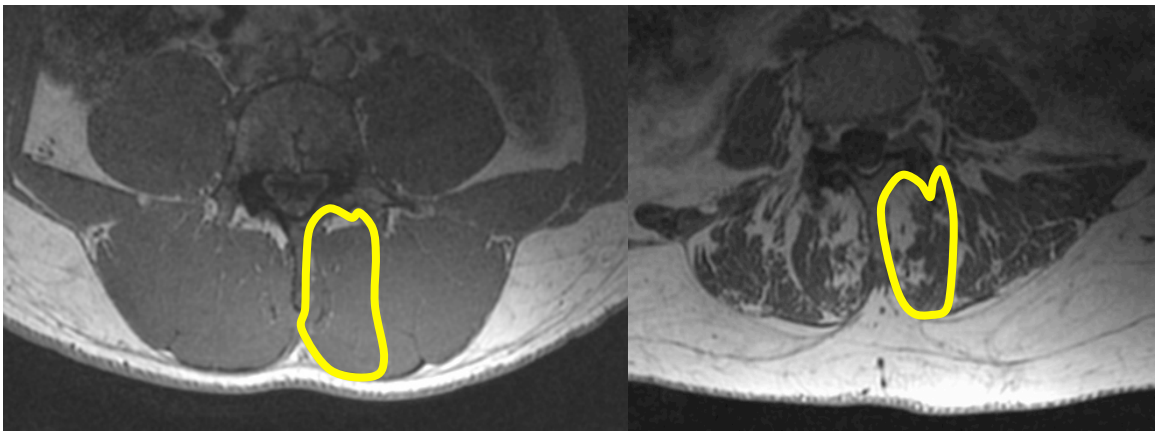

Figure 1-2. Axial T2 weighted MRIs of the lumbar spine in young (left) and aged (right) volunteers. The multifidus muscle is outlined in yellow.

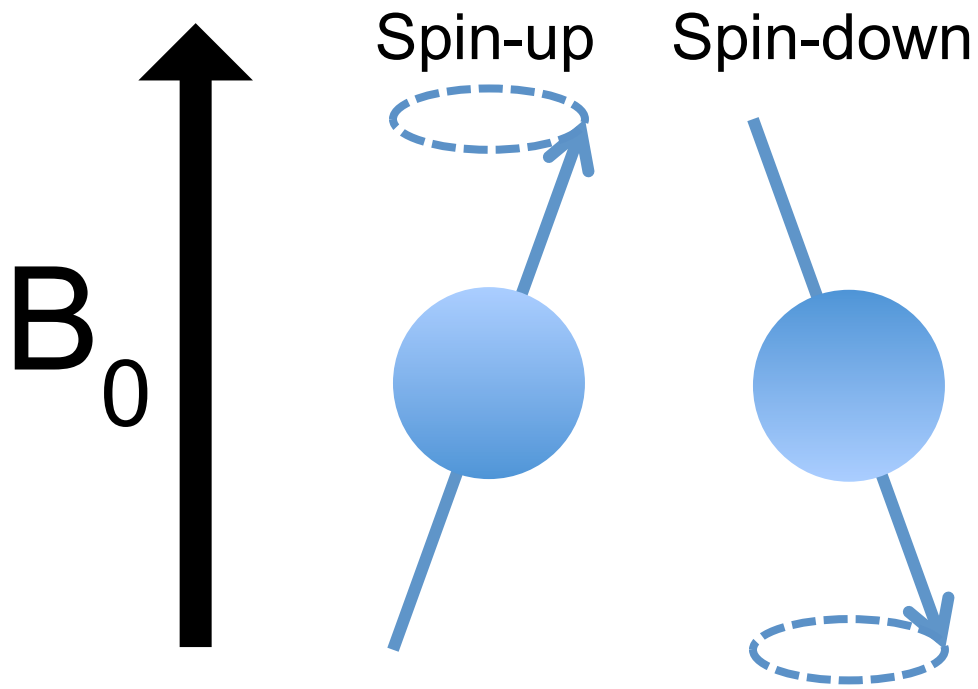

Figure 1-3. Precession of protons about the magnetic field (B_0). Protons can precess aligned with the magnetic field (spin-up) or directly opposite of the magnetic field (spin-down).

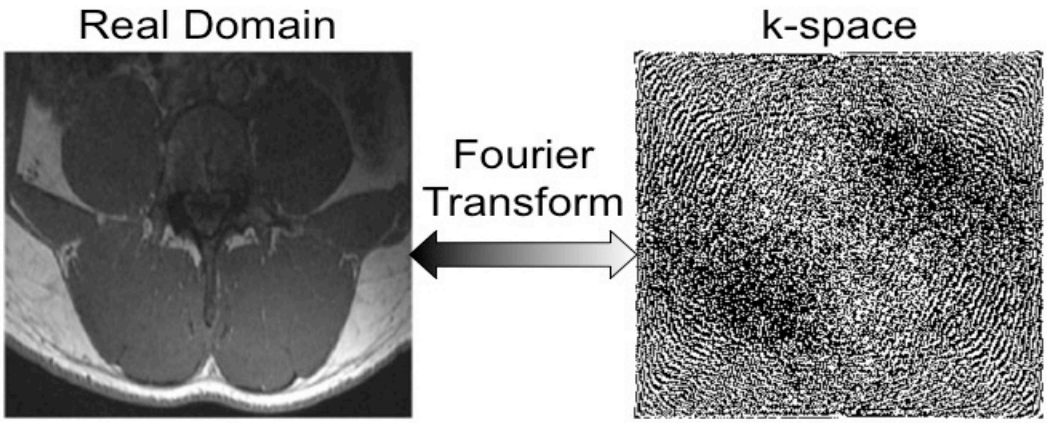

Figure 1-4. Sample MRI image in the real domain (left) and in the frequency domain (right).

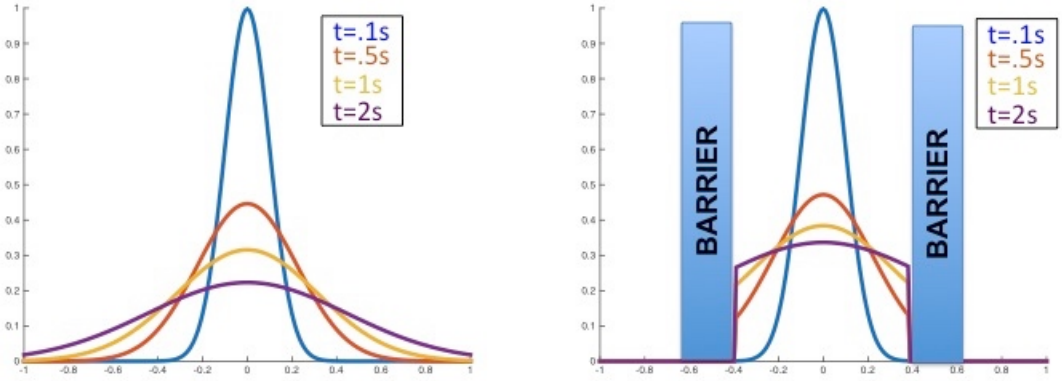

Figure 1-5. Characteristic bell shaped curve of Brownian diffusion (left) at different diffusion times. The distribution of particles is a dirac delta function at t=0s. As time increases, particles will diffuse further from the origin. When there are barriers to diffusion (right), particles will reflect off of the barrier, and the overall distribution of particles is confined.

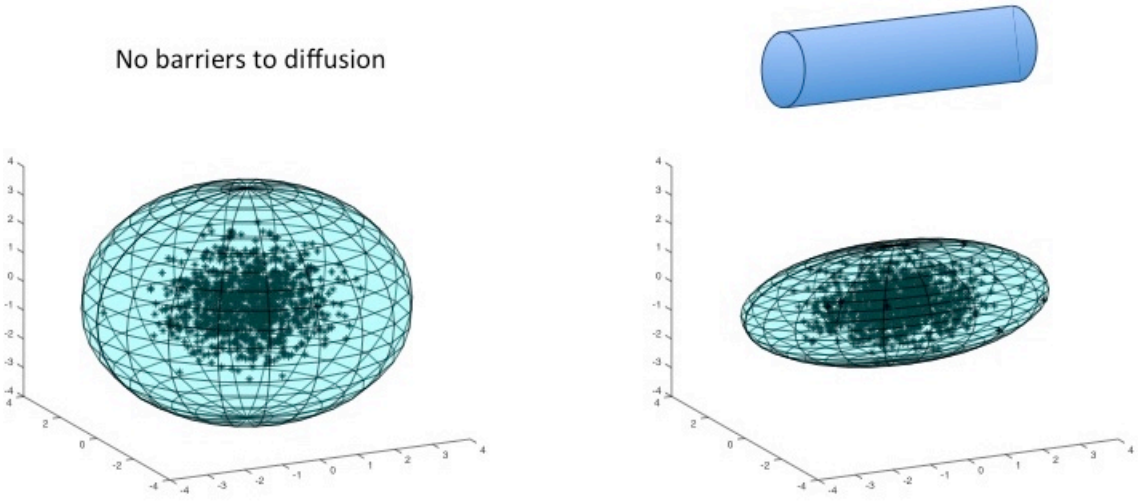

Figure 1-6. Schematic representation of particles (black) diffusing in a free (left) and a restricted (right) diffusion environment. The blue surface represents the diffusion tensor representative of the diffusion environment. When a columnar barrier restricts diffusion of water, it will diffuse further longitudinally, than radially.

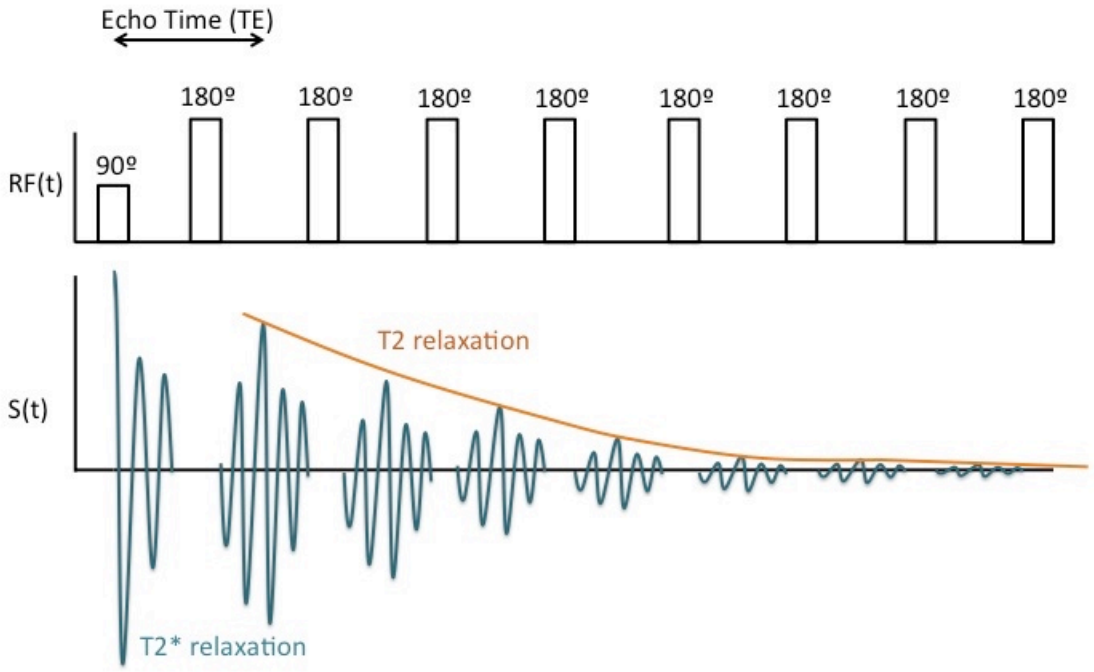

Figure 1-7. Schematic spin-echo MRI pulse sequence that can be used to measure transverse (T2) relaxation. Initially a 90° radiofrequency (RF) pulse is applied, after which the measured signal begins to rapidly decay due to signal dephasing (T2* relaxation). By applying a series of 180° RF pulses at equally spaced echo times (TE) after the original 90° pulse, T2 relaxation can be measured.

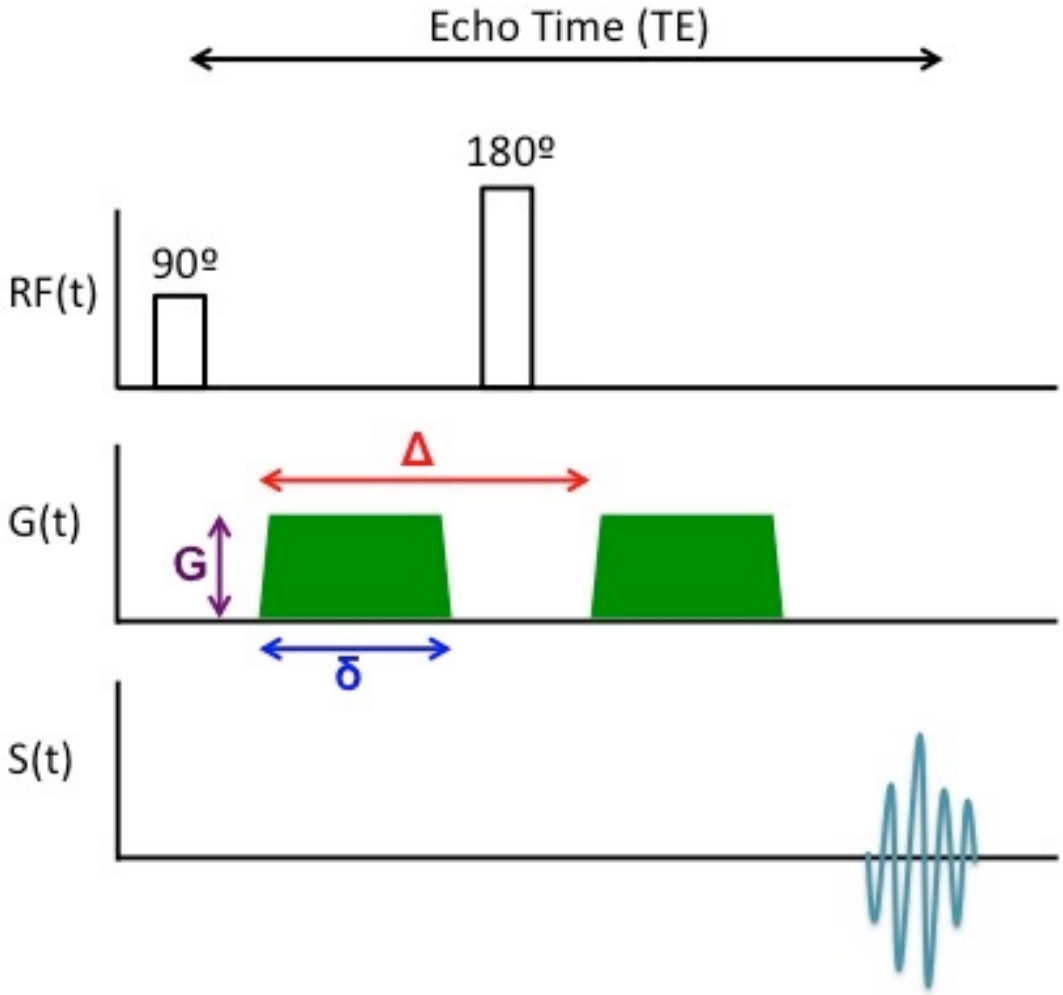

Figure 1-8. Schematic of a diffusion weighted, spin-echo pulse sequence. After an initial 90° radiofrequency pulse, a diffusion gradient is applied (green) for duration δ and gradient strength G. This diffusion gradient labels water molecules diffusing along a certain direction. After a 180° refocusing radiofrequency pulse is applied and a second diffusion gradient is applied at a time Δ after the start of the first diffusion gradient.

Figure 1-9. Sample tractography images made from diffusion tensor imaging of the spine. The multifidus (yellow) and erector spinae (red) group are shown in an anterior-posterior view (left) and a posterior-anterior view (right). Tractography can be used to estimate fiber bundle length in muscle.

1.7 References

1. Andersson GB. Epidemiological features of chronic low-back pain. The lancet. 1999;354:581-585.

2. Activity USAMS. Absolute and Relative Morbidity Burdens Attributable to Various Illnesses and Injuries, U.S. Armed Forces, 2013. Medical Surveillance Medical Report 2013. 2014;21:32.

3. Yu W, Ravelo A, Wagner TH, Phibbs CS, Bhandari A, Chen S, Barnett PG. Prevalence and costs of chronic conditions in the VA health care system. Medical Care Research and Review. 2003;60:146S-167S.

4. Martin BI, Deyo RA, Mirza SK, Turner JA, Comstock BA, Hollingworth W, Sullivan SD. Expenditures and health status among adults with back and neck problems. Jama. 2008;299:656-664.

5. Roy TC, Knapik JJ, Ritland BM, Murphy N, Sharp MA. Risk factors for musculoskeletal injuries for soldiers deployed to Afghanistan. Aviation, space, and environmental medicine. 2012;83:1060-1066.

6. Roy TC, Lopez HP, Piva SR. Loads worn by soldiers predict episodes of low back pain during deployment to Afghanistan. Spine. 2013;38:1310-1317.

7. Rodriguez-Soto AE, Jaworski R, Jensen A, NIederberger B, Hargens AR, Frank LR, Kelly KR, Ward SR. Effect of load carriage on lumbar spine kinematics. Spine. 2013;38:E783-791.

8. Rodriguez-Soto AE, Berry DB, Palombo L, Valaik E, Kelly KR, Ward SR. The Effect of Load Magnitude and Distribution on Lumbar Spine Posture in Active-Duty Marines. Spine. 2016.

9. Shirazi-Adl A, El-Rich M, Pop D, Parnianpour M. Spinal muscle forces, internal loads and stability in standing under various postures and loads—application of kinematics-based algorithm. European spine journal. 2005;14:381-392.

10. Ward SR, Kim CW, Eng CM, Gottschalk LJ 4th, Tomiya A, Garfin SR, Lieber RL. Architectural analysis and intraoperative measurements demonstrate the unique design of the multifidus muscle for lumbar spine stability. J Bone Joint Surg Am. 2009;91:176-185.

11. Panjabi MM. Clinical spinal instability and low back pain. Journal of electromyography and kinesiology. 2003;13:371-379.

12. O'sullivan PB, Phyty GDM, Twomey LT, Allison GT. Evaluation of specific stabilizing exercise in the treatment of chronic low back pain with radiologic diagnosis of spondylolysis or spondylolisthesis. Spine. 1997;22:2959-2967.

13. Morgan FP, King T. Primary instability of lumbar vertebrae as a common cause of low back pain. Bone & Joint Journal. 1957;39:6-22.

14. Shahidi B, Parra CL, Berry DB, HUbbard JC, Gombatto S, Zlomislic V, Allen RT, Hughes-Austin J, Garfin SR, Ward SR. Contribution of Lumbar Spine Pathology and age to Paraspinal Muscle Size and fatty Infiltration. Spine. 2016.

15. Crawford R, Filli L, Elliott J, Nanz D, Fisher MA, Marcon M, Ulbrich EJ. Age- and level-dependence of fatty infiltration in lumbar paravertebral muscles of healthy volunteers. American Journal of Neuroradiology. 2016;37:742-748.

16. Gans C. Fiber architecture and muscle function. Exercise and sport sciences reviews. 1982;10:160-207.

17. Lieber RL, Ward SR. Cellular mechanisms of tissue fibrosis. 4. Structural and functional consequences of skeletal muscle fibrosis. American Journal of Physiology-Cell Physiology. 2013;305:C241-C252.

18. Lieber RL, Ward SR. Skeletal muscle design to meet functional demands. Philosophical Transactions of the Royal Society B: Biological Sciences. 2011;366:1466-1476.

19. Danneels L, Vanderstraeten G, Cambier D, Witvrouw EE, Bourgois J, Dankaerts W, De Cuyper HJ. Effects of three different training modalities on the cross sectional area of the lumbar multifidus muscle in patients with chronic low back pain. British journal of sports medicine. 2001;35:186-191.

20. Eng CM, Abrams GD, Smallwood LR, Lieber RL, Ward SR. Muscle geometry affects accuracy of forearm volume determination by magnetic resonance imaging (MRI). Journal of biomechanics. 2007;40:3261-3266.

21. Einstein A. Über die von der molekularkinetischen Theorie der Wärme geforderte Bewegung von in ruhenden Flüssigkeiten suspendierten Teilchen. Annalen der physik. 1905;322:549-560.

22. Stejskal EO, Tanner JE. Spin diffusion measurements: spin echoes in the presence of a time-dependent field gradient. The journal of chemical physics. 1965;42:288-292.

23. Damon BM. Effects of image noise in muscle diffusion tensor (DT)-MRI assessed using numerical simulations. Magnetic resonance in medicine. 2008;60:934-944.

24. Oudeman J, Nederveen AJ, Strijkers GJ, Maas M, Luijten PR, Froeling M. Techniques and applications of skeletal muscle diffusion tensor imaging: A review. Journal of Magnetic Resonance Imaging. 2015.

25. Van Donkelaar C, Kretzers L, Bovendeerd P, Lataster LM, Nicolay K, Janssen JD, Drost MR. Diffusion tensor imaging in biomechanical studies of skeletal muscle function. Journal of anatomy. 1999;194:79-88.

26. Van Doom A, Bovendeerd P, Nicolay K, Drost M, Janssen J. Determination of muscle fibre orientation using diffusion-weighted MRI. Eur. J. Morphol. 1996;34:5-10.

27. Lieber RL. Skeletal muscle structure, function, and plasticity: Lippincott Williams & Wilkins; 2002.

28. Minamoto VB, Suzuki KP, Bremner SN, Lieber RL, Ward SR. Dramatic Changes in Muscle Contractile and Structural Properties After Two Botulinum Toxin Injections. Muscle & nerve. 2015.

29. Minamoto VB, Hulst JB, Lim M,Peace WJ, Bremner SN, Ward SR, Lieber RL. Increased efficacy and decreased systemic-effects of botulinum toxin A injection after active or passive muscle manipulation. Developmental Medicine & Child Neurology. 2007;49:907-914.

30. Karampinos DC, King KF, Sutton BP, Georgiadis JG. Myofiber ellipticity as an explanation for transverse asymmetry of skeletal muscle diffusion MRI in vivo signal. Annals of biomedical engineering. 2009;37:2532-2546.

31. Deux J, Malzy P, Paragios N, Bassez G, Luciani A, Zerbib P, Roudot-Thoraval F, Vignaud A, Kobeiter H, Rahmouni A. Assessment of calf muscle contraction by diffusion tensor imaging. European radiology. 2008;18:2303-2310.

32. Schwenzer NF, Steidle G, Martirosian P, Schraml C, Springer F, Claussen CD, Schick F. Diffusion tensor imaging of the human calf muscle: distinct changes in fractional anisotropy and mean diffusion due to passive muscle shortening and stretching. NMR in biomedicine. 2009;22:1047-1053.

33. Sinha S, Sinha U. Reproducibility analysis of diffusion tensor indices and fiber architecture of human calf muscles in vivo at 1.5 Tesla in neutral and plantarflexed ankle positions at rest. Journal of Magnetic Resonance Imaging. 2011;34:107-119.

34. Sinha U, Sinha S, Hodgson JA, Edgerton RV. Human soleus muscle architecture at different ankle joint angles from magnetic resonance diffusion tensor imaging. Journal of applied physiology. 2011;110:807-819.

35. Okamoto Y, Kemp GJ, Isobe T, Sato E, Hirano Y, Shoda J, Minami M. Changes in diffusion tensor imaging (DTI) eigenvalues of skeletal muscle due to hybrid exercise training. Magnetic resonance imaging. 2014;32:1297-1300.

36. Hatakenaka M, Yabuuchi H, Sunami S, Kamitani T, Takayama Y, Nishikawa K, Honda H. Joint position affects muscle proton diffusion: evaluation with a 3-T MR system. American Journal of Roentgenology. 2010;194:W208-W211.

37. Shiraishi T, Chikui T, Inadomi D, Kagawa T, Yoshiura K, Yuasa K. Evaluation of diffusion parameters and T2 values of the masseter muscle during jaw opening, clenching, and rest. Acta Radiologica. 2012;53:81-86.

38. Hatakenaka M, Matsuo Y, Setoguchi T, Yabuuchi H, Okafuji T, Kamitani T, Nishikawa K, Honda H. Alteration of proton diffusivity associated with passive muscle extension and contraction. Journal of Magnetic Resonance Imaging. 2008;27:932-937.

39. Sigmund EE, Novikov DS, Sui D, Ukpebor O, Baete S, Bapp JS, Liu K, Feiweier T, Kwon J, McGorty K, Bencardino J, Fieremans E. Time-dependent diffusion in skeletal muscle with the random permeable barrier model (RPBM): application to normal controls and chronic exertional compartment syndrome patients. NMR in Biomedicine. 2014;27:519-528.

40. McMillan AB, Shi D, Pratt SJ, Lovering RM. Diffusion tensor MRI to assess damage in healthy and dystrophic skeletal muscle after lengthening contractions. BioMed Research International. 2011;2011.

41. Dalakas MC. Polymyositis, dermatomyositis, and inclusion-body myositis. New England Journal of Medicine. 1991;325:1487-1498.

42. Griggs RC, Askanas V, DiMauro S, Engel A, Karpati G, Mendell JR, Rowland LP. Inclusion body myositis and myopathies. Annals of neurology. 1995;38:705-713.

43. Arnardottir S, Alexanderson H, Lundberg IE, Borg K. Sporadic inclusion body myositis: pilot study on the effects of a home exercise program on muscle function, histopathology and inflammatory reaction. Journal of rehabilitation medicine. 2003;35:31-35.

44. Plotz PH, Dalakas M, Leff RL, Love LA, Miller FW, Cronin ME. Current concepts in the idiopathic inflammatory myopathies: polymyositis,

dermatomyositis, and related disorders. Annals of internal medicine. 1989;111:143-157.

45. Dalakas MC, Hohlfeld R. Polymyositis and dermatomyositis. The Lancet. 2003;362:971-982.

46. Okamoto Y, Kunimatsu A, Miki S, Shindo M, Nitsu M, Minami M. Fractional anisotropy values of calf muscles in normative state after exercise: preliminary results. Magnetic Resonance in Medical Sciences. 2008;7:157-162.

47. Yanagisawa O, Kurihara T, Kobayashi N, Fukubayashi T. Strenuous resistance exercise effects on magnetic resonance diffusion parameters and muscle–tendon function in human skeletal muscle. Journal of Magnetic Resonance Imaging. 2011;34:887-894.

48. Yanagisawa O, Kurihara T, Okumura K, Fukubayashi T. Effects of Strenuous Exercise with Eccentric Muscle Contraction: Physiological and Functional Aspects of Human Skeletal Muscle. Magnetic Resonance in Medical Sciences. 2010;9:179-186.

49. Esposito A, Campana L, Palmisano A, De Cobelli F, Canu T, Santarella F, Colantoni C, Monno A, Vezzoli M, Pezzetti F, Manfredi AA, Rovere-Querini P, Del Maschio A. Magnetic resonance imaging at 7T reveals common events in age-related sarcopenia and in the homeostatic response to muscle sterile injury. PloS one. 2013;8.

50. Fan RH, Does MD. Compartmental relaxation and diffusion tensor imaging measurements in vivo in λ-carrageenan-induced edema in rat skeletal muscle. NMR in biomedicine. 2008;21:566-573.

51. Belton PS, Jackson RR, Packer KJ. Pulsed NMR studies of water in striated muscle: I. Transverse nuclear spin relaxation times and freezing effects. Biochimica et Biophysica Acta (BBA)-General Subjects. 1972;286:16-25.

52. Cole WC, Leblanc AD, Jhingran SG. The origin of biexponential T2 relaxation in muscle water. Magnetic resonance in medicine. 1993;29:19-24.

53. Zhang J, Zhang G, Morrison B, Mori S, Sheikh KA. Magnetic resonance imaging of mouse skeletal muscle to measure denervation atrophy. Experimental neurology. 2008;212:448-457.

54. Abdullah OM, Drakos SG, Diakos NA, Wever-Pinzon O, Kfoury AG, Stehlik J, Selzman CH, Reid BB, Brunisholz K, Verma DR, Myrick C, Sachse FB, Li DY, Hsu EW. Characterization of diffuse fibrosis in the failing human heart via

diffusion tensor imaging and quantitative histological validation. NMR in Biomedicine. 2014;27:1378-1386.

55. Nishii T, Kono AK, Shigeru M, Takamine S, Fujiwara S, Kyotani K, Aoyama N, Sugimura K. Cardiovascular magnetic resonance T2 mapping can detect myocardial edema in idiopathic dilated cardiomyopathy. The international journal of cardiovascular imaging. 2014;30:65-72.

56. Froeling M, Oudeman J, Strijkers GJ, Maas M, Drost MR, Nicolay K, Nederveen AJ. Muscle changes detected with diffusion-tensor imaging after long-distance running. Radiology. 2014;274:548-562.

57. Ababneh Z, Beloeil H, Berde CB, Gambarota G, Maier SE, Mulkern RV. Biexponential parameterization of diffusion and T2 relaxation decay curves in a rat muscle edema model: decay curve components and water compartments. Magnetic resonance in medicine. 2005;54:524-531.

58. Baete SH, Cho G, Sigmund EE. Multiple-echo diffusion tensor acquisition technique (MEDITATE) on a 3T clinical scanner. NMR in Biomedicine. 2013;26:1471-1483.

59. Fan RH, Does MD. Compartmental Relaxation and DTI Measurements In Vivo in λ-Carrageenan Induced Edema in Rat Skeletal Muscle. NMR in Biomedicine. 2008;21:566.

60. Ai T, Yu K, Gao L, Zhang P, Goerner F, Runge VM, Li X. Diffusion tensor imaging in evaluation of thigh muscles in patients with polymyositis and dermatomyositis. The British journal of radiology. 2014;87:20140261.

61. Knox J, Orchowski J, Scher DL, Owens BD, Burks R, Belmont PJ. The incidence of low back pain in active duty United States military service members. Spine. 2011;36:1492-1500.

62. Saotome T, Sekino M, Eto F, Ueno S. Evaluation of diffusional anisotropy and microscopic structure in skeletal muscles using magnetic resonance. Magnetic resonance imaging. 2006;24:19-25.

CHAPTER 2: LUMBAR SPINE POSTURES IN MARINES DURING SIMULATED OPERATIONAL POSITIONS

2.1 ABSTRACT

Low back pain has a 70% higher prevalence in members of the armed forces than in the general population, possibly due to the loads and positions soldiers experience during training and combat. Although the influence of heavy load carriage on standing lumbar spine posture in this population is known, postures in other operationally relevant positions are unknown. Therefore, the purpose of this study was to characterize the effect of simulated military operational positions under relevant loading conditions on global and local lumbar spine postures in active duty male US Marines. Secondary objectives were to evaluate if intervertebral disc degeneration and low back pain affect lumbar spine postures. Magnetic resonance images were acquired on an upright scanner in the following operational positions: natural standing with no external load, standing with body armor (11.3 kg), sitting with body armor, and prone on elbows with body armor. Custom software was used to measure global lumbar spine posture: lumbosacral flexion, sacral slope, lordosis, local measures of intervertebral angles, and intervertebral distances. Sitting resulted in decreased lumbar lordosis at all levels of the spine except L1−L2. When subjects were prone on elbows, a significant increase in local lordosis was observed only at L5−S1 compared with all other positions. Marines with disc degeneration (77%) or history of low back pain (72%) had decreased lumbar range of motion and less lumbar extension than healthy Marines. These results indicate that a male

Marine's pathology undergoes a stereotypic set of postural changes during functional tasks, which may impair performance.

2.2 INTRODUCTION

Low back pain (LBP), one of the most common musculoskeletal complaints, affects between 70% and 85% of the population at any given time,[1] and is a particularly large problem in the military. In 2013, military medical encounters due to back pain were greater than any other major medical condition (975,000).[2] Additionally, the Veterans Health Administration has seen an increasing trend in the incidence of LBP in recent years.[3] These trends yield a large financial burden on the Departments of Defense and Veterans Affairs to provide health care to these individuals, costing over $2 billion annually.[4,5]

Members of the US Armed Forces are a unique population due to the physical demands required by their job. Increased rates of intervertebral disc (IVD) degeneration have been associated with increased military service, time, and age,[6] and individuals with IVD degeneration have been shown to have a higher incidence of LBP.[7] The increased rates of reported LBP in Marines may be attributed to pathophysiologic changes occurring in the lumbar spine, resulting from heavy loads and unusual positions experienced in training and combat.[8] Until recently, these ideas had not been measured directly. Rodriguez-Soto et al.[9] observed that heavy loading creates postural changes in standing that are not further exacerbated by the duration of loading or activity (e.g., marching with load). Although standing with heavy loads is not necessarily an injury- or pain-provoking activity in these subjects, the effect of other operationally relevant tasks

and positions on posture have not been studied. For example, military members are often required to maintain static positions such as standing, sitting, and prone for extended periods of time (depending on military occupational specialty), which may contribute to LBP. In particular, members of the military have reported LBP induced by prolonged sitting in vehicles, suggesting sitting posture may also be related to back pain in this population.[10]

The influence of IVD degeneration and LBP on posture has also been studied in a male civilian population. Subjects with idiopathic LBP have been found to have less overall lordosis, but increased local lordosis in the upper lumbar spine compared with healthy controls.[11] In subjects with disc degeneration and LBP, decreased segmental range of motion between extension and flexion positions was found at levels with degenerated IVDs compared to levels with nondegenerated IVDs.[12,13] Understanding the relationship between the health and posture of the lumbar spine is crucial to understanding why subjects may be at risk of developing LBP. However, the results of the previous studies may not translate to the military due to the difference in age, loads worn in training, and physical activity level. The influence of IVD degeneration and LBP on posture in operationally relevant positions has not been studied in a military population, and may provide insight into whether task modification would be recommended for military personnel with these pathologies.

Therefore, the purpose of this study was to investigate changes in lumbar spine posture, in a variety of operationally relevant positions, with the minimum operationally relevant load, in active duty male Marines. Secondary analyses were performed to compare lumbar spine postures between Marines with and without IVD degeneration, and

with and without LBP. We hypothesized that Marines with IVD degeneration or LBP would have less lower lumbar lordosis in operationally relevant positions than healthy Marines.

2.3 METHODS

2.3.1 Participants

Forty-three active duty male Marines from the Marine Corps Base Camp Pendleton volunteered to participate in this study. The University of California, San Diego and Naval Health Research Center Institutional Review Boards approved this study, and all Marines gave oral and written consent to participate.

2.3.2 Low Back Pain Evaluation

The Baecke questionnaire on habitual physical activity was administered to classify a Marine's daily work, leisure, and sport-related activity levels.[14] The Roland-Morris Disability Questionnaire data were collected to assess how a participant's LBP limits the ability to perform everyday activities.[15] We used another questionnaire to assess self-reported LBP on an 11-point numeric rating scale (0–10; 0 = no pain, 10 = worst imaginable pain) at the time of data collection, duration of the current episode of LBP (if applicable), duration of LBP since the first episode (if applicable), and number of LBP episodes within the last year. Additionally, volunteers were asked to report the activities that aggravated or eased their LBP symptoms.

2.3.3 Imaging

Marines were scanned using an upright 0.6T magnetic resonance imaging (MRI) scanner (Upright Multi-Position MRI, Fonar Corporation, Melville, NY) and a planar coil. An elastic band was used to hold the coil against the volunteer's lumbar spine

between the L1–S1 levels while standing. The band was secured to hold the coil in place while retaining the volunteer's natural position. A three-plane localizer (TR = 1254 ms, TE = 100 ms, FOV = 34 cm, matrix = 256 × 256, in-plane resolution = 1.33mm x 1.33mm, THK = 9 mm, NEX = 1, time = 0:17) and sagittal T2-weighted images (TR = 1974 ms, TE = 160 ms, FOV = 35 cm, matrix = 224 × 224, in-plane resolution = 1.56mm x 1.56mm, THK = 3 mm, gap = 0 mm, NEX = 1, time = 2:12) were acquired.

2.3.4 Load Carriage and Position Tasks

Marines were scanned in the following positions: standing without load, standing with body armor (11.3 kg), sitting with body armor, and prone on elbows with body armor (Fig. 1). Positions with external load were randomized to control for the cumulative effects of loading over time. Body armor was selected for the load configuration in the current study, because it is the minimum protective equipment Marines are required to wear at all times during military operations/training. Marines were not instructed on how to assume each position, but were asked to hold each position steady for the duration of the MRI acquisition. At the end of each scan, volunteers were asked to rate their level of LBP in each position on an 11-point numeric rating scale. Volunteers were classified as having increased pain in a position if LBP on the numeric rating scale was greater than baseline levels when standing without load.

2.3.5 Disc Grading

Lumbar IVD degeneration was assessed by an experienced radiologist (C.C.) using the Pfirmmann grading scale.[16] The Pfirmmann classification system categorizes IVD degeneration from Grade I (normal) to Grade V (severely degenerated), based on nucleus pulposus signal strength and homogeneity, and intervertebral distance. Marines were separated into degenerated or nondegenerated groups based on the Pfirmmann grade

of the L5−S1 IVD. A threshold of Pfirmmann Grade III was used to define spine degeneration because data support that IVD biomechanics begin to change at this grade.[17–19]

2.3.6 Kinematic Measurements

Postural measurements were generated from upright MRI images in each position, using a previously validated algorithm.[20] Briefly, digital seed points were manually placed on the corners of the vertebral body and on the posterior elements of each vertebra using OsiriX.[21] The locations of the seed points were imported into MATLAB (MathWorks Inc., Natick, MA) and used to define an endplate-based joint coordinate system applied to the superior and inferior endplate of each vertebra (L1−S1).

Global and local measurements of lumbar spine posture, intervertebral angles, and distances were calculated for all positions (Fig. 2). Global measurements included angle with respect to the horizontal, sacral slope, and sagittal Cobb angle. The angle with respect to the horizontal is defined as the angle between a line connecting the geometric centroids of L1 and S1, and a line perpendicular to gravity, pointing anteriorly. This measurement indicates the degree of lumbosacral flexion or extension of the entire lumbar spine in the sagittal plane. For the prone loaded position, images were rotated 90 degrees to allow for comparison of the measurements from the prone position to other positions (Fig. 1).The sacral slope is defined as the angle between the superior endplate of S1 and the horizontal, and describes the orientation of the sacrum to provide an estimate of pelvic rotation. The sagittal Cobb angle is used extensively to measure the curvature of the spine and is defined from the superior endplate of L1 to the superior endplate of S1.[22] Sagittal intervertebral angles were measured between the superior and

inferior endplates of adjacent vertebrae to describe local changes in lordosis and distribution of lordosis throughout the lumbar spine. Intervertebral distances were measured as the anterior, central, and posterior Euclidean distance between planes fit to the endplates of each vertebra.

2.3.7 Statistical Analysis

Demographic comparisons of age, height, weight, and body mass index (BMI) between volunteers with and without IVD degeneration or LBP were evaluated using independent t-tests. Global kinematic measurements (angle with respect to the horizontal and Cobb angle) were compared using one-way repeated measures analysis of variance (ANOVA) tests with post hoc Sidak tests to identify differences between positions. Local measurements (intervertebral angles and heights) were analyzed using two-way repeated measures ANOVA tests with post hoc Sidak tests to identify differences between positions and intervertebral levels. Secondary analyses were conducted to determine kinematic differences in Marines with and without LBP or IVD degeneration. Volunteers were grouped based on presence of LBP on the day of data collection (yes, no), when the current episode of LBP began (chronic >6 months, acute <6 months, none), history of LBP (yes, no) and positional back pain (extension, neutral, sitting, none), and degeneration of the lumbar spine assessed by Pfirmmann grading (L5−S1 IVD > Grade II). Separate two-way ANOVAs (position × LBP or IVD variable) with post hoc Sidak tests were performed to identify differences for each variable describing LBP or disc degeneration. To investigate the relationship between disc degeneration, LBP, and segmental range of motion, we calculated the difference in postural measurements between the sitting and prone positions. Differences in segmental range of motion for

each variable describing LBP or disc degeneration were compared using independent t-tests. The threshold for significance (α) was set to 0.05 for all analyses. η^2 and Cohen's d effect sizes are reported for ANOVA and post hoc tests respectively. Analyses were conducted using IBM SPSS Statistics 20.0 (IBM, Armonk, NY). All data are reported as mean ± standard deviation.

2.4 RESULTS

2.4.1 Marine Demographics

Complete image data sets were obtained from 43 male Marines (mean age = 26.8 ± 6.4 years, height = 1.78 ± 0.07 meters, weight = 82.04 ± 9.85 kg, BMI = 25.90 ± 2.86 kg/m^2; Table 1). IVD degeneration assessed using the Pfirmmann classification system (>2) was observed in 125 out of 215 (58%) of all graded lumbar IVDs (Fig. 3). Based on the Pfirmmann grades (>2) of the L5−S1 IVD, 33 of 43 (77%) Marines were in the degenerated group, and 10 were in the nondegenerated group.

The Baecke and Roland-Morris questionnaires were collected from 32 Marines. The average Baecke score was 9.96 ± 1.61 (range: 7.25–13.25). The Roland-Morris average score was 2.69 ± 3.25 (range: 0–13, 22/32 had score >0). Back pain history information was collected from 39 Marines. At the time of data collection, 16 of 39 (41%) Marines reported current back pain (7 chronic LBP, 9 acute LBP), and 28 of 39 (72%) Marines reported previously experiencing at least one episode of LBP. Marines self-reported that sitting, standing for extended periods of time, and hiking with a pack resulted in increased LBP. Additionally, lying supine and positions of lumbar spine extension were reported to decrease LBP in this population. Positional back pain

information was collected from 32 Marines. Seven participants reported LBP when standing unloaded (22%), 9 when standing loaded (28%), 6 when sitting loaded (19%), and 11 when prone loaded (34%).

2.4.2 Effect of Position on Global Posture

Significant differences occurred in lumbosacral flexion ($p < 0.001$, $\eta^2 = 0.22$), sacral slope ($p < 0.001$, $\eta^2 = 0.51$), and lumbar lordosis ($p < 0.001$, $\eta^2 = 0.60$) between tasks (Fig. 4). Compared to standing without load, standing wearing body armor resulted in a small decrease in sacral slope (3°, $p = 0.006$, d = 0.19), indicating slight posterior tilt of the pelvis, while lumbosacral flexion and lumbar lordosis remained constant. Decreased sacral slope (>21°, $p < 0.001$, d = 0.33-1.03) and lumbar lordosis (>30°, $p < 0.001$, d = 0.92-1.18) were observed when sitting loaded compared with other positions. No change in lumbosacral flexion was observed during sitting relative to standing positions. Compared with standing unloaded, when Marines were prone on elbows, lumbosacral flexion increased (5.5°, $p = 0.016$, d = 0.40), sacral slope decreased (14°, $p < 0.001$, d = 0.98), and lumbar lordosis increased (6°, $p = 0.001$, d = 0.33). Interestingly, both sitting and prone on elbows positions resulted in significantly decreased sacral slope compared to standing without load, indicating posterior pelvic tilt.

2.4.3 Effect of Position on Local Posture

Local intervertebral angles were measured to identify regional contributions to overall lumbar posture. A significant effect of level ($p < 0.001$, $\eta^2 = 0.49$), position ($p < 0.001$, $\eta^2 = 0.54$), and an interaction of level x position ($p < 0.001$, $\eta^2 = 0.30$) for intervertebral angles was found. When volunteers were sitting, a significant decrease in lordosis was evident at all levels of the lumbar spine except at L1−L2 (Fig. 5). Larger decreases in lordosis were found in the inferior lumbar spine than in the superior lumbar

spine when seated. When Marines were prone on elbows, the only level where a significant increase in lordosis was found was L5−S1, indicating that overall lordosis changes in this position originate from L5−S1.

Intervertebral distance was measured to identify local IVD compression and excursion in different postures (Fig. 6). A significant effect of level ($p < 0.001$), position ($p < 0.001$), and an interaction of level x position ($p < 0.001$) for anterior ($\eta^2_{level} = 0.31$, $\eta^2_{position} = 0.37$, $\eta^2_{interaction} = 0.13$), central ($\eta^2_{level} = 0.06$, $\eta^2_{position} = 0.21$, $\eta^2_{interaction} = 0.01$), and posterior ($\eta^2_{level} = 0.07$, $\eta^2_{position} = 0.12$, $\eta^2_{interaction} = 0.05$) intervertebral distance was found. Intervertebral distance changes paralleled changes in intervertebral lordosis at all levels. The sitting position resulted in anterior compression from L2−L3 to L5−S1 ($p < 0.009$, d = 0.62 – 0.90), and posterior distraction from L3−L4 to L5−S1 ($p < 0.017$, d = 0.20 – 0.38), with magnitude of effect increasing inferiorly through the lumbar spine. Additionally, sitting resulted in a slight loss of central intervertebral distance from L2−L3 to L5−S1 ($p < 0.011$, d = 0.15 – 0.31) compared with standing unloaded, with magnitude of effect increasing inferior through the lumbar spine. Similarly, the prone on elbows position induced an anterior intervertebral distance distraction at L5−S1 ($p < 0.001$, d = 0.28 – 0.68).

2.4.4 Effect of Intervertebral Disc Degeneration on Lumbar Spine Posture

No lumbar spine postural differences were found between Marines with and without disc degeneration at L5−S1. However, Marines with IVD degeneration at L5−S1 were found to have less whole lumbar range of motion, measured as the Cobb angle between sitting loaded and prone on elbows loaded positions, than Marines with no IVD degeneration (9°, $p = 0.002$, d = 0.13). Interestingly, this difference between groups

appears to be driven by decreased intervertebral segmental range of motion at L2−L3 (2.1°, p = 0.031, d = 0.29), L3−L4 (1.0°, p = 0.015, d = 0.14), and L4−L5 (1.9°, p = 0.039, d = 0.19).

2.4.5 Effect of Low Back Pain on Lumbar Spine Posture

There were no significant differences in lumbar spine posture, intervertebral angle, or intervertebral distance between Marines with and without back pain at the time of data collection, or with and without reported back pain in each position. However, there was a difference in angle with respect to the horizontal ($p < 0.001$, $\eta^2 = 0.27$) when the current episode of LBP was subclassified into chronic, acute, or no LBP. Marines with chronic LBP displayed more extension of the lumbosacral spine than those without LBP (~4°, p = 0.024, d = 0.61) and Marines with an acute episode of LBP (~3°, p = 0.048, d = 0.08) when standing without external load. Additionally, when sitting with body armor, Marines with chronic LBP displayed more extension of the lumbosacral spine than those with an acute episode of LBP (5°, p = 0.021, d = 0.24), but their posture was the same as Marines without LBP (p = 0.105, d = 0.21). When subjects were classified by history of LBP, a significant effect was found for angle with respect to the horizontal ($p < 0.001$, $\eta^2 = 0.12$). Participants who reported a history of LBP displayed less intervertebral extension at L5−S1 (6°, p = 0.024, d = 0.78) when prone on elbows, with corresponding less anterior distraction (4 mm, p = 0.028, d = 0.50) than those who did not have an episode of LBP.

2.5 DISCUSSION

In this study, we evaluated the lumbar spine posture in 43 active duty male Marines in simulated, relevant operational positions and loading conditions. Position-dependent changes in global lumbar spine postures were found in lumbosacral extension, sacral slope, and lumbar lordosis. Sitting with body armor resulted in a reduced lumbar lordosis of over 30°, but no changes in the forward inclination of the lumbar spine with respect to standing positions was observed. The addition of load did not change standing posture as was previously observed.[9] This is likely related to the small load magnitude used in this study (11.3 kg) compared with the previous study (50.8 kg). This load magnitude was used because tasks involving sitting and being prone on elbows typically do not involve the heavy packs used in previous studies. Additionally, the load from the body armor was evenly distributed anterior-posterior, while the load distribution in previous studies was distributed with a posterior bias, which may have an effect on the response of the lumbar spine to loading.

To determine the location of global position-dependent differences in posture, we measured sagittal intervertebral angles and intervertebral heights. The largest decrease in lordosis relative to standing was observed between L2 and S1 when volunteers were sitting, with magnitudes of change increasing caudally, similar to previous studies.[23] Interestingly, when volunteers were prone on elbows, the only intervertebral segment with a measured increase in lordosis was found in L5−S1. Additionally, this level had the largest segmental range of motion between sitting and prone positions, and the largest number of discs that were classified as degenerated (33/43). Decreases in anterior intervertebral distance, driven by intervertebral flexion, were observed between L2 and

S1, with anterior intervertebral distance progressively decreasing caudally. This follows previous observations that changes in intervertebral distance appear to track changes in sagittal intervertebral angle, not task or load.[9]

During this study, we did not specifically recruit Marines with LBP. However, we observed a relationship between history of LBP and posture in Marines. In standing and sitting positions, Marines with chronic LBP (current episode lasting >6 months) had more lumbosacral extension than Marines with no back pain or Marines with an acute (<6 months) case of LBP. O'Sullivan identified that LBP subjects with lumbar segmental instability can be classified into four groups, based on the manifestation of the patients' symptoms and motor dysfunction: flexion, extension, lateral shift, and multidirectional patterns.[24,25] Of those subclassifications, the extension pattern has been reported to be due to repetitive low impact trauma associated with sporting activities, such as hiking with a heavy pack.[24] These data support the idea that postural changes in soldiers with chronic LBP may be due to heavy loads carried in training and combat.

In the present study, approximately half of the Marines reported LBP as a result of sitting for extended periods of time. It was previously reported that volunteers who sit for extended periods of time are at risk for developing LBP.[26] A 2007 review paper by Lis et al. determined that people with occupations requiring them to sit for over half of the workday, and who are exposed to factors such as whole body vibration and/or awkward postures, are at an increased risk of developing LBP.[26] The Marines in this study are often exposed to whole body vibration during transport in tactical vehicles and helicopters, and remain in awkward positions such as prone on elbows, for extended periods of time. Therefore, the high rate of LBP in this young population of Marines is

likely attributable to their high occupational demands during both training and combat situations.

In this study, 58% of all IVDs were classified as degenerated, which is greater than among older patients imaged for LBP (45.5 years old, 44% degenerated).[13] Marines with IVD degeneration experienced less whole lumbar range of motion between sitting and prone positions. It has been established that disc degeneration decreases local segmental range of motion using upright MRI.[13] As a disc degenerates, functional spinal units become hypermobile (Pfirmmann Grades III and IV) and then hypomobile (Pfirmmann Grade V).[17-19] Although we did not identify local changes in segmental range of motion, possibly because they were below our threshold of detection, we hypothesize that small changes at each level all contributed to the overall observed change in lumbar range of motion. Several studies have found trends toward differences in the posture of the lumbar spine with disc degeneration; however, it is unclear if disc degeneration leads to increased or decreased lordosis.[12,13,27,28] Disc degeneration occurs in the normal progression of aging, but it can be accelerated by lifestyle factors such as excessive loading or smoking.[11] People with physically intensive jobs are at risk for accelerated IVD degeneration. Marines in our study had higher levels of habitual physical activity, measured by the Baecke questionnaire, than civilians of similar age[14,29] because they routinely engage in physical activity and training per their infantry program of instruction.

There are several limitations to this study. First, imaging resolutions were 1.56 mm in plane and 3.0 mm thick. We know from prior validation work[20] that this yields low angular error rates (~1 deg), but it does mean that our confidence in linear changes in

disc height is relatively coarse. Second, our secondary analyses included a number of univariate comparisons aimed at identifying kinematic differences between Marines with and without LBP or with and without IVD degeneration. Because of the structure of these variables and our statistical approach, type I error rates could have been elevated. However, the subtle effects of LBP and IVD degeneration on whole spine kinematics are consistent with prior observations in civilian populations.

This study was performed on active, young Marines, and their postural responses to loading may not apply to a civilian population. Due to the intense training and demands of their jobs, the Marines in this study were extremely fit, and trained on how to adapt their posture in different positions while wearing body armor to minimize their risk of injury. One of the long-term goals of this line of research is to identify Marines who were at risk for developing LBP based on their posture profile. We observed that Marines with chronic LBP exhibit an extension pattern of LBP, which may be related to the loads they carry during training and combat. Marines carry required equipment to ensure they can successfully complete their job, a load that sometimes exceeds the standard 32 kg. Since we have previously investigated the effect of heavy load on lumbar spine posture, and have identified postural differences in Marines with pathology in this study, further studies on LBP and disc degeneration in Marines should focus on managing the anterior-posterior distribution of load around the torso center of mass. We have previously noted that balanced loads minimize postural changes in standing[30], but their influence on non-standing postures (e.g. sitting) have not been investigated. A second long-term goal of this research is to understand position-related lumbar spine disease and to understand the influence of loading and position on existing lumbar spine pathology. For example, future

work should test the influence of relevant positions and loads on stable and unstable disc protrusions/fragmentations in the civilian population. These studies may shed light onto more appropriate, or patient specific, exercise regimes for individuals with anatomically identifiable sources of low back pain.

2.6 CONCLUSION

This study investigated the effect of operationally relevant positions on lumbar spine posture in active duty male Marines. Sitting and prone on elbows positions resulted in large global postural differences in the lumbar spine, with the greatest local change found at L5−S1. This level also had the highest incidence of IVD degeneration in the lumbar spine. Overall, we found that Marines have a high incidence of lumbar disc degeneration and high rates of LBP, particularly in the sitting position. Marines with disc degeneration at L5−S1 had decreased lumbar range of motion and Marines with chronic LBP had more lumbar extension. Subtle postural changes were seen in subjects with disc degeneration or LBP, resulting in increased overall lumbar lordosis and decreased lumbar range of motion. These results provide the framework for postural interventions aimed at reducing LBP, and perhaps, risk factors for LBP in Marines during operational tasks.

2.7 ACKNOWLEDGMENTS

I am a military service member (or employee of the U.S. Government). This work was prepared as part of my official duties. Title 17 U.S.C. § 105 provides the “Copyright protection under this title is not available for any work of the United States Government.” Title 17 U.S.C. § 101 defines a U.S. Government work as work prepared by a military

service member or employee of the U.S. Government as part of that person's official duties.

This manuscript was supported by the U.S. Army Medical Research Acquisition Activity, Award No. W81XWH-13-2-0043 (work unit no. 1305). This work was supported by DoD grant PR120576 (SRW & KK). The views expressed in this article are those of the authors and do not necessarily reflect the official policy or position of the Department of the Navy, Department of the Army, Department of the Air Force, Department of Veterans Affairs, Department of Defense, or the U.S. Government. Approved for public release; distribution unlimited.

Human subjects participated in this study after giving their free and informed consent. This research has been conducted in compliance with all applicable federal regulations governing the protection of human subjects in research (University of California, San Diego protocol 110483, and NHRC.2013.0023).

The authors wish to thank the Marines from the 1st and 5th Regiment who supported this effort. The authors declare no conflicts of interest.

Chapter 2 is a reprint of the published article, "Lumbar spine postures in Marines during simulated operational positions." Berry DB, Rodriguez-Soto AE, Su J, Gombatto SP, Shahidi B, Palombo L, Chung C, Kelly KR, Ward SR. *Journal of Orthopaedic Surgery,* [E pub ahead of print], 2017. The dissertation author was the primary investigator and author of this paper.

Table 2-1. Participant characteristics by intervertebral disc degeneration, and current and past low back pain. No significant differences were found between groups.

	Aggregate	Degeneration		Low Back Pain			
				"Are you currently experiencing LBP?"		"Have you ever experienced LBP?"	
		Yes = 33	No = 10	Yes = 16	No = 23	Yes = 28	No = 11
Age (years)	26.8 ± 6.4	27.6 ± 6.8	24.0 ± 3.7	26.9 ± 5.7	27.1 ± 7.4	27.7 ± 6.6	25.4 ± 6.6
Height (m)	1.78 ± 0.07	1.78 ± 0.07	1.76 ± 0.07	1.78 ± 0.07	1.78 ± 0.08	1.79 ± 0.07	1.77 ± 0.09
Weight (kg)	81.9 ± 9.8	83.8 ± 9.5	75.6 ± 8.6	81.8 ± 10.6	82.3 ± 10.0	82.5 ± 9.9	81.0 ± 11.2
BMI (kg/m^2)	25.9 ± 2.9	26.4 ±2.8	24.3 ±2.4	25.7 ± 3.1	26.1 ± 2.9	25.9 ± 2.8	26.0 ± 3.5

BMI, body mass index.

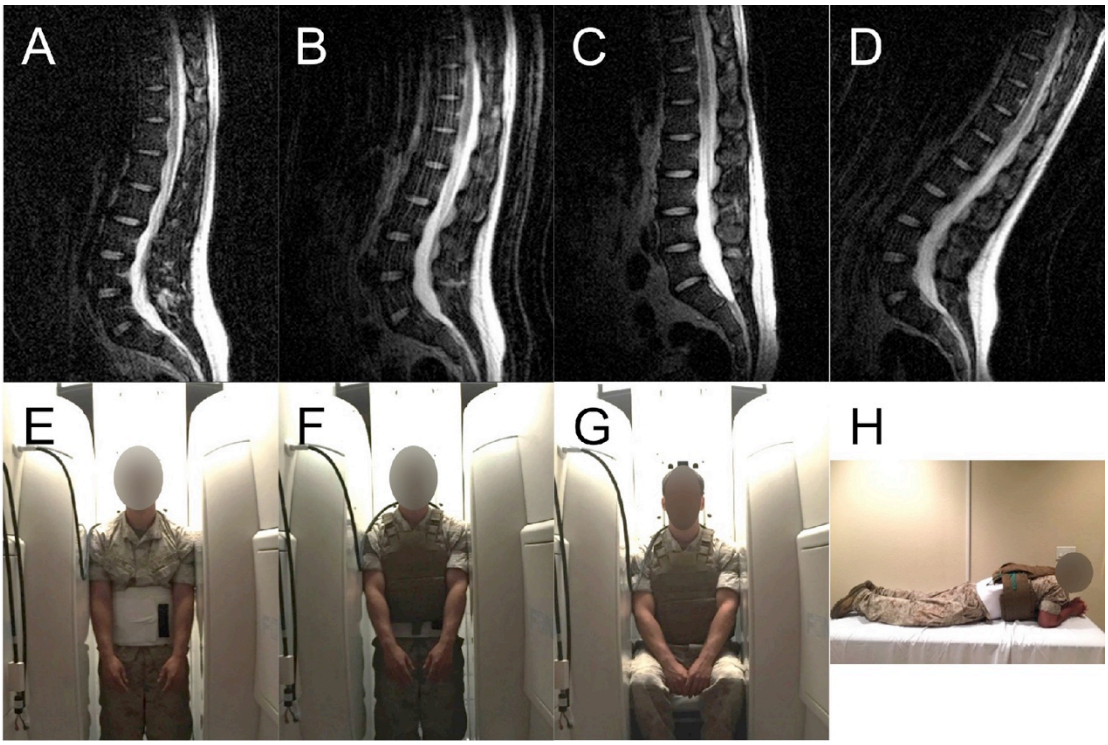

Figure 2-1. T2-weighted mid-sagittal magnetic resonance images (MRIs) of the lumbar spine (top) and photographs of Marines in the MRI scanner (bottom). Volunteers were scanned standing unloaded (A, E), standing with body armor (B, F), sitting with body armor (C, G), and prone on elbows with body armor (D, H).

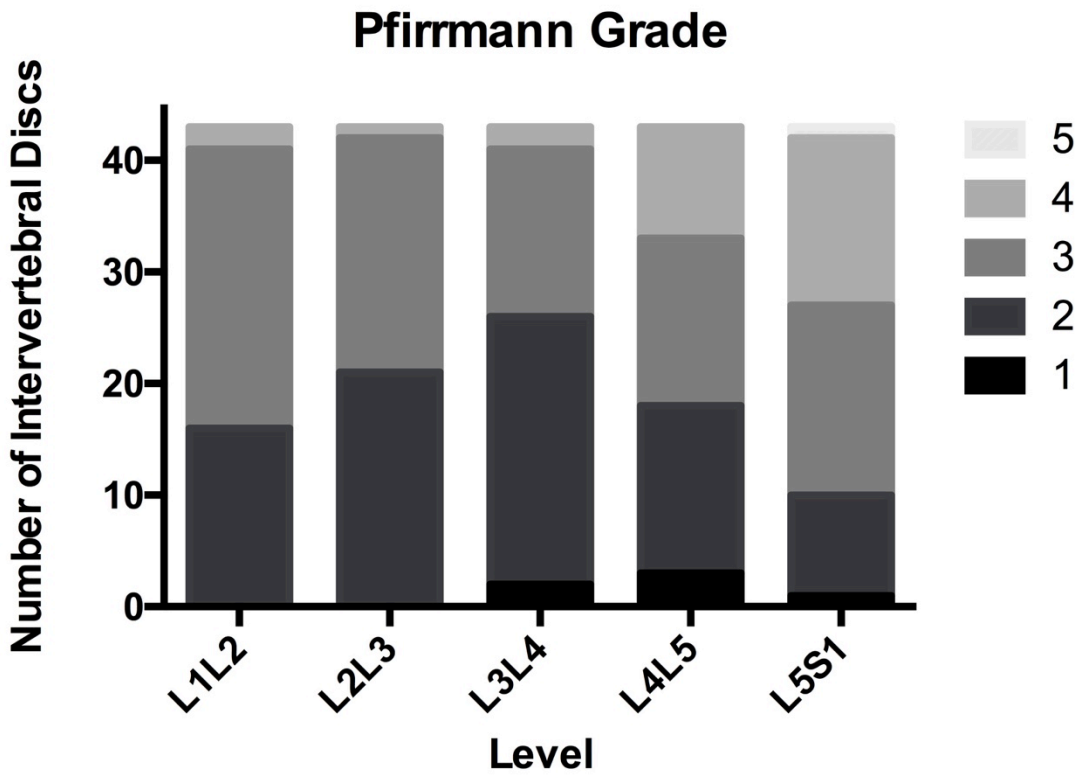

Figure 2-2. Distribution of Pfirmmann-graded intervertebral discs by level.

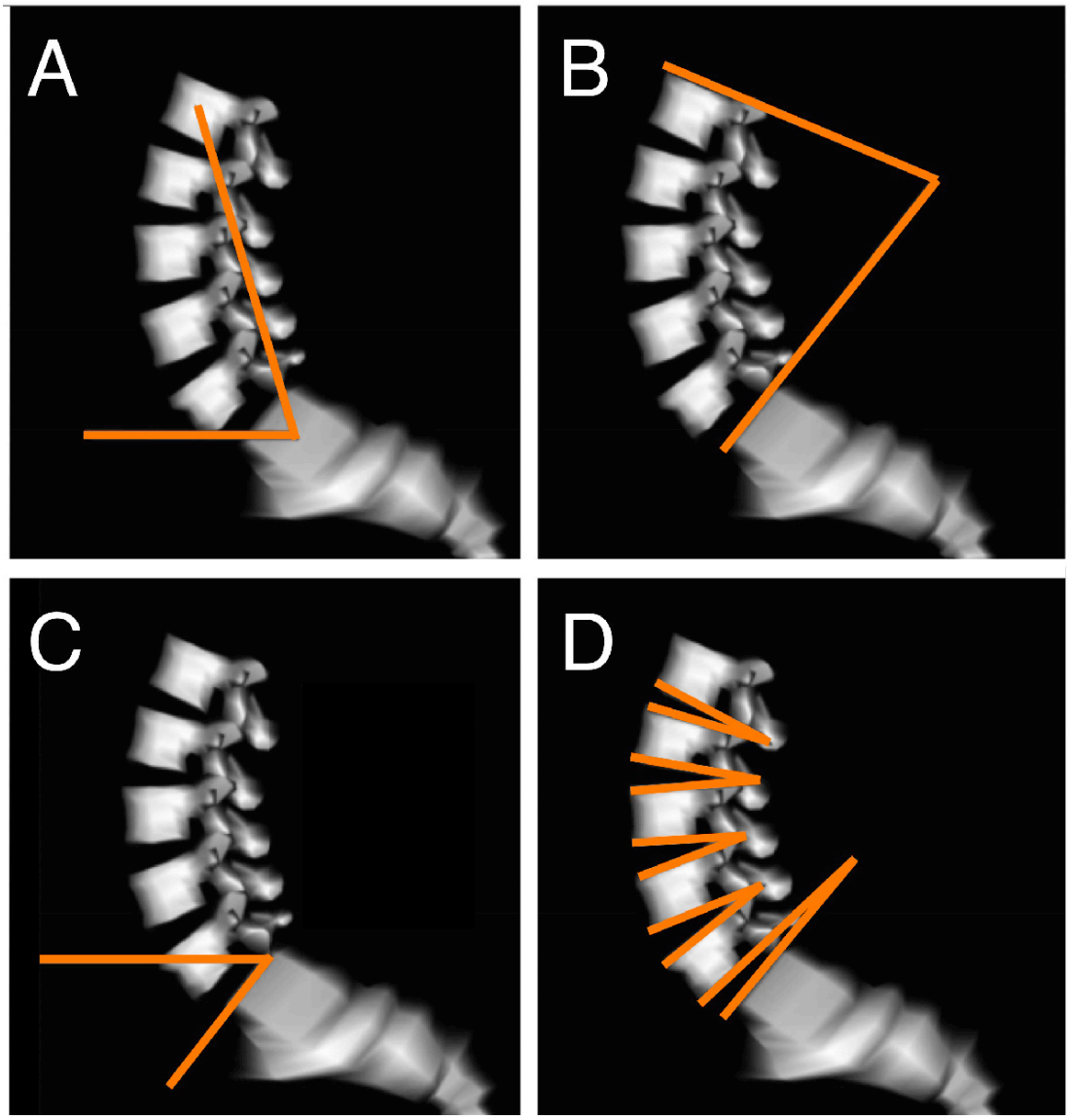

Figure 2-3. Schematic depicting lumbar spine postural measurements on a 3D model of the lumbar spine. Measurements included A.) Angle with respect to the horizontal to assess lumbar flexion/extension. B.) Sagittal Cobb angle to measure lumbar lordosis. C.) Sacral slope to assess rotation of the pelvis. D.) Intervertebral angles to provide a measurement of local lumbar lordosis.

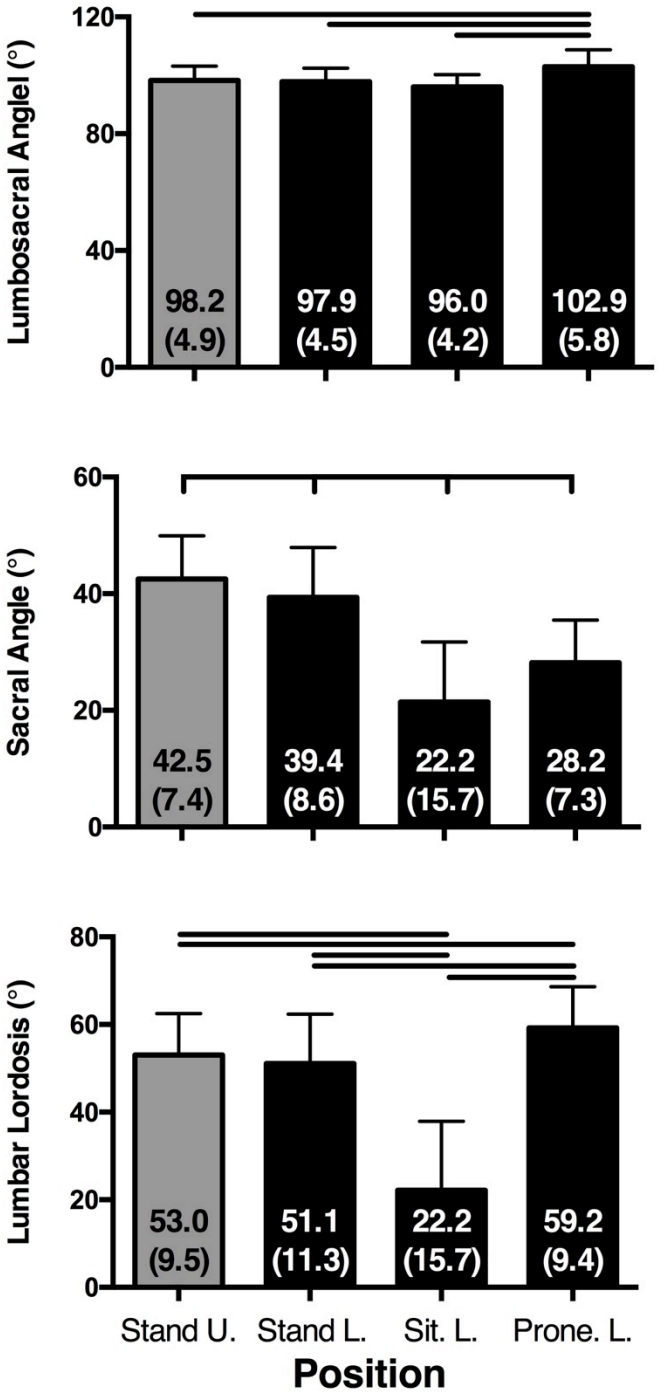

Figure 2-4. Global measures of lumbar spine posture. Angle with respect to horizontal (top), sacral slope (middle), Cobb angle (bottom). Statistically significant difference between measurements ($p < 0.05$) indicated by line. Data reported as mean (standard deviation).

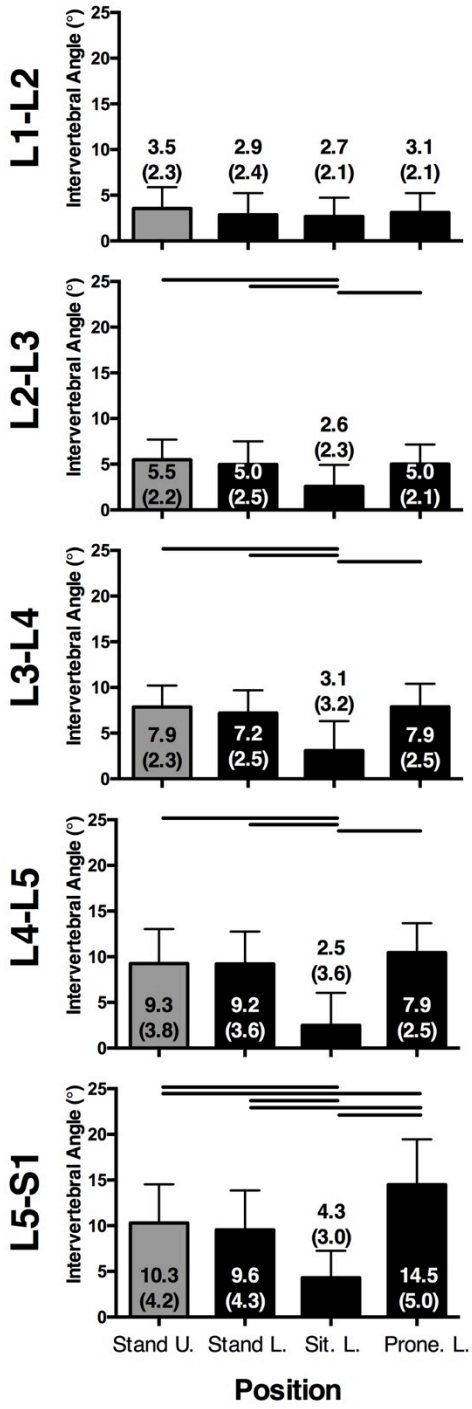

Figure 2-5. Local measures of lumbar spine posture. Intervertebral angles from L1–L2 (top) to L5–S1 (bottom) are shown. Statistically significant difference between measurements ($p < 0.05$) indicated by line. Data reported as mean (standard deviation).

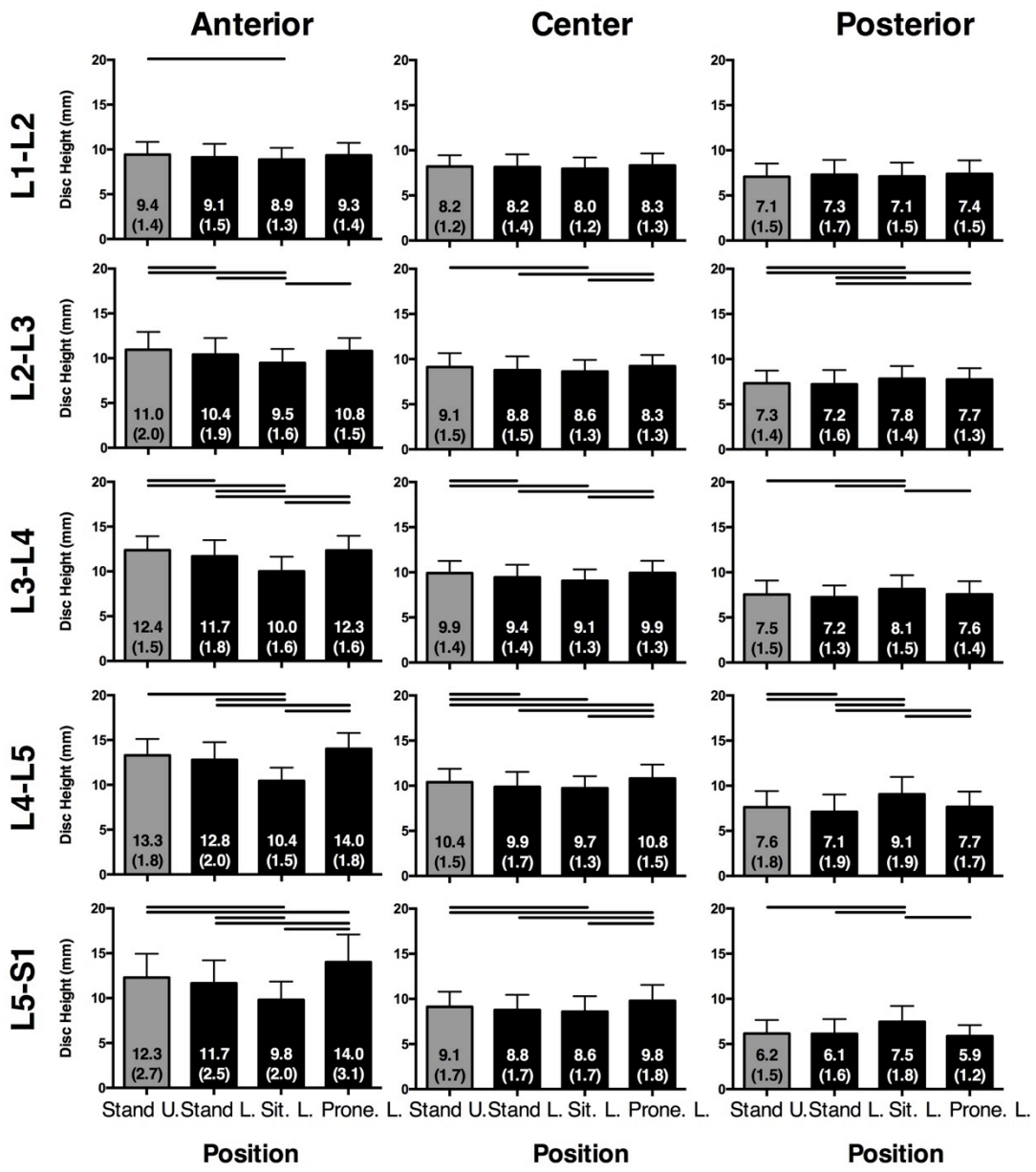

Figure 2-6. Anterior (left column), central (middle column), and posterior (right column) intervertebral distance measurements for each level of the lumbar spine. Intervertebral heights from L1–L2 (top) to L5–S1 (bottom) are shown. Statistically significant difference between measurements ($p < 0.05$) indicated by line. Data reported as mean (standard deviation).

2.8 REFERENCES

1. Andersson GB. Epidemiological features of chronic low-back pain. Lancet. 1999; 354: 581–585.

2. Daniele DOL, Elizabeth J. Absolute and relative morbidity burdens attributable to various illnesses and injuries, U.S. Armed Forces, 2013. MSMR. 2014; 21: 2–7.

3. Sinnott P, Dally S, Avoundjian T, Trafton J, Wagner T. 2013. Neck and Back Pain at the VA. Available from: http://www.hsrd.research.va.gov/for_researchers/cyber_seminars/archives/768-notes.pdf.

4. Yu W, Ravelo A, Wagner TH, Phibbs CS, Bhandari A, Chen S, Barnett PG. Prevalence and costs of chronic conditions in the VA health care system. Med Care Res Rev. 2003; 60: 146S–167S.

5. Martin BI, Deyo RA, Mirza SK, Turner JA, Comstock BA, Holligwort W, Sullivan SD. Expenditures and health status among adults with back and neck problems. JAMA. 2008; 299: 656–664.

6. Schoenfeld AJ, Nelson JH, Burks R, Belmont PJ Jr. 2011. Incidence and risk factors for lumbar degenerative disc disease in the United States military 1999-Mil Med; 2008l; 176: 1320–1324.

7. Luoma K, Riihimaki H, Luukkonen R, Raininko R, Viikari-Juntura E, Lammienen A. Low back pain in relation to lumbar disc degeneration. Spine. 2000; 25: 487–492.

8. Roy TC, Lopez HP, Piva SR. Loads worn by soldiers predict episodes of low back pain during deployment to Afghanistan. Spine. 2013; 38: 1310–1317.

9. Rodríguez-Soto AE, Jaworski R, Jensen A, Niederberger B, Hargens AR, Frank LR, Kelly KR, Ward SR. Effect of load carriage on lumbar spine kinematics. Spine. 2013 38: E783–E791.

10. Pelham TW, White H, Holt LE, Lee SW. The etiology of low back pain in military helicopter aviators: prevention and treatment. Work. 2004; 24: 101–110.

11. Jackson RP, McManus AC. Radiographic analysis of sagittal plane alignment and balance in standing volunteers and patients with low back pain matched for age, sex, and size. A prospective controlled clinical study. Spine; 1994; 19: 1611–1618.

12. Keorochana G, Taghavi CE, Lee KB, Yoo JH, Jiao JC, Fei Z, Wang JC. Effect of sagittal alignment on kinematic changes and degree of disc degeneration in the lumbar spine: an analysis using positional MRI. Spine. 2011; 36: 893–898.

13. Lao L, Daubs MD, Scott TP, Lord EL, Cohen JR, Yin R, Zhong G, Wang JC. Effect of disc degeneration on lumbar segmental mobility analyzed by kinetic magnetic resonance imaging. Spine. 2015; 40: 316–322.

14. Baecke JA, Burema J, Frijters JE. A short questionnaire for the measurement of habitual physical activity in epidemiological studies. Am J Clin Nutr. 1982; 36: 936–942.

15. Roland M, Fairbank J. The Roland–Morris Disability Questionnaire and the Oswestry Disability Questionnaire. Spine; 2000; 25: 3115–3124.

16. Pfirmmann, CW, Metzdorf A, Zanetti M, Holder J, Boos N. Magnetic resonance classification of lumbar intervertebral disc degeneration. Spine; 2001; 26: 1873–1878.

17. Iguchi T, Nishida K, Ozaki T, Kitagawa A, Tsumura N, Kakutani K, Yurube T, Kuroda R. Grade three disc degeneration is a critical stage for anterior spondylolisthesis in lumbar spine. Eur Spine J. 2012; 21: 2134–2139.

18. Kirkaldy-Willis WH, Farfan HF. Instability of the lumbar spine. Clin Orthop Relat Res. 1982; 165: 110–123.

19. Lee ES, Ko CW, Suh SW, Kumar S, Kang IK, Yang JH. The effect of age on sagittal plane profile of the lumbar spine according to standing, supine, and various sitting positions. J Orthop Surg Res. 2014; 9: 1–10.

20. Berry DB, Rodriguez-Soto AE, Tokunaga JR, Gombatto SG, Ward SR. An Endplate-Based Joint Coordinate System for Measuring Kinematics in Normal and Abnormally Shaped Lumbar Vertebrae. J Appl Biomech; 2015; 31: 499–503.

21. Rosset A, Spadola L, Ratib O. OsiriX: an open-source software for navigating in multidimensional DICOM images. J Digit Imaging. 2004; 17: 205–216.

22. Cobb J. 1948. Outline for the study of scoliosis. Instr Course Lect 5: 261–275.

23. Lord MJ, Small JM, Dinsay JM, Watkins RG. Lumbar lordosis. Effects of sitting and standing. Spine; 1997; 22: 2571–2574.

24. O'Sullivan PB. Lumbar segmental 'instability': clinical presentation and specific stabilizing exercise management. Man Ther. 2000; 5: 2–12.

25. O'Sullivan P. Diagnosis and classification of chronic low back pain disorders: maladaptive movement and motor control impairments as underlying mechanism. Man Ther. 2005; 10: 242–255.

26. Lis AM, Black KM, Korn H, Nordin M. Association between sitting and occupational LBP. Eur Spine J. 2007; 16: 283–298.

27. Lao L, Daubs MD, Takahashi S, Lord EL, Cohen JR, Zhong G, Wang JC. Kinetic magnetic resonance imaging analysis of lumbar segmental motion at levels adjacent to disc herniation. Eur Spine J. 2016; 1–8.

28. Dankaerts W, O'Sullivan P, Burnett A, Straker L. Differences in sitting postures are associated with nonspecific chronic low back pain disorders when patients are subclassified. Spine. 2016; 31: 698–704.

29. Neville CE, Murray LJ, Boreham CA, Gallagher AM, Twisk J, Robson PJ, Savage JM, Kemper HC, Ralston SH, Davey Smith G. Relationship between physical activity and bone mineral status in young adults: the Northern Ireland Young Hearts Project. Bone. 2002; 30: 792–798.

30. Rodríguez-Soto AE, Berry DB, Palombo L, Valaik E, Kelly KR, Ward SR. The effect of load magnitude and distribution on lumbar spine posture in active-duty Marines. Spine. 2016; [Epub ahead of print].

CHAPTER 3: THE RELATIONSHIP BETWEEN SKELETAL MUSCLE KINEMATICS AND MUSCLE PHYSIOLOGY IN ACTIVE DUTY MARINES

3.1 ABSTRACT

Study Design: Cross-sectional.

Background: The relationship between lumbar spine posture and muscle structure is not well understood.

Objectives: Investigate the predictive capacity of muscle structure on lumbar spine posture in active-duty Marines.

Methods: Marines (n=31) were scanned using an upright MRI scanner in the following positions: standing, standing with body armor, sitting with body armor, and prone on elbows with body armor. Cobb angle, horizontal angle, and sacral angle were measured. Marines were then scanned unloaded in supine using a supine MRI scanner. The imaging protocol consisted of: 1) T2 IVD mapping, 2) high-resolution anatomical, 3) fat-water separation, and 4) diffusion tensor imaging to quantify disc hydration and muscle volume, fat fraction and restricted diffusion profiles in the lumbar muscles. A stepwise multiple linear regression model was used to identify physiologic measures predictive of lumbar spine posture.

Results: The multiple regression model demonstrated that fractional anisotropy (FA) of the erector spinae was a significant predictor of lumbar posture for 7/18 dependent variables measured and explained 20–35% of the variance in each model.

Conclusions: Decreased FA of the erector spinae (associated with muscle fiber size) resulted in decreased lordosis, decreased lumbosacral extension, and decreased anterior pelvic tilt, which functionally decreases lower lumbar sheer stress and may be more protective against developing injury or low back pain while load bearing. The ability of FA to determine postural responses in several positions along with the absence of association between muscle volume and lumbar spine posture suggests that muscle quality, but not quantity is an important predictor of lumbar spine posture.

3.2 INTRODUCTION

Low back pain (LBP) is the second most common musculoskeletal complaint among civilians, affecting 70%-85% of the population at some point in their lives[1]. LBP can be idiopathic, provoked by acute injury, or due to structural abnormalities in the spinal column. In the military, more medical encounters are due to back pain than any other medical condition[10]. Military members are a highly active population, who are often required to carry heavy loads. Studies investigating how Marines adapt to these loads suggest they routinely operate under conditions that put them at risk for developing lumbar musculoskeletal injury[22, 23]. Therefore, increased rates of reported LBP in Marines may be attributed to pathophysiologic changes of the lumbar spine structures, as a result of the heavy loads and unusual postures experienced in training and in combat.

The muscles of the lumbar spine are crucial for stabilizing and supporting the upper trunk, especially during the dynamic loading conditions experienced by military members. The multifidus muscle is considered one of the primary muscular stabilizers of the lumbar spine; due to its ability to produce high forces over a narrow range of

lengths[33]. A commonly used metric to roughly estimate the force generating potential of the multifidus is muscle cross sectional area or volume, which is known to decrease in size with age or injury and can be measured non-invasively with computed tomography, magnetic resonance imaging (MRI), or ultrasound[6, 7]. However, physiological cross sectional area is a much better metric of predicting muscle force as it takes into account measures of muscle architecture such as pennation angle and normalized fiber length, which are difficult to measure with noninvasive imaging techniques. With injury and age, replacement of muscle tissue with adipose and fibrotic tissue is typically observed compared to healthy muscle, further decreasing the overall volume of functional contractile tissue in the muscle[6, 24]. As pathogenic muscle becomes more fibrotic and contains more adipose tissue, the active and passive force generating potential of the whole muscle changes, which can directly negatively effect whole joint stability and range of motion[16, 20, 27, 34].

Changes to the orientation and position of bony structures of the spinal column are often observed simultaneously with aforementioned changes in muscle composition[15, 26, 28]. With age, gross changes in spinal posture such as decreased lumbar lordosis, increased lumbar flexion, and increased pelvic tilt are typically observed[11, 12, 14, 30]. Decreased segmental range of motion has also been measured at vertebral levels with intervertebral disc (IVD) degeneration[11, 13], which is defined as decreased hydration of the nucleus pulposus with accompanying disc height loss[19]. However, changes in muscle structure, lumbar posture and IVD health are not independent of one another, and their effects are confounded by age, sex, activity level, and the timing of disease progression. A non-invasive tool that can be used to measure and predict maladaptive posture in

operational conditions from musculoskeletal health would allow clinicians to tailor rehabilitation protocols to prevent injury, and could potentially be used to predict individuals at risk for lumbar spine injury. Therefore, the purpose of this study is to investigate the predictive capacity of muscle structure, IVD health and anthropometric measures on lumbar spine posture in active-duty Marines.

3.3 METHODS

The University of California, San Diego and Naval Health Research Center Institutional Review Boards approved this study, and all volunteers gave oral and written consent to participate.

3.3.1 Upright MRI-Imaging

Marines were scanned using an upright 0.6T MRI scanner (Upright Multi-Position MRI, Fonar Corporation, Melville, NY, USA) and a planar coil. An elastic band was used to hold the coil against the volunteer's lumbar spine between the L1-S1 levels while standing. The band was secured to hold the coil in place while not altering the volunteer's natural position. A three-plane localizer and sagittal T2-weighted images were acquired[4].

3.3.2 Upright MRI-Load Carriage and Position Tasks

Marines were scanned in the following positions: standing without load (St.U.), standing with body armor (St.L.; 11.3 kg), sitting with body armor (Si.L)., and prone on elbows with body armor (P.L.). Positions with external load were randomized to control for the cumulative effects of loading or time. The positions chosen are common static positions Marines are often required to maintain for extended periods of time depending on military occupational specialty and are often noted as provoking LBP. Load

magnitude (11.3kg) was chosen based on use of body armor, which is minimum protective equipment that Marines are required to wear at all times during military operations/training. Marines were not provided instruction on how to assume each position, but were asked to hold each position steady for the duration of the MRI acquisition.

3.3.3 Upright MRI-Postural Measurements

Postural measurements were generated from upright MRI images in each position, using a previously validated algorithm[3]. Briefly, digital seed points were manually placed on the corners of the vertebral body and on the posterior elements of each vertebra using OsiriX[21]. The location of the seed points were imported into Matlab (Mathworks Inc., Natick, MA) and used to define an endplate-based joint coordinate system applied to the superior and inferior endplate of each vertebrae (L1-S1).

Global measurements of lumbar spine posture were calculated for each position to characterize the posture of the lumbar spine. Global measures included: angle with respect to the horizontal to assess lumbosacral flexion/extension, sacral slope to assess sacral tilt, and sagittal Cobb angle to assess lumbar lordosis (Fig. 1). The change in global measurements from standing unloaded to standing loaded (Δload), and sitting loaded to prone loaded (Δposition) were additionally calculated to determine lumbar kinematics in response to load and dynamic movement, respectively.

3.3.4 Supine MRI-Imaging

MRI's of the lumbar spine (L1-S1) of this group of Marines were acquired using a 3T MRI scanner (GE MR350 Discovery, GE Healthcare) and spine array coil. The imaging protocol consisted of 1) an anatomical, 2) fat-water separation scan, 3) diffusion tensor imaging (DTI) of the lumbar spine and 4) T2 mapping of each lumbar IVD.

3.3.5 Supine MRI-Lumbar Physiology Measurements

Anatomical images were imported into Osirix (Switzerland) for semi-automatic segmentation. The contour of the multifidus, erector spinae group, psoas and quadratus lumborum muscles was manually traced from L1 to S1 lumbar levels every 10 images; these were interpolated to generate the remaining contours. This process was followed by visual inspection of the resulting contours, which were manually corrected as needed. The resulting segmentations were used to generate masks to quantify muscle volumes, fat fraction and diffusion properties.

Images acquired using the fat-water separation sequence yield two sets of images: one where both fat and water MRI signals are in phase and one where they are out of phase. This allows for isolating the independent contributions of water (S_W) and fat (S_F) to the total MR signal. These data were then used to quantify fat fraction (FF) of the multifidus and erector spinae group with the following relationship:

$$FF = \frac{S_F}{S_w + S_F}$$

The diffusion tensor was fitted using AFNI (NIH, Bethesda, MD) function 3dDWItoDT[5]. Mean diffusivity (MD), fractional anisotropy (FA), and the three eigenvalues $\lambda_{1\text{-}3}$ of the diffusion tensor are reported. MD describes the average restricted diffusion coefficient of the three eigenvalues of the diffusion and, FA is a unitless measurement from 0 to 1 that indicates the shape of the diffusion tensor. A FA value of 0 corresponds to isotropic diffusion (unrestricted) and a FA value of 1 corresponds to diffusion along a line (highly restricted). $\lambda_{1\text{-}3}$ define the magnitude of diffusion along (λ_1) and radial to ($\lambda_{2,3}$) the main direction of the muscle fiber.

The T_2 values for each IVD were estimated by fitting the magnitude of the multi-echo data to a mono-exponential decay:

$$S_i = S_o e^{-t/T2}$$

IVD health is often assessed by qualitatively assessing disc hydration from T2 weighted MRI's. Quantitative T2 mapping provides a quantitative measurement of how hydrated an IVD is; T2 is inversely proportional to Pfirmmann grade[29].

3.3.6 Statistical Analysis

Dependent variables were global postural measurements (angle with respect to the horizontal, saggital Cobb angle, and sacral angle) for all positions (standing unloaded, standing with load, sitting with load, prone on elbows with load) and the change in load and flexion-extension positions (Δload, Δposition).

An *apriori* approach was used to minimize the number of independent variables input into each model (Fig. 2). First, independent variables were empirically grouped into 3 separate domains; muscle structure (volume, FF, FA, MD, λ_{1-3}), IVD health (T2-relaxation of each disc), and anthropometric (age, weight, height, BMI) measures. Hierarchical cluster analysis was used to verify domain groupings. Variables that did not cluster were then sorted into like variables (eigenvectors) using principle components analysis (PCA). Within each eigenvector, Pearson's correlation was used to remove collinear variables ($r>0.8$). For collinear variables, the variable with the smallest eigenvector value was removed in order to remove redundancy of variance across variables. Remaining variables were entered into a stepwise multiple linear regression model for each dependent variable separately, to identify physiologic measures that are predictive of lumbar spine posture. Collinearity was also verified at this point by variance

inflation factor. If a variable had a variance inflation factor >10 it was removed from the model. Statistical analyses were performed using SPSS Statistics software (version 20.0, IBM, Armonk, NY).

3.4 RESULTS

3.4.1 Volunteer Demographics

Forty-three male Marines (mean age = 26.8 ± 6.4 years, height = 1.8 ± 0.1 meters, weight = 82.0 ± 9.9 kg) volunteered for this study. Two subjects dropped out of this study during supine imaging due to claustrophobia in the MRI scanner. Additionally, DTI datasets of 10 subjects were deemed unusable due to breathing artifact. Therefore, 31 Marines were included in this analysis (mean age = 27.3 ± 6.9 years, height = 1.8 ± 0.1 meters, weight = 80.6 ± 8.7kg). Marines excluded from the study had no differences in any anthropometric measures than Marines included in the study. Of these volunteers, 10 Marines self-reported experiencing low back pain at the time of the scan.

3.4.2 Regression Model

After initial grouping of independent variables, collinearity resulted in removal of eight of the twenty-nine independent variables from the model (Fig. 2). Collinear variables that were removed included diffusion measurements from either multifidus or erector spinae, erector spinae fat fraction and BMI. Results of the multiple regression demonstrated that FA of the erector spinae was a significant predictor of lumbar posture for 7/18 dependent variables measured and explained 20%-35% of the variance for each outcome (Table 1). In general, increased FA in erector spinae was predictive of increased lumbar lordosis, increased lumbosacral flexion, and increased pelvic tilt. Additionally, decreased T2 relaxation of the L4-L5 IVD was a significant predictor of increased

lumbosacral extension when standing unloaded ($p=.025$, $R^2=.192$). When prone on elbows, increasing subject weight was a significant predictor of increased lumbar lordosis ($p=.016$, $R^2=.219$). No muscle volume, muscle microstructure, IVD health or anthropometric measures were significant predictors of posture when subjects were sitting loaded.

3.5 DISCUSSION

In this study, we evaluated the relationship between lumbar spine posture and muscle structure, IVD health and anthropometric measures in 31 active duty male Marines in simulated, relevant operational positions and loading conditions. FA of the erector spinae was a significant predictor of 7/18 measures of lumbar spine posture across several different positions. For the standing loaded condition, FA of the erector spinae was a significant predictor of all three measures of lumbar posture; Marines with increased FA of the erector spinae, had a more lordotic, extended lumbar posture with greater sacral tilt. Muscle volume was not a significant predictor of any postural measurements, despite being a commonly used proxy for muscle strength[8, 15]. Together, the ability of FA to predict postural behavior in several positions along with the absence of association between muscle volume and lumbar spine posture suggests that muscle quality, but not quantity is an important predictor of lumbar spine posture.

DTI is an MRI technique that measures the restricted diffusion of water in tissues with anisotropic microstructure[2]. As the sarcolemma is believed to be the primary barrier to diffusion, DTI is believed to be most sensitive to changes in fiber size because radial diffusion of water across a muscle fiber is more restricted (by the sarcolemma) than

longitudinal diffusion within a muscle fiber[31, 32]. While it has been shown that FA and fiber area are inversely related, it is important to note the exact relationship has not been validated. However, it is well established that muscle fiber area and isometric force are directly related[17] to these measurements. Therefore, it follows that there is a likely an inverse relationship between FA and isometric force generating capacity of muscle. As such, as FA increases, the force generating capacity of a muscle decreases (i.e. the muscle is weaker).

Two unique relationships between posture and muscle structure were found in this study: 1) erector spinae and not multifidus and 2) muscle quality not muscle quantity were found to be a significant predictors of lumbar posture. First, FA of the multifidus and the erector spinae were found to be collinear, with FA of the erector spinae a stronger descriptor of the eigenvector from the PCA. Therefore, multifidus was not entered into the final statistical model. To verify FA of the multifidus was not removed from the model because it had less variability than FA of the erector spinae, coefficient of variation was calculated for both variables. FA of the erector spinae had less variability relative to the mean than FA of the multifidus (0.07 vs. 0.08), further supporting FA of the multifidus as a stronger descriptor of the eigenvector. This finding suggests that while the multifidus acts as the main stabilizer of the spine, the erector spinae plays a critical role in whole lumbar posture. Second, while muscle volume is proportional to muscle strength, muscle architecture has been shown to be a more accurate predictor of muscle force generating capacity. Clinically, the findings from this study are important because they suggest that microstructural quality of the lumbar muscles is more important to whole lumbar posture in functionally loaded positions than the quantity or volume of

muscle. This is not surprising given that measures of whole muscle size and volume are confounded by non-contractile tissue, such as fat and fibrosis. Importantly, FA may be a non-invasive composite measure of how much functional contractile tissue is present in a whole muscle, and it also seems to explain much of the variance postural responses to load.

In this study, T2 of the L4-L5 IVD was found to be inversely proportional to lumbosacral extension when Marines were standing without load. This suggests that Marines with decreased IVD T2 values (increased IVD degeneration) at L4-L5 have increased lumbosacral extension. Previously, using the Pfirmmann grading scale, we reported no significant difference in lumbosacral extension in Marines when categorized by degeneration at L5-S1 (Pfirmmann grade > 2)[4]. As L5-S1 is the base of support of the lumbar spine, it was assumed that degeneration at this level would have whole lumbar postural consequences. However, our findings demonstrate L4-L5 IVD health also has a large effect on whole lumbar posture and therefore should be considered an important structural level for whole lumbar stability. The finding that single-level disc health has the potential to influence lumbosacral flexion reiterates the importance of the lower lumbar spine as a transition zone of load between the trunk and the body. Changes to the health of this region has the potential to affect stability of the trunk.

Several studies have previously attempted to determine the relationship between lumbar lordosis and BMI. It appears increased lumbar lordosis might be found in subjects with increased BMI[9, 18], however other studies have shown no difference[35]. In this study, weight and BMI were found to be collinear, with weight being the stronger predictor of the eigenvector from PCA. Therefore BMI was dropped from the final statistical model.

However, this is likely due to a larger variance in subject weight than BMI in this relatively homogeneous population. If a more representative cross section of the population was used, these findings may be different. We found that heavier Marines exhibited increased lumbar lordosis only when prone on elbows loaded, which is similar to previously reported findings.

In this study, we made several attempts to decrease the complexity of this model in order to decrease the amount of type I error which can be associated from making multiple comparisons. First, we chose not to include individual vertebral level measures of muscle structure or lumbar posture. Second, we chose to remove collinear variables with clustering and PCA analysis to minimize the number of independent variables representing similar constructs that were entered into the model. Third, we evaluated forward, backward and stepwise multiple linear regression models to determine which model was the most conservative approach. Results were the same with forward and stepwise elimination techniques, and backward elimination allowed for several more independent variables to be retained in the model, suggesting it was the least conservative regression approach. Therefore, we chose to use a stepwise multiple linear regression technique as it appeared to be the most conservative model.

3.6 CONCLUSION

This study is the first to measure the predictive capacity of lumbar muscle structure, IVD health and anthropometric measures on lumbar spine posture in different positions. It was found that FA of the erector spinae was a significant predictor of several lumbar postural measures. In general, decreased FA of the erector spinae resulted in

decreased lordosis, decreased lumbosacral extension, and decreased anterior pelvic tilt. This posture results in decreased shear stress at lower lumbar levels and may be considered a more protective posture for preventing injury and LBP while load bearing in the lumbar spine[25]. Decreased FA of the erector spinae can be physiologically interpreted as larger muscle fibers with more capacity to generate force. Due to the intense training and demands of their jobs, the Marines in this study were extremely active, and trained on how to adapt their posture in different positions while wearing body armor to minimize their risk of injury. Therefore, these findings may not translate to a civilian population. Future studies should apply these methods to determine what features of muscle structure, IVD health and anthropometric data can predict lumbar posture in healthy civilians and civilians with low back pain.

3.7 ACKNOLEDGEMENTS

I am a military service member (or employee of the U.S. Government). This work was prepared as part of my official duties. Title 17 U.S.C. § 105 provides the "Copyright protection under this title is not available for any work of the United States Government." Title 17 U.S.C. § 101 defines a U.S. Government work as work prepared by a military service member or employee of the U.S. Government as part of that person's official duties.

This manuscript was supported by the U.S. Army Medical Research Acquisition Activity, Award No. W81XWH-13-2-0043 (work unit no. 1305). This work was supported by DoD grant PR120576 (SRW & KK). The views expressed in this article are those of the authors and do not necessarily reflect the official policy or position of the

Department of the Navy, Department of the Army, Department of the Air Force, Department of Veterans Affairs, Department of Defense, or the U.S. Government. Approved for public release; distribution unlimited.

Human subjects participated in this study after giving their free and informed consent. This research has been conducted in compliance with all applicable federal regulations governing the protection of human subjects in research (University of California, San Diego protocol 110483, and NHRC.2013.0023).

The authors wish to thank the Marines from the 1st and 5th Regiment who supported this effort. The authors declare no conflicts of interest.

Chapter 3, in full, is currently being prepared for submission for the publication of the material as it may appear in the Journal of Orthopaedic and Sports Physical Therapy, 2017, Berry DB, Shahidi B, Rodriguez-Soto AE, Hughes-Austin JM, Kelly KR, Ward SR. The dissertation author was the primary investigator and author of this paper.

Table 3-1. Results from stepwise multiple linear regression

Dependent Variables	Significant Independent Variable(s)	Standardized Beta Coefficient	R^2	p
Cobb Angle: Standing Unloaded	none	-	-	-
Cobb Angle: Standing Loaded	Erector Spinae Fractional Anisotropy	0.453	0.205	0.020
Cobb Angle: Sitting Loaded	none	-	-	-
Cobb Angle: Prone on Elbows Loaded	Weight	0.468	0.219	0.016
Cobb Angle: Δ Load	none	-	-	-
Cobb Angle: Δ Position	none	-	-	-
Angle w.r.t. Horizontal: Standing Unloaded	T2-L4/L5	-0.439	0.192	0.025
Angle w.r.t. Horizontal: Standing Loaded	Erector Spinae Fractional Anisotropy	0.514	0.264	0.007
Angle w.r.t. Horizontal: Sitting Loaded	none	-	-	-
Angle w.r.t. Horizontal: Prone on Elbows Loaded	Erector Spinae Fractional Anisotropy	-0.480	0.230	0.013
Angle w.r.t. Horizontal: Δ Load	none	-	-	-
Angle w.r.t. Horizontal: Δ Position	Erector Spinae Fractional Anisotropy	0.455	0.207	0.020
Sacral Angle: Standing Unloaded	Erector Spinae Fractional Anisotropy	0.442	0.195	0.024
Sacral Angle: Standing Loaded	Erector Spinae Fractional Anisotropy	0.587	0.345	0.002
Sacral Angle: Sitting Loaded	none	-	-	-
Sacral Angle: Prone on Elbows Loaded	Erector Spinae Fractional Anisotropy	0.562	0.316	0.003
Sacral Angle: Δ Load	none	-	-	-
Sacral Angle: Δ Position	none	-	-	-

Δ Load: Standing Unloaded-Standing Loaded. Δ Position: Sitting Loaded-Prone on Elbows Loaded

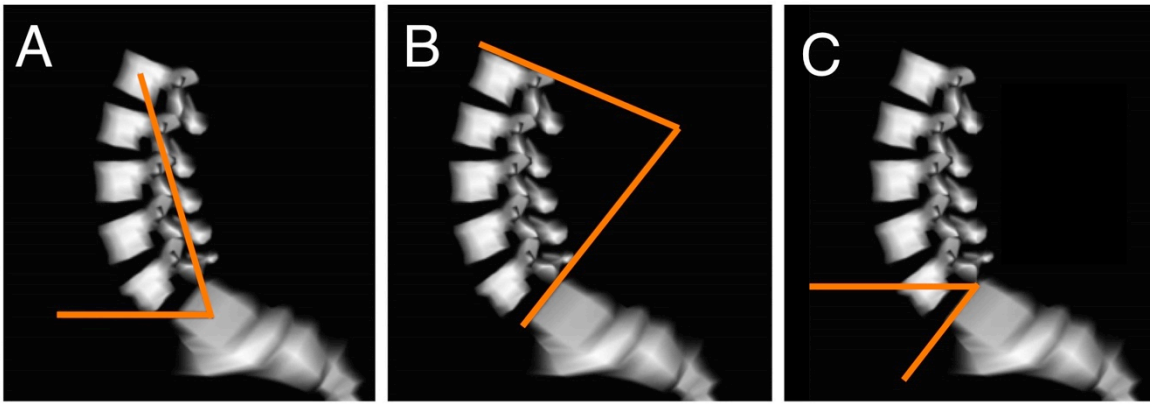

Figure 3-1. Schematic depicting lumbar spine postural measurements on a 3D model of the lumbar spine. Measurements included A.) Angle with respect to the horizontal to assess lumbar flexion/extension. B.) Sagittal Cobb angle to measure lumbar lordosis. C.) Sacral slope to assess rotation of the pelvis.

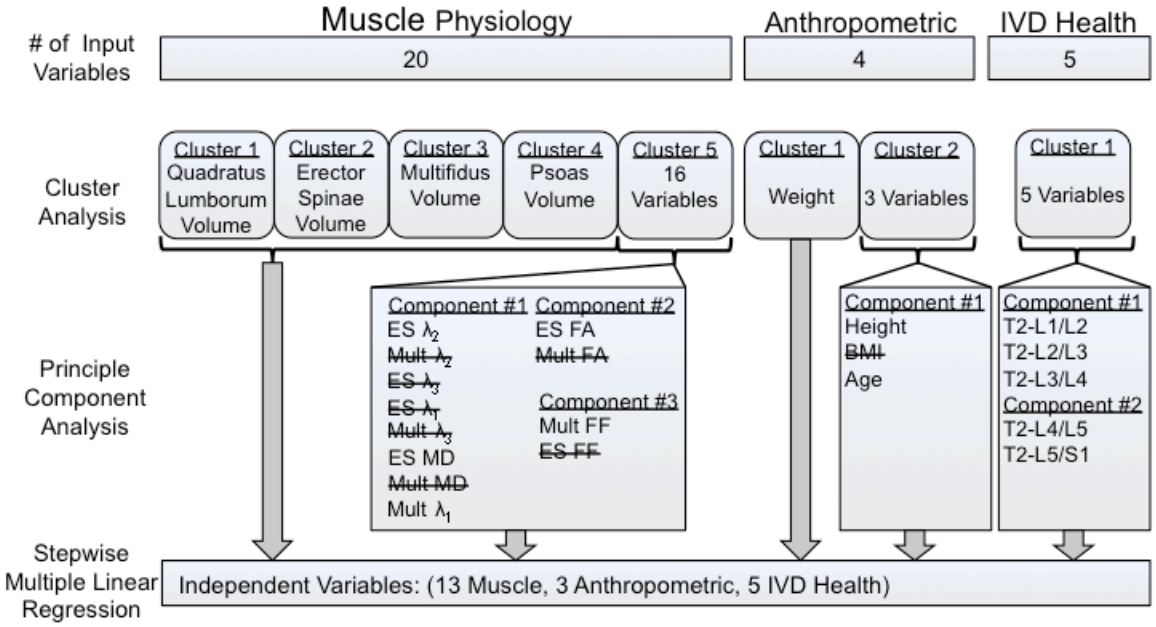

Figure 3-2. Schematic depicting the reduction of collinear independent variables for input into the stepwise multiple regression model. Initially, models were sorted into measures of muscle physiology, anthropometric measures and intervertebral disc (IVD) health. Cluster analysis was used to identify measures that were similar to other measures. For similar variables, principle components analysis was used to separate like variables into groups (components). Within each component, Pearson's correlations were used to identify collinear variables. If two variables were collinear ($r>0.8$ or variance inflation factor>10), the variable with the weaker contribution to the eigenvector was removed (crossed out).

3.8 REFERENCES

1. Andersson GB. Epidemiological features of chronic low-back pain. The lancet. 1999;354:581-585.

2. Basser PJ, Mattiello J, LeBihan D. MR diffusion tensor spectroscopy and imaging. Biophysical journal. 1994;66:259.

3. Berry DB, Rodríguez-Soto AE, Tokunaga JR, Gombatto SP, Ward SR. An Endplate-Based Joint Coordinate System for Measuring Kinematics in Normal and Abnormally-Shaped Lumbar Vertebrae. Journal of applied biomechanics. 2015;31:499-503.

4. Berry DB, Rodríguez-Soto AE, Su J, Gombatto SP, Shahidi B, Palombo L, Chung C, Jensen A, Kelly KR, Ward SR. Lumbar spine postures in Marines during simulated operational positions. Journal of Orthopaedic Research. 2017.

5. Cox RW. AFNI: software for analysis and visualization of functional magnetic resonance neuroimages. Computers and Biomedical research. 1996;29:162-173.

6. Demoulin C, Crielaard J-M, Vanderthommen M. Spinal muscle evaluation in healthy individuals and low-back-pain patients: a literature review. Joint Bone Spine. 2007;74:9-13.

7. Fortin M, Macedo LG. Multifidus and paraspinal muscle group cross-sectional areas of patients with low back pain and control patients: a systematic review with a focus on blinding. Physical therapy. 2013;93:873.

8. Fukunaga T, Miyatani M, Tachi M, Kouzaki M, Kawakami Y, Kanehisa H. Muscle volume is a major determinant of joint torque in humans. Acta Physiologica. 2001;172:249-255.

9. Guo J, Zhang G. Effect of BMI and WHR on lumbar lordosis and sacrum slant angle in middle and elderly women. China journal of orthopaedics and traumatology. 2008;21:30-31.

10. J. DDE. Absolute and relative morbidity burdens attributable to various illnesses and injuries, U.S. Armed Forces. MSMR. 2014;21:2-7.

11. Keorochana G, Taghavi CE, Lee KB, Yoo JH, Liao JC, Fei Z, Wang JC. Effect of sagittal alignment on kinematic changes and degree of disc degeneration in the lumbar spine: an analysis using positional MRI. Spine. 2011;36:893-898.

12. Kim YB, Kim YJ, Ahn YJ, Kang GB, Yang JH, Lim H, Lee SW. A comparative analysis of sagittal spinopelvic alignment between young and old men without localized disc degeneration. European Spine Journal. 2014;23:1400-1406.

13. Lao L, Daubs MD, Scott TP, Lord EL, Cohen JR, Yin R, Zhong G, Wang JC. Effect of disc degeneration on lumbar segmental mobility analyzed by kinetic magnetic resonance imaging. Spine. 2015;40:316-322.

14. Mac-Thiong J-M, Roussouly P, Berthonnaud E, Guigui P. Age-and sex-related variations in sagittal sacropelvic morphology and balance in asymptomatic adults. European Spine Journal. 2011;20:572.

15. Meakin JR, Fulford J, Seymour R, Welsman JR, Knapp KM. The relationship between sagittal curvature and extensor muscle volume in the lumbar spine. Journal of anatomy. 2013;222:608-614.

16. Meyer GA, Lieber RL. Elucidation of extracellular matrix mechanics from muscle fibers and fiber bundles. Journal of biomechanics. 2011;44:771-773.

17. Minamoto VB, Hulst JB, Lim M, Peace WJ, Bremner SN, Ward SR, Lieber RL. Increased efficacy and decreased systemic-effects of botulinum toxin A injection after active or passive muscle manipulation. Developmental Medicine & Child Neurology. 2007;49:907-914.

18. Murrie V, Dixon A, Hollingworth W, Wilson H, Doyle T. Lumbar lordosis: study of patients with and without low back pain. Clinical Anatomy. 2003;16:144-147.

19. Pfirrmann CW, Metzdorf A, Zanetti M, Hodler J, Boos N. Magnetic resonance classification of lumbar intervertebral disc degeneration. Spine. 2001;26:1873-1878.

20. Pontén E, Fridén J, Thornell LE, Lieber RL. Spastic wrist flexors are more severely affected than wrist extensors in children with cerebral palsy. Developmental Medicine & Child Neurology. 2005;47:384-389.

21. Rosset A, Spadola L, Ratib O. OsiriX: an open-source software for navigating in multidimensional DICOM images. Journal of digital imaging. 2004;17:205-216.

22. Roy TC, Knapik JJ, Ritland BM, Murphy N, Sharp MA. Risk factors for musculoskeletal injuries for soldiers deployed to Afghanistan. Aviation, space, and environmental medicine. 2012;83:1060-1066.

23. Roy TC, Lopez HP, Piva SR. Loads worn by soldiers predict episodes of low back pain during deployment to Afghanistan. Spine. 2013;38:1310-1317.

24. Shahidi B, Parra CL, Berry DB, HUbbard JC, Gombatto S, Zlomislic V, Allen RT, Hughes-Austin J, Garfin S, Ward SR. Contribution of Lumbar Spine Pathology and age to Paraspinal Muscle Size and fatty Infiltration. Spine. 2016.

25. Shirazi-Adl A, El-Rich M, Pop D, Parnianpour M. Spinal muscle forces, internal loads and stability in standing under various postures and loads—application of kinematics-based algorithm. European spine journal. 2005;14:381-392.

26. Sinaki M, Itoi E, Rogers JW, Bergstralh EJ, Wahner HW. Correlation of Back Extensor Strength With Thoracic Kyphosis and Lumbar Lordosis in Estrogen-Deficient Women1. American journal of physical medicine & rehabilitation. 1996;75:370-374.

27. Smith LR, Lee KS, Ward SR, Chambers HG, Lieber RL. Hamstring contractures in children with spastic cerebral palsy result from a stiffer extracellular matrix and increased in vivo sarcomere length. The Journal of physiology. 2011;589:2625-2639.

28. Sparrey CJ, Bailey JF, Safaee M, Clark AJ, Lafage V, Schwab F, Smith JS, Ames CP. Etiology of lumbar lordosis and its pathophysiology: a review of the evolution of lumbar lordosis, and the mechanics and biology of lumbar degeneration. Neurosurgical focus. 2014;36:E1.

29. Stelzeneder D, Welsch GH, Kovács BK, Goed S, Paternostro-Sluga T,Vlychou M, Friedrich K, Mamisch TC, Trattnig S. Quantitative T2 evaluation at 3.0 T compared to morphological grading of the lumbar intervertebral disc: a standardized evaluation approach in patients with low back pain. European journal of radiology. 2012;81:324-330.

30. Sullivan MS, Dicknison C. The Influence of Age and Gender on Lumbar Spine Sagittal Plane Range of Motion: A Study of 1126 Healthy Subjects. Spine. 1994;19:682-686.

31. Van Donkelaar C, Kretzers L, Bovendeerd P, Lataster LM, Nicolay K, Janssen JD, Drost MR. Diffusion tensor imaging in biomechanical studies of skeletal muscle function. Journal of anatomy. 1999;194:79-88.

32. Van Doom A, Bovendeerd P, Nicolay K, Drost MR, Janssen J. Determination of muscle fibre orientation using diffusion-weighted MRI. Eur. J. Morphol. 1996;34:5-10.

33. Ward SR, Kim CW, Eng CM, Gottschalk LJ 4th, Tomiya A, Garfin SR, Warrd SR. Architectural analysis and intraoperative measurements demonstrate the unique design of the multifidus muscle for lumbar spine stability. J Bone Joint Surg Am. 2009;91:176-185.

34. Wokke B, Van Den Bergen J, Versluis M, Niks EH, Milles J, Webb AG, van Zwet EW, Aartsma-Rus A, Verschuuren JJ, Kan HE. Quantitative MRI and strength measurements in the assessment of muscle quality in Duchenne muscular dystrophy. Neuromuscular Disorders. 2014;24:409-416.

35. Youdas JW, Hollman JH, Krause DA. The effects of gender, age, and body mass index on standing lumbar curvature in persons without current low back pain. Physiotherapy theory and practice. 2006;22:229-237.

CHAPTER 4: THE RELATIONSHIPS BETWEEN MICROSTRUCTURE AND THE DIFFUSION TENSOR IN SIMULATED SKELETAL MUSCLE

4.1 ABSTRACT

Purpose: To establish a series of relationships defining how muscle microstructure and diffusion tensor imaging (DTI) are related.

Methods: The relationship between key microstructural features of skeletal muscle (fiber size, fibrosis, edema, and permeability) and the diffusion tensor were systematically simulated over physiologically relevant dimensions individually, and in combination, using the numerical simulation application DifSim. Stepwise multiple regression was used to identify which microstructural features of muscle significantly predict the diffusion tensor using single-echo and multi-echo DTI pulse sequences. Simulations were also performed in models with histology informed geometry to investigate the relationship between fiber size and the diffusion tensor in models with real muscle geometry.

Results: Fiber size is the strongest predictor of λ2, λ3, MD, and FA in skeletal muscle, accounting for ~40% of the variance in the diffusion model when calculated with single-echo DTI. This increased to ~70% when diffusion measures were calculated from the short T2 compartment of the multi-echo DTI sequence. This non-linear relationship begins to plateau in fibers with greater than 60μm diameter.

Conclusion: As normal fiber size of a human muscle fiber is 40μm-60μm, this suggests that DTI is a sensitive tool to monitor muscle atrophy, but may be limited in measurements of muscle with larger fibers.

4.2 INTRODUCTION

Skeletal muscle is a highly organized, hierarchical tissue containing long contractile cells bundled to form fascicles, which are again bundled to form the larger whole muscle [1]. These subdivisions of muscle are all packaged in layers of extracellular matrix (ECM). With injury, microstructural (cell-level) changes have been observed, which are related to impaired muscle function [2,3]. Commonly observed changes in muscle microstructure with injury or pathology include fiber atrophy/hypertrophy [4,5], fibrosis [6], membrane damage (permeable fibers) [7-9], and edema [10-12]. The current gold standard for studying injury- or plasticity-associated changes in muscle microstructure is histology, which is highly invasive, is semi-quantitative, and difficult to extrapolate to the entire muscle. Therefore a quantitative, non-invasive technique to study muscle microstructural changes resulting from injury would be a potentially important contribution to the clinical assessment of muscle pathologies.

Diffusion tensor imaging (DTI) is a magnetic resonance imaging (MRI) technique that has been shown to be sensitive to changes in muscle microstructure [13-15]. DTI measures the anisotropic diffusion of water in muscle, which is restricted by microstructure. However, the relationship between microstructure, the actual diffusion changes, and the resultant diffusion tensor (DT) associated with muscle injury or pathology are exceedingly complex and not amenable to simple analysis. Nevertheless,

certain structural and physiological quantities averaged over the voxel volume can nevertheless serve as a proxy for actual structural features and their changes. For example, several groups have shown a less restricted diffusion profile when muscles are contracted, and a more restricted diffusion profile when muscles are elongated [16-20]. As the sarcolemma is thought to be the main barrier to diffusion in muscle, this effect is attributed to changes in muscle fiber diameter that occur when a whole muscle is contracted (fiber diameter increases) or elongated (fiber diameter decreases). However, such a simple explanation is complicated in injured states as less restricted diffusion is also observed when edema is present or structural integrity of the sarcolemma is compromised (increased fiber permeability), regardless of underlying changes in muscle fiber diameter [4,21]. In addition to changes in the permeability of the sarcolemma and size of fibers, diffusion changes have been attributed to increases in T2, and increased signal to noise ratios, secondary to increased extra-cellular fluid volume [22-24]. Non-diffusion, MR-relaxometry experiments can uncover these edema-related fluid shifts involved in maintaining metabolic and volumetric stasis between the intracellular compartments [12,25-27], but lacks the ability to resolve microstructural features of muscle, which directly inform physiology and performance.

Muscle exhibits a multi-exponential T2 decay signal of water, which originates from macromolecular interactions (ultrashort; <10ms), intra-cellular (short T2; ~40ms) and extra-cellular (long T2; 90+ms) compartments of muscle (26-29). The ultrashort T2 compartment is often too short to be measured using spin echo imaging due to requisite echo times and is mostly ignored [10]. In the presence of edema, increased fluid content is observed in the extra-cellular space around cells [11,30]. Due to the changes in cellularity

observed during edema, as the volume fraction of extracellular water increases, whole muscle T2 increases. However, whole muscle T2 can also be traced to intracellular origins [24,31,32]. While simplification of T2 decay into a one-compartment model is adequate for normal muscle, injured or pathologic muscle exhibits multiple microstructural changes, including edema, which renders a single compartment model too simple [10,33]. One approach to addressing this complication is multi-echo DTI, a MR technique that combines basic principles to simultaneously measure T2 and the DT, which allows quantification of diffusion originating from the short (intra-cellular) and long (extra-cellular) compartments of muscle [33]. This technique has the potential to increase the specificity of DTI to be a better tool to measure changes in muscle microstructure.

The complexity of the relationship between muscle microstructure and the diffusion profile in both normal and injured muscle thus requires a systematic investigation if useful clinical metrics are to be derived from the measured diffusion signal. The effect of muscle microstructural changes on the measured DT can be quantified by computer simulation. Several groups have investigated the effect of imaging parameters such as noise, partial volume, and diffusion weighting strength on the DT, to inform guidelines for developing DTI protocols [22,34-36]. However, only two studies have simulated the effect of fiber geometry [37] and edema [38] on the DT. In this paper we utilize the DTI simulation application DifSim, which is capable of modeling an entire DTI experiment with complex tissue geometries.

Therefore, the purpose of this study is to use a novel, sophisticated, *in silico* tool to carefully investigate the relationships between both simplified and histology informed

muscle microstructure and the DT. Specifically, we will quantify the influence of muscle fiber size, fibrosis, membrane permeability, and edema, in isolation and in combination, on the DT using single- and multi-echo DTI techniques. We hypothesize intra- and extra-cellular microstructural changes in injured muscle have characteristic diffusion profiles that can be uncoupled with multi-echo DTI.

4.3 METHODS

4.3.1 Overview of DifSim

DifSim embeds MCell, a Monte Carlo simulator for cellular microphysiology [39], within an MRI simulator which tracks particle location, magnetization amplitude and phase, within a user defined arbitrarily complex geometrical model [40]. DifSim is capable of supporting boundary and particle interactions, and multiple molecular species with different diffusion coefficients.

The basic numerical approach of DifSim is presented here. A more complete treatment can be found in Balls et. al 2009 [40]. Particles (spins) diffusing in time (t) at a position (x(t)) have a spin (j) and will accrue a phase (θ_j) generated by the spin's displacement in the direction of the magnetic field (G(t)) gradient

$$\theta_j(t) = \int_{t_0}^{t} G(\tau) \cdot x_j(\tau) d\tau \qquad \text{Equation 1}$$

where "·" represents the dot product. If time is discretized into N_t time steps of length dt, and measure the magnetic field strength and spin location at each time t_i, equation 1 can be approximated as

$$\theta_j(t) = \sum_{i=0}^{t} G(t_i) \cdot x_j(t_i) dt \qquad \text{Equation 2}$$

The relaxation is introduced for each particle *j* at each time t_i by using particle magnetization vector:

$$\left(m_x^j, m_y^j, m_z^j\right) = \left(m_\rho^j cos\left(\theta_j\right), m_\rho^j sin\left(\theta_j\right), m_z^j\right) \quad \text{Equation 3}$$

as:

$$m_\rho^j = m_\rho^j(0)e^{-t/T_2} \quad \text{Equation 4}$$

$$m_z^j = m_z^j(0)e^{-t/T_1} + \left(1 - e^{-t/T_1}\right) \quad \text{Equation 5}$$

By simultaneously simulating the diffusion of N_p individual spins with MCell, the echo amplitude is

$$E = \frac{e^{-t/T_2}}{N_p}\sum_{j=1}^{N_p} e^{i\gamma\theta_j} \quad \text{Equation 6}$$

where γ is the gyromagnetic ratio.

4.3.2 Simulation DTI pulse sequence parameters

Pulse sequence parameters used in our MRI simulations were based on those used on a 7T MRI scanner at our institution (Bruker, Billerica MA) (41). A diffusion-weighted, multi-echo pulse sequence was used [12]. The first echo was TE=21.76ms, with 16 equally spaced echoes at 10ms intervals, 15 gradient directions, b=500mm^2/s (δ/Δ 2ms/9ms), and voxel size 200x200x200μm^3.

4.3.3 DT calculation

For each voxel, the DT was calculated using single-echo data (Equation 7a) and as two compartments in slow exchange (Equation 7b) from multi-echo data using custom written software in Matlab (Mathworks, Natick MA).

$$S_i(b) = e^{(-bD_i)} + \varepsilon \quad \text{Equation 7a}$$

$$S_i(TE, b) = f_a e^{\left(\frac{-TE}{T_{2,a}}\right)} e^{(-bD_{i,a})} + f_b e^{\left(\frac{-teTE}{T_{2,b}}\right)} e^{(-bD_{i,b})} + \varepsilon \quad \text{Equation 7b}$$

$Where S_i(TE, b)$ is the signal along a certain gradient direction (S_i) at echo time (TE) and b-value (b), f is the volume fraction of the short (a) and long (b) transverse relaxation (T2) compartments of the apparent diffusion coefficient (D_i) along the same gradient direction, such that $f_a + f_b = 1$.

First, a bi-exponential decay function was fit from the b=0 image from each echo using the MERA 2.03 toolbox to find $f_a, f_b, T_{2,a}$, and $T_{2,b}$[33]. A nonlinear least square fit was used to solve $D_{i,a}$ and $D_{i,b}$ using the *fit* function in Matlab. The DT was solved using a nonnegative least-squares fit using the fanDTasia toolbox [42]. Diagonalization of the DT yields the eigenvalues (λ1, λ2, and λ3), which were used to calculate mean diffusivity (MD) and fractional anisotropy (FA) (Equations 8, 9). For single-echo analysis, data from the first recorded echo of the multi-echo DTI sequence was used.

$$MD = \frac{\lambda 1+\lambda 2+\lambda 3}{3} \qquad \text{Equation 8}$$

$$FA = \sqrt{\frac{3}{2}}\sqrt{\frac{(\lambda 1-MD)^2+(\lambda 2-MD)^2+(\lambda 3-MD)^2}{\sqrt{\lambda 1^2+\lambda 2^2+\lambda 3^2}}} \qquad \text{Equation 9}$$

Fractional anisotropy is a normalized scalar measure of how anisotropic the diffusion profile is and varies from 0 (perfectly isotropic) to 1 (perfectly anisotropic). Mean diffusivity is a measure of the average overall diffusion. Mean diffusivity of unrestricted water is $2.5 \times 10^{-3} mm^2/s$. Generally, as the restricted diffusion profile increases (increased FA), there is less overall diffusion (decreased MD) and vice versa.

4.3.4 Simplified Model generation

As a first step, the complex geometry of skeletal muscle was reduced to simple, closely packed hexagons, which has a limited number of defining parameters that allowed us to systematically study the relationship between an idealized muscle

microstructure model and the measured DT. The features of muscle microstructure studied include fiber size, fibrosis, edema, and permeability and are depicted individually in Figure 1. Ideal muscle model geometries were simplified into geometrically symmetric patterns, which approximate but not exactly replicate real muscle microstructure. Fiber size was varied by systematically changing the diameter of the hexagon structures. Fibrosis was modeled by varying the spacing between muscle fibers. Edema was simulated by varying the volume fraction of water in the "extracellular" space. Permeability was varied by randomly defining walls of the fibers as transparent to water molecules to diffuse between the intra- and extra-cellular spaces.

Microstructural features of skeletal muscle were varied individually and in combination over a range of physiologically relevant values (Table 1) to determine their individual contributions to the DT, individually, and in combination with one another. The basic model representative of normal healthy muscle was defined with 50μm fiber diameter, 2μm fiber spacing, 5% extracellular water volume fraction and 0% permeable walls. Individual features of muscle microstructure were investigated based on this model. Models were constructed in Google SketchUp, and triangulated using Blender [43]. Intra- and extra-cellular particles were assigned different diffusion coefficients and magnetic relaxation (T1, T2) rates based on literature values. Relaxation rates and diffusion coefficients of molecular species were taken from the literature; intracellular: T1/T2: 1,740/25ms (44-46), D: $1.8*10^{-3}mm^2/s$ [47-49]; extracellular: T1/T2: 2,500/95ms [46,47], D: $2.2*10^{-3}mm^2/s$ [50,51]. Two hundred thousand particles were simulated in order to accurately converge on an analytical solution based on the diffusion coefficients and b-value chosen for this experiment [39]. Each model was simulated 10 times with a different

initial location of diffusing particles to measure variance in an individual model. No noise was added in order to measure the exact relationship between muscle microstructure and the DT under ideal imaging conditions.

4.3.5 Histology informed geometry models

To evaluate how our results compare to real diffusion measurements of muscle, we created models with geometry derived from previous animal histology experiments. Masson's Trichrome stained histology of muscle fibers from control, cardiotoxin injected, *botulinium toxin* (botox) injected, surgically denervated and surgically tenotomized rat tibias anterior muscles at 1, 3, 7, 14 and 30 days post injury were manually segmented and triangulated in Blender (Fig. 2). Cardiotoxin is venom from the *naja mossambica* snake, and induces depolarization of the sarcolemma that results in a massive, rapid onset muscle degeneration from which muscle can heal in approximately 30 days [52]. Botox is a bacterium-produced neurotoxin that prevents acetylcholine release in motor neurons and results in muscle atrophy [3]. Surgical denervation creates a physical nerve injury that prevents a muscle from contracting, resulting in chronic atrophy [53]. Surgical tenotomy severs the tendon attaching muscle to bone, resulting in acute fiber hypertrophy due to isometric contraction of the muscle, followed by chronic atrophy [54]. Average fiber diameters were recorded for each model. Each histological image was separated into 9 individual diffusion experiments, covering a total area of 600μm x 600μm. Extracellular water volume fractions assigned to each model are defined in Table 2 and are approximated from histologic and MRI studies of these tissues. The same relaxation and diffusion coefficients assigned to the simplified models of muscle were applied to the histology informed models.

4.3.6 Statistics

The relationship between individual features of muscle microstructure and the DT were quantitatively examined. To determine how the interaction between different compartments of muscle microstructure and the DT (FA and MD) are related, a stepwise multiple linear regression model was used.

To demonstrate the difference in the DT measured with single- and multi-echo DTI, a curve was fit to describe the relationship fiber size and the DT for simplified, non-edematous models using the single-echo data. Then, the same fiber size models were simulated with edema (45% extracellular water volume fraction) and the DT calculated with both single- and multi-echo DTI data. The relationship between the single, short, and long DT's and fiber size in edematous muscle were compared to the non-edematous curve. Coefficient of determination (R^2) was calculated to measure the amount of variance explained by the original model and the edematous DT's. Then, the same equations were compared to the single, short, and long DT's in models with histology informed geometry.

The threshold for significance (α) was set to 0.05 for all analyses. Statistics were computed using SPSS 20.0 (IBM, Armonk, NY). All data are reported as mean ± standard deviation.

4.4 RESULTS

4.4.1 Individual relationships between simplified muscle geometry and the measured diffusion tensor

Of the independent features studied, fiber size has the largest dynamic range of the microstructural features examined in this study. Above 60μm diameter, the

relationship between fiber size and the DT appears to reach a plateau (Fig. 3A, D). The single-echo and short compartment of the multi-echo DTI pulse sequences appear to be nearly identical as fiber size, fibrosis, and permeability was varied (Fig. 3A, B, D-F, H). However, as extracellular water volume is increased (muscle becomes more edematous) the single-echo DTI measurements appear to become more similar to the long compartment of the multi-echo DTI measurements (Fig. 3C, G). Interestingly, there is no change in either the short or long compartment diffusion measurements as extracellular water volume fraction is increased.

4.4.2 Predictive capacity of muscle microstructure on the diffusion tensor

Ten replicates of 500 models were input into the stepwise multiple linear regression model to determine which features of microstructure are the best predictors of the DT. As fiber size has a strong non-linear relationship to the DT, it was $\log_e$ transformed for all statistical analysis. Using single-echo DTI, fiber size was the best predictor of MD, λ2, λ3, and FA, explaining 40.7%-44.9% of the variance respectively (Table 3). The next best microstructural predictor of MD, λ2, λ3, and FA was permeability, explaining 29.0% to 35.7% of the variance. Edema and fibrosis together explain 3.1% to 6.4% of variance for MD, λ2, λ3, and FA. Fiber size, permeability, and fibrosis are positively correlated with MD, λ2, and λ3, and negatively correlated with FA. Edema is positively correlated with MD, and FA. Interestingly, edema was a strong predictor of λ1 (R^2=0.98, β=.990), with fibrosis (R^2=0.30 β=-.046) and fiber size (R^2<0.10, β=.018) also significant predictors in the model.

Diffusion in the short T2 compartment calculated with multi-echo DTI was hypothesized to represent intracellular diffusion. Similar to single-echo, fiber size is a

strong predictor of the short compartment of MD, λ2, λ3, and FA, explaining 70.7%-76.2% of the variance in the model (Table 3). Additionally, permeability (R^2: 0.098-0.106) and fibrosis (R^2: 0.001-0.002) were significant predictors of MD, λ2, λ3, and FA. Fiber size, permeability, and fibrosis are positively correlated with MD, λ2, and λ3, and negatively correlated with FA. Permeability (β=-.132), fiber size (β=-.090), and edema (β=.054) were all found to be significant predictors of λ1, however, these microstructural measurements only explain 2.9% of the variance in the model.

Diffusion in the long T2 compartment calculated with multi-echo DTI was hypothesized to represent extracellular diffusion. Permeability was the best predictor of MD, λ2, and FA (R^2: 0.615-0.669), followed by fibrosis (R^2: 0.135-0.177) then fiber size (R^2: 0.044-0.075; Table 3). Permeability and fibrosis are positively correlated with MD and λ2 and negatively correlated with FA. Fiber size is negatively correlated with MD and λ2 and positively correlated with FA. Unexpectedly, fiber size was the strongest predictor of λ3 (R^2=0.756, β=.870), followed by permeability (R^2=0.106, β=.325) and fibrosis (R^2=0.001, β=.037). All four microstructural features tested were significant predictors of λ1, however the total variance explained by the model was relatively low (R^2=0.249) compared to other dependent variables.

4.4.3 Resolution of fiber size measurements using multi-echo DTI

The relationship between fiber size and FA calculated from single-echo DTI for normal (5% extracellular water volume fraction) simplified muscle was fit to an exponential decay equation, which explained 99.5% of the variance in the data (Fig. 4a). When fiber size and FA were simulated under edematous conditions (45% extracellular water volume fraction), the original equation explained none of the variance when FA

was calculated from single-echo DTI data (R^2=-5.68) or from the long T2 compartment using multi-echo DTI analysis (R^2=-76.8), and 97.9% of the variance of FA calculated from the short T2 compartment using multi-echo DTI data. Similarly, the relationship between fiber size and MD calculated from single-echo DTI for normal simplified muscle was fit to a one-phase association equation, which explained 99.6% of the variance in the data (Figure 4b). When fiber size and MD were simulated under edematous conditions, the original equation explained none of the variance when MD was calculated from single-echo DTI data (R^2=-1.55) or from the long T2 compartment using multi-echo DTI analysis (R^2=-35.1), and 98.7% of the variance of FA calculated from the short T2 compartment using multi-echo DTI data.

4.4.4 Histology informed muscle geometry

Models were simulated at all time points except for the cardiotoxin day 1 injury as these muscle fibers had no discernable organized structure. Mean fiber size ranged from 35μm to 76μm in diameter (Fig. 5). In general, botox and denervation models had the smallest fibers that decreased in size with time. Average fiber size of the cardiotoxin model steadily increased over the 30-day time course.

Diffusion measurements in control muscle show little change over the course of 30-days with single-echo DTI (Fig. 6A, D). Large differences in FA were observed between day 3 (FA=.12±.01), day 7 (FA=.22±.05), and day 14 (FA=.14±.03) in the cardiotoxin model when calculated using single-echo DTI, which were not reflective of the measured fiber size changes (Fig. 5, 7A). However, when FA was calculated from the short compartment of the multi-echo DTI analysis, FA appeared to steadily decrease over this time period, which better reflects fiber size changes at these time points (Fig. 6B, 7B). Botox and

denervation models had the highest FA measurements with measured with both single- and multi-echo DTI, especially at later times points when fibers were smaller. In general, MD measurements made with single and the short compartment of multi-echo DTI displayed similar trends, although the short compartment measured MD had higher overall diffusivity measurements, likely due to a higher defined diffusion coefficient. FA and MD measurements calculated from the long compartment of multi-echo DTI demonstrated very high FA and low MD, likely due to the highly restricted diffusion environment of the extracellular space between fibers (Fig. 6C, F).

To compare how well diffusion measurements made in the simplified hexagonal models of muscle are to diffusion measurements made in models with histology informed geometries, we compared the equations fit between fiber size and diffusion measurements (FA and MD) for normal (5% extracellular water volume content) muscle with ideal geometry to histology informed measures of diffusion (Fig. 7). The equation relating fiber size to FA in models with ideal muscle geometry explained none of the variance in FA when calculated with single-echo (R^2=-0.156) or the long compartment of multi-echo DTI (R^2=-10.9). However, this equation described 68.6% of the variance in FA when calculated with the short compartment of multi-echo DTI. The equation relating fiber size to MD in models with ideal muscle geometry described none of the variance in MD when calculated with single-echo (R^2=-3.21), the short compartment (R^2=-9.12), or the long compartment (R^2=-6.50) using multi-echo DTI.

4.5 DISCUSSION AND CONCLUSION

The use of DTI to characterize muscle structure and physiology is an active area or research with important clinical implications informing guidelines for developing DTI protocols specific to skeletal muscle [22,34-36]. However, the complexity of the relationship between muscle health and the measured DT continues to limit DTI's clinical utility.

In this study, we report our initial developments of a program to systematically assess these complex relationships through the use of well defined, albeit simplistic, computational models within a DTI simulation environment. We have evaluated the relationship between four microstructural features of skeletal muscle (fiber size, fibrosis, edema, and permeability) individually, and in combination with one another and the DT in models with both simplified and histology informed geometry. These relationships were simulated using a standard DTI, and a multi-echo DTI pulse sequence, which was able to separate intra- and extra-cellular diffusion based on T2-relaxation of particles in the two compartments. The main finding of this study was fiber size is overall the strongest predictor of $\lambda 2$, $\lambda 3$, MD, and FA in skeletal muscle, accounting for ~40% of the variance in the diffusion model when calculated with single-echo DTI. This increased to ~70% when diffusion measures were calculated from the short T2 compartment from multi-echo DTI, which effectively separates intra- and extra-cellular diffusion. Additionally, the sensitivity of diffusion measurements begins to plateau at fiber sizes greater than 60μm. As the normal fiber size of a human muscle fiber is 40μm-60μm (FA: .180-.135), this suggests that DTI is a sensitive tool to monitor muscle atrophy, but may be limited in measurements of muscle hypertrophy. Comparing diffusion measurements made in models with simplified geometry versus histology informed geometry we found

that fiber size was able to explain 68% of the variance in FA calculated with the short T2 compartment of the multi-echo DTI sequence. This supports that multi-echo DTI may be a useful tool to monitor fiber size changes in the presence of edema.

Healthy skeletal muscle fibers are tightly packed, polygonal structures, surrounded by hierarchical layers of thin ECM. In the simplified models in this study, muscle fibers were approximated as tessellated hexagons, since they can be tightly packed and have a uniform linear spacing. Fibrosis is commonly studied via histology, and is defined as an accumulation of ECM, in both the intrafasicular and perifasicular spaces around muscle fibers, which ultimately interferes with function [2]. ECM is a dynamic structure, composed of a scaffold of connective tissue (e.g. collagen), fluid, and a variety of cells. Functionally in muscle, fibrosis results in increased whole muscle passive stiffness. However, passive mechanical properties are not correlated to the biochemical makeup, or area fraction of the ECM, albeit they normally change in the same direction [2,55]. Fibrosis is a complicated process that resists a precise characterization. For the purposes of the present study, fibrosis was defined as increased spacing of fibers. The restricted diffusion coefficient of water in the ECM was chosen to remain constant as the relative volume fraction of fluid, ECM proteins, cells and cellular debris in the extracellular space is unknown in healthy or fibrotic muscle. Edema in skeletal muscle is a complex, time dependent process, which includes increased fluid transport across capillary beds, which allows for recruitment and migration of inflammatory cells into the damaged region to break down cellular debris [56]. From a DTI perspective, the increased volume fraction of water has the largest effect on both the overall diffusion signal, but the overall T2-relaxation of skeletal muscle. Therefore,

edema was simplified as an increase in the overall extracellular volume fraction of water particles. The concept of permeability in skeletal muscle is often not well defined. Permeability can either be referred to as the passage of water molecules through the sarcolemma of the muscle fibers between the intra and extracellular space, or as a structural defect in the sarcolemma itself. Evans blue dye is commonly used to identify "permeable" fibers in histology, as it is unable to pass through the sarcolemma of an intact fiber [57]. This suggests that the second definition of permeability more accurately describes the focal disruptions thought to occur in the sarcolemma of muscle fibers when injured. Therefore, permeability was simplified as fibers with walls randomly deleted.

In vivo, the presence of increased extra-cellular water due to edema in injured muscle has been shown to strongly affect the diffusion signal, and may dominate other microstructural changes (e.g. fiber atrophy), making detection of microstructure-driven the diffusion signal changes difficult to resolve. This confound can be addressed with the use of multi-echo DTI, which can distinguish intra- and extra-cellular diffusion in muscle by exploiting differences in the transverse relaxation (T2) rate of intra- and extra-cellular water [10,46]. However, this application of multi-echo DTI, while promising, has not been well studied in muscle *in vivo*. To date, single-echo DTI pulse sequences have been the predominant method in muscle DTI studies and have yielded non-specific signal changes, making microstructural changes difficult to quantify in the presence of edema. Though, multi-echo DTI has two major drawbacks. First, the duration of the scan is long (30 minutes -1 hour) since multiple diffusion directions must be sampled at multiple echo times. Second, multi-T2 fitting is a non-trivial technique that is prone to errors, especially when the compartments of the T2 decay are close. However, techniques such as non-

negative least squares estimation and linear programming can be used to reduce the number of T2 compartments into the smallest number of discrete terms to provide an accurate estimation of the data [33]. As this technique is susceptible to noise, care must be taken in order to maximize SNR, particularly at the shortest measured echo times.

Diffusion weighted spin-echo echo planar imaging is sensitive to the T2 relaxation of tissues due to relatively long echo times required for diffusion weighting. Ideally, echo time should be minimized in order to maximize signal-to-noise ratio (SNR). The strategy employed in this study to minimize echo time was to shorten the duration (d) and separation (D) of the diffusion encoding gradients and multi-shot acquisition. However, the drawback to this is the length scale of diffusion being probed over this period (mean square displacement ~5μm^2) is less than the size of a muscle fiber. Other diffusion pulse sequences such as stimulated echo DTI have the potential to sample diffusion at multiple diffusion times at relatively short echo times [58,59], which will certainly provide different insight into the restricted diffusion environment. One of the strengths of DifSim is that this entire experiment can be easily repeated with the same diffusion models but with a different pulse sequence and may be considered for future work.

Fiber size is a key metric in understanding the isometric force generating potential of muscle [60]. In this study, we found that fiber size explains about 70% of the variance in FA when calculated with the short T2 compartment from multi-echo DTI. As FA decreased, fiber size increased and the theoretical force generating capacity of muscle fibers increase. While this finding is not in itself novel, the exponential relationship between fiber size and FA has not been previously shown. Additionally, with the

diffusion sequence tested, a plateau was found for diffusion measurements in muscle fibers greater than 60μm diameter, which is on the upper boundary of normal human skeletal muscle. Clinically, this suggests that DTI is most sensitive to monitoring atrophic disease processes in skeletal muscle.

There are 3 main limitations to this study. First, we did not investigate the effect of SNR on the DT. Future studies of these models will add Gaussian noise to each echo of the diffusion signal to generate SNR ranging from 5 to 140 to compare to previously reported studies. Second, the estimates of extracellular water volume fraction for histology informed geometry models were approximated from previous MR studies of these tissues and were not histologically measured. Third, a relatively small duration of diffusion was measured, which does not allow for all of the water molecules in a cell to be restricted by the sarcolemma. Future studies should include investigating these same models with either different diffusion parameters (i.e. longer diffusion duration) or different DTI pulse sequences (i.e. stimulated echo DTI, HARDI, or multi-shell DTI) in order to get better diffusion contrast.

Using *in silico* modeling to tightly regulate microstructure provides experimental control required to uncouple microstructure from diffusion measurements, which is impossible to perform *in vivo*. This was an initial study, which studied the relationship between microstructure and the DT in highly simplified, and geometrically relevant models of skeletal muscle. This study provides the framework for future studies investigating the dependence of the relationship between the diffusion and muscle microstructure on signal to noise ratio, diffusion pulse sequence parameters, and diffusion pulse sequences. Additionally, a key interpretation of these experiments is a

theoretical framework that can be used to identify features of muscle microstructure DTI may be most sensitive to, and which combinations are beyond the sensitivity of the technique. This tool can be used to inform interpretation of DTI data for clinicians and researchers to non-invasively quantify muscle microstructure to aid in diagnosis, monitor disease progression, and evaluate treatment of muscle pathologies for a wide range of patients.

4.6 ACKNOLEDGEMENTS

L.R.F is supported by grants from the National Institutes of Health (R01MH096100) and National Science Foundation (DBI-1147260, ACI-1550405, ACI-1440412, and AA013419-12). S.R.W. is supported by grants from the National Institutes of Health (HD073180) and Department of Defense (PR120576). The authors would like to thank Keaton Blazer for his help in generating the histology informed computer models.

Chapter 4, in full, is currently being submitted for the publication of the material as it may appear in the Journal of Magnetic Resonance Imaging in Medicine, 2017, Berry DB, Regner BM, Gallinsky V, Ward SR, Frank LF. The dissertation author was the primary investigator and author of this paper.

Table 4-1. Microstructural features and the range over which they were varied individually and in combination of muscle with simplified geometry.

Microstructure	Units	Lower Bound	Upper Bound	Step	
				Individual	Interactions
Fiber Size	μm	10	100	10	20
Fiber Shape	n/a	0.5	1	.1	N/A
Permeability	% transparent fibers	0	60	20	20
Fibrosis	μm	1	10	1	2
Edema	Extra-cellular volume fraction	5	50	5	10

Table 4-2. Extracellular water volume fractions applied to models with histology informed geometry.

	Day 1	Day 3	Day 7	Day 14	Day 30
Control	5	5	5	5	5
Botox	20	15	10	10	10
Denervation	10	10	10	10	10
Tenotomy	10	5	5	5	5
Cardiotoxin	X	45	35	10	5

Table 4-3. Stepwise multiple linear regression results

DTI Analysis	Diffusion Measure	Microstructure	β	Standardized β	R^2
Single Echo	λ1	Constant	1.78E-03		
		Edema	4.64E-06	.990	.980
		Fibrosis	-1.08E-06	-.046	.983
		Fiber Size	1.55E-06	.018	.983
	λ2	Constant	1.59E-04		
		Fiber Size	2.39E-04	.670	.449
		Permeability	5.77E-04	.581	.787
		Fibrosis	1.65E-05	.168	.815
		Edema	1.79E-06	.091	.823
	λ3	Constant	2.02E-04		
		Fiber Size	2.22E-04	.638	.407
		Permeability	5.78E-04	.597	.763
		Fibrosis	1.68E-05	.176	.794
		Edema	1.23E-06	.064	.798
	MD	Constant	7.14E-04		
		Fiber Size	1.54E-04	.646	.417
		Permeability	3.85E-04	.580	.754
		Edema	2.55E-06	.195	.791
		Fibrosis	1.07E-05	.164	.818
	FA	Constant	7.49E-01		
		Fiber Size	-1.14E-01	-.661	.437
		Permeability	-2.59E-01	-.539	.727
		Fibrosis	-7.95E-03	-.168	.755
		Edema	5.89E-04	.062	.759

Table 4-3. Stepwise multiple linear regression results (continued)

DTI Analysis	Diffusion Measure	Microstructure	β	Standardized β	R^2
Multi-Echo (Short)	λ1	Constant	1.77E-03		
		Permeability	-3.16E-06	-.132	.018
		Fiber Size	-7.72E-07	-.090	.026
		Edema	2.52E-08	.054	.029
	λ2	Constant	-2.91E-04		
		Fiber Size	3.99E-04	.873	.762
		Permeability	4.11E-04	.324	.866
		Fibrosis	4.20E-06	.033	.867
	λ3	Constant	-2.82E-04		
		Fiber Size	3.91E-04	.870	.756
		Permeability	4.07E-04	.325	.862
		Fibrosis	4.54E-06	.037	.864
	MD	Constant	3.99E-04		
		Fiber Size	2.63E-04	.871	.758
		Permeability	2.72E-04	.323	.863
		Fibrosis	2.89E-06	.035	.864
	FA	Constant	1.05		
		Fiber Size	-2.10E-01	-.841	.707
		Permeability	-2.17E-01	-.313	.806
		Fibrosis	-2.15E-03	-.031	.807

Table 4-3. Stepwise multiple linear regression results (continued)

DTI Analysis	Diffusion Measure	Microstructure	β	Standardized β	R^2
Multi-Echo (Long)	λ1	Constant	2.11E-03		
		Permeability	2.89E-05	.362	.131
		Fibrosis	-2.26E-06	-.286	.213
		Fiber Size	4.36E-06	.152	.236
		Edema	1.82E-07	.115	.249
	λ2	Constant	1.24E-03		
		Permeability	8.35E-04	.821	.673
		Fibrosis	3.86E-05	.384	.821
		Fiber Size	-7.63E-05	-.209	.865
	λ3	Constant	-2.82E-04		
		Fiber Size	3.91E-04	.870	.756
		Permeability	4.07E-04	.325	.862
		Fibrosis	4.54E-06	.037	.864
	MD	Constant	1.55E-03		
		Permeability	5.66E-04	.818	.669
		Fibrosis	2.52E-05	.368	.805
		Fiber Size	-6.03E-05	-.243	.863
	FA	Constant	3.07E-01		
		Permeability	-3.27E-01	-.784	.615
		Fibrosis	-1.74E-02	-.421	.792
		Fiber Size	4.12E-02	.275	.867

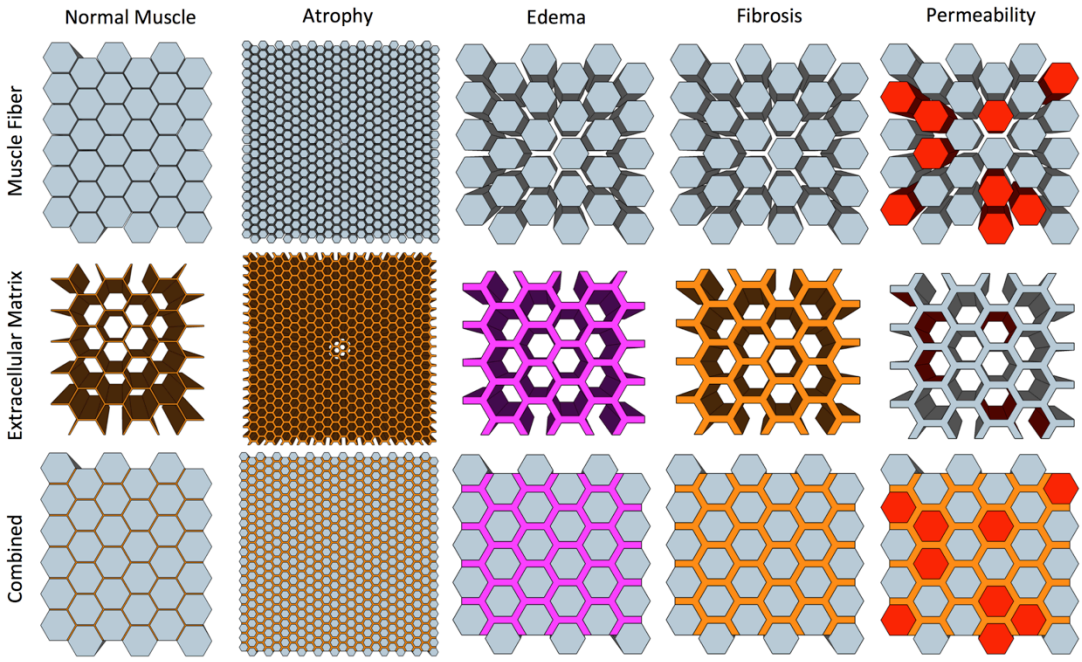

Figure 4-1. Schematic depicting ideally shaped hexagonal models of skeletal muscle (top row; intracellular) and the extracellular matrix (middle row; extracellular). Atrophy/hypertrophy was simulated by changing the diameter of the muscle fibers, edema was simulated by changing the extracellular water volume fraction, fibrosis was simulated by changing the spacing between muscle fibers, and permeability was simulated by allowing free transport between fiber walls into the ECM (red).

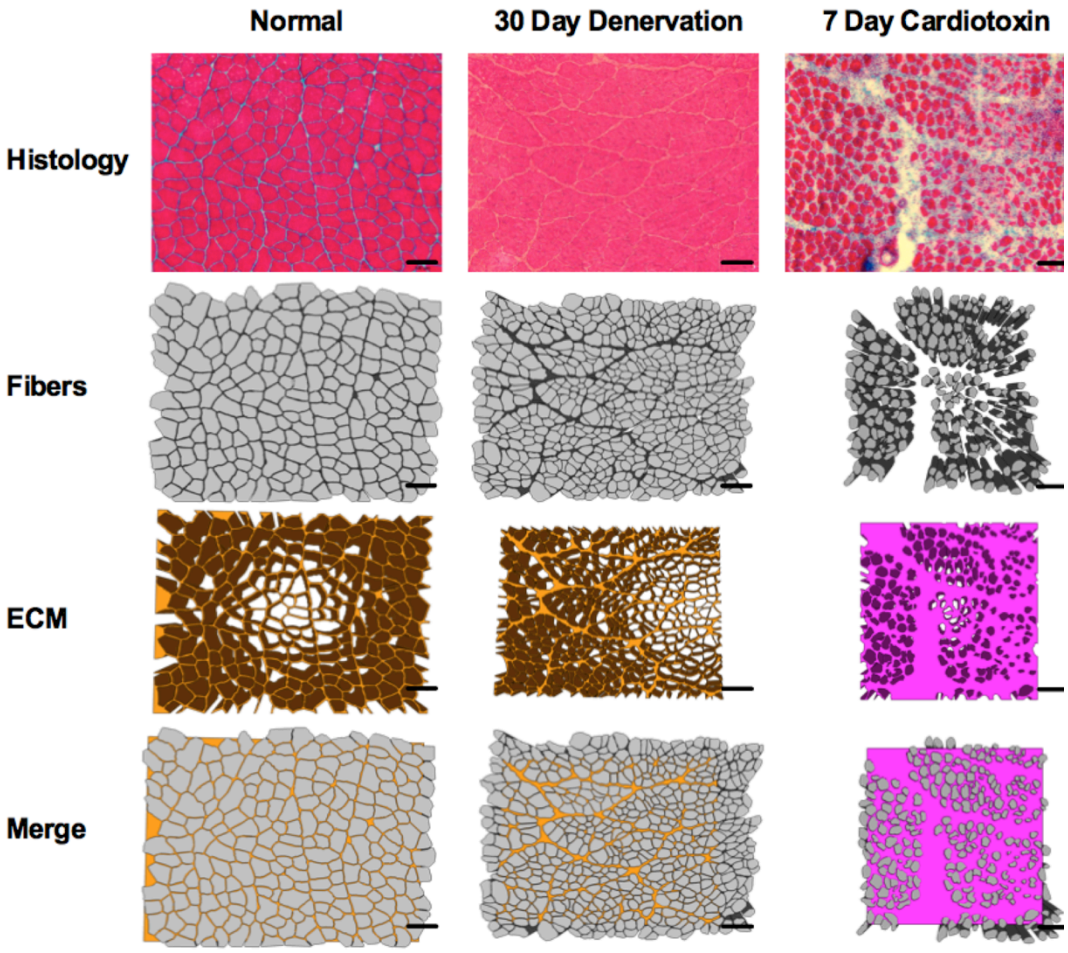

Figure 4-2. Schematic depicting sample histology informed models of skeletal muscle. Fibers were manually traced from histology images.

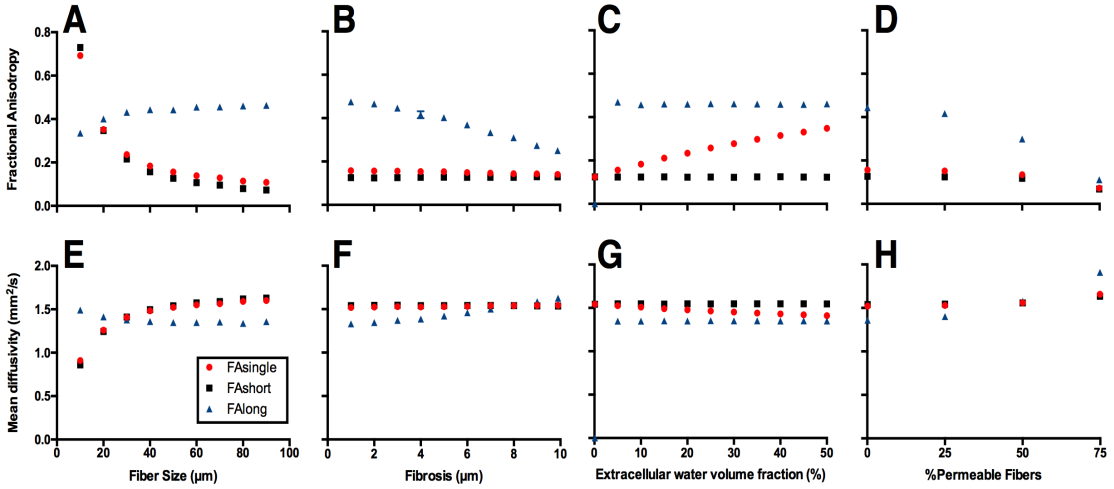

Figure 4-3. Fractional anisotropy (A-D) and mean diffusivity measurements (E-H) measurements of simplified models of skeletal muscle. Diffusion measurements were made from single-echo DTI (red circles) and the short (black squares) and long (blue triangles) T2 compartments from the multi-echo DTI sequence. Fiber size (A, E), fibrosis (B, F), edema (C, G), and permeability (D, H) were varied over a physiologically relevant range of parameters defined in Table 1.

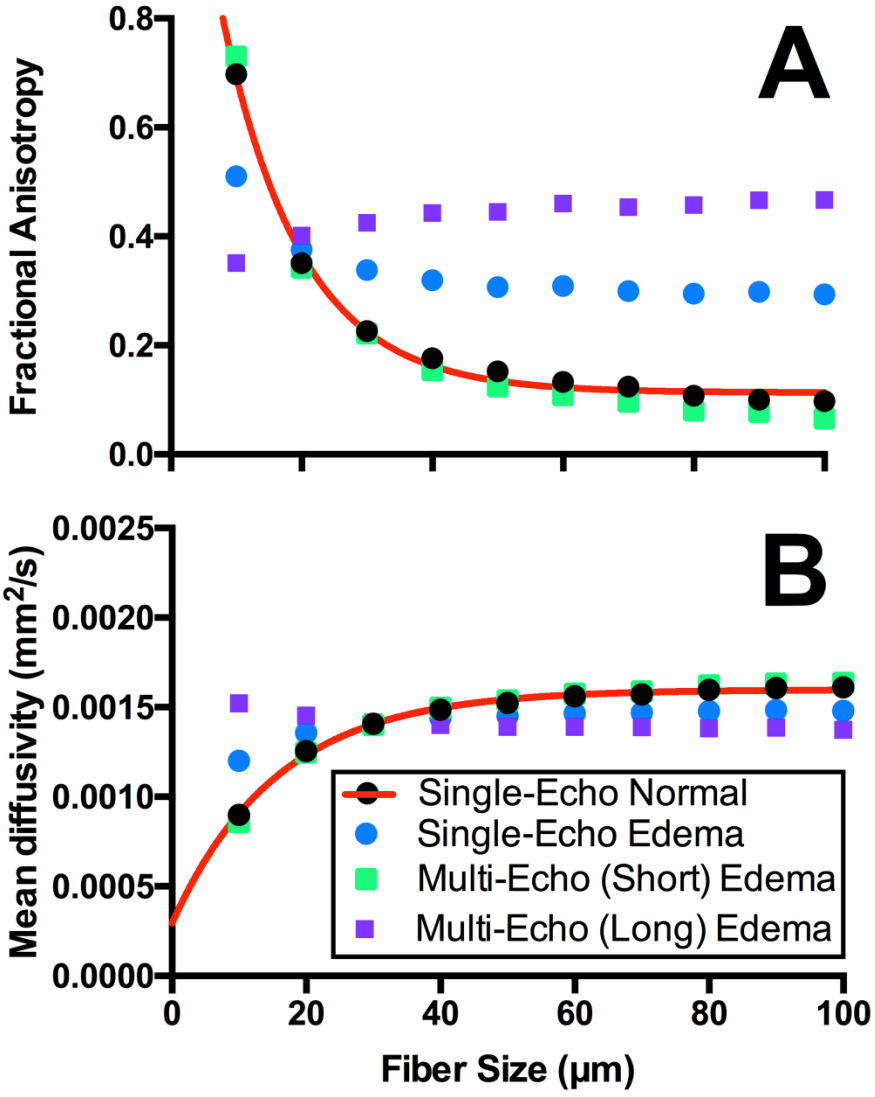

Figure 4-4. Fractional anisotropy (A) and mean diffusivity (B) measurements as a function of fiber diameter measured with single-echo (circles) and multi-echo (squares) DTI for normal (black; 5% extracellular water volume fraction) and edematous (45% extracellular water volume fraction) muscle. Non-linear regression (red line) was fit to the normal muscle diffusion measurements measured with single-echo DTI. The equation for the fractional anisotropy regression is $FA = (1.432 - 0.1134) * e^{-0.082 * fibersize} + 0.1134$. The equation for the mean diffusivity regression is $MD = 2.94 * 10^{-4} \frac{mm^2}{s} + \left(1.30 * 10^{-3} \frac{mm^2}{s}\right) * \left(1 - e^{-.064 * fibersize}\right)$.

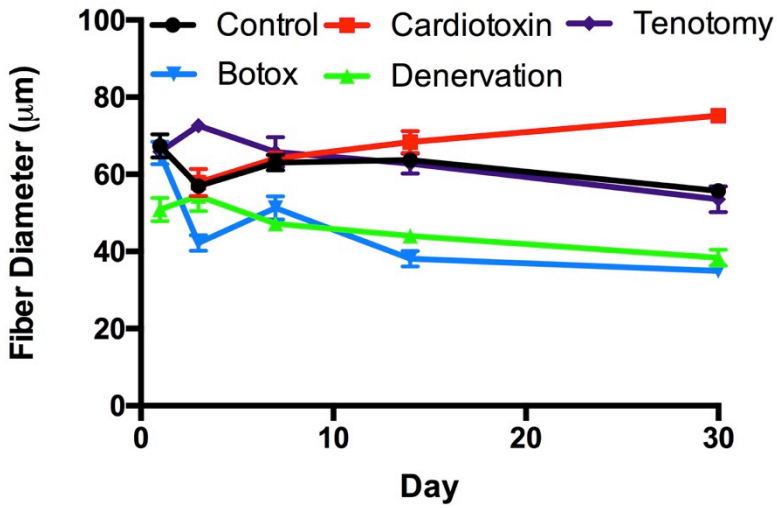

Figure 4-5. Fiber diameter measurements as a function of time for control (black circles), cardiotoxin (red squares), tenotomy (purple diamonds), botox (blue upside down triangles), and denervation (green triangles) models of skeletal muscle. Histology was obtained at day 1, 3, 7, 14, and 30 post-injury from a previous study in our lab.

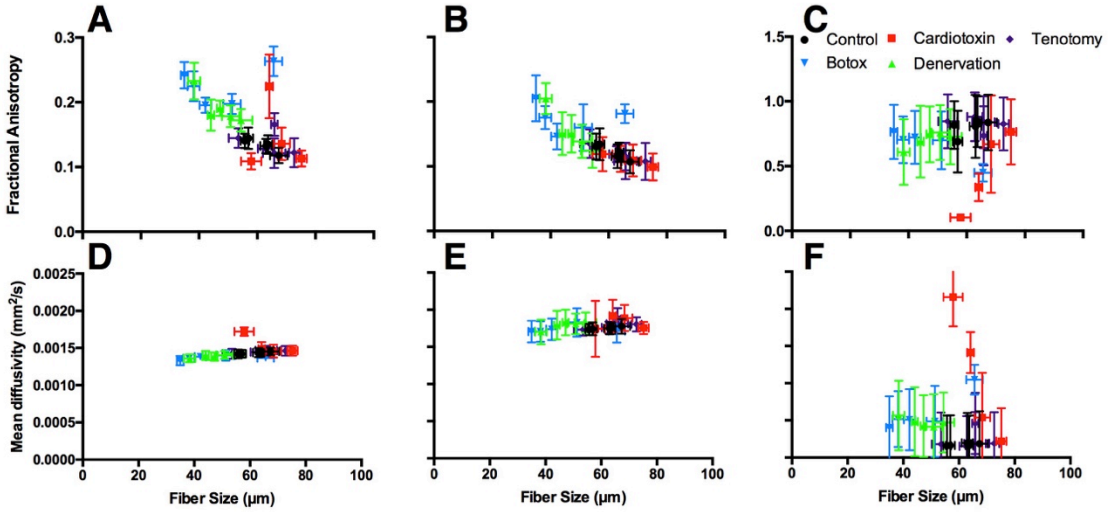

Figure 4-6. Fractional anisotropy (A-C) and mean diffusivity (D-F) measurements of models with histology informed geometry from control (black circles), cardiotoxin (red squares), tenotomy (purple diamonds), botox (blue upside down triangles), and denervation (green triangles) skeletal muscle as a function of mean fiber diameter. Diffusion measures were made with single-echo (A, D), and the short (B, E) and long (C, F) T2 compartments from the multi-echo DTI sequence.

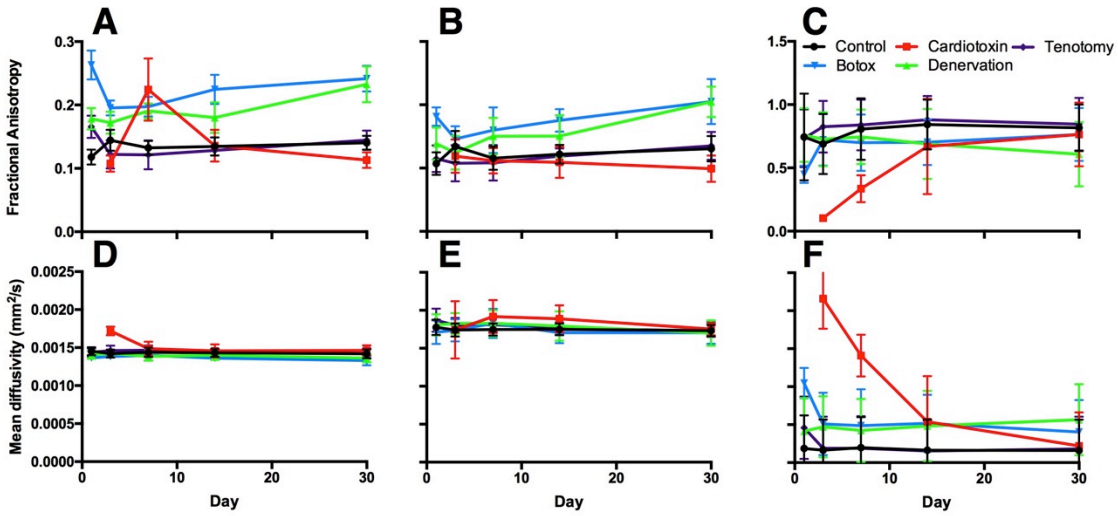

Figure 4-7. Fractional anisotropy (A-C) and mean diffusivity (D-F) measurements of models with histology informed geometry from control (black circles), cardiotoxin (red squares), tenotomy (purple diamonds), botox (blue upside down triangles), and denervation (green triangles) skeletal muscle as a function of days after injury. Diffusion measures were made with single-echo (A, D), and the short (B, E) and long (C, F) T2 compartments from the multi-echo DTI sequence.

4.7 REFERENCES

1. Lieber RL. Skeletal muscle structure, function, and plasticity: Lippincott Williams & Wilkins; 2002.

2. Lieber RL, Ward SR. Cellular mechanisms of tissue fibrosis. 4. Structural and functional consequences of skeletal muscle fibrosis. American Journal of Physiology-Cell Physiology 2013;305(3):C241-C252.

3. Minamoto VB, Suzuki KP, Bremner SN, Lieber RL, Ward SR. Dramatic changes in muscle contractile and structural properties after 2 botulinum toxin injections. Muscle & nerve 2015;52(4):649-657.

4. Esposito A, Campana L, Palmisano A, De Cobelli F, Canu T, Santarella F, Colantoni C, Monno A, Vezzoli M, Pezzetti G. Magnetic resonance imaging at 7T reveals common events in age-related sarcopenia and in the homeostatic response to muscle sterile injury. PloS one 2013;8(3):e59308.

5. Herbison G, Jaweed M, Ditunno J. Muscle fiber atrophy after cast immobilization in the rat. Archives of physical medicine and rehabilitation 1978;59(7):301-305.

6. Silldorff MD, Choo AD, Choi AJ, Lin E, Carr JA, Lieber RL, Lane JG, Ward SR. Effect of supraspinatus tendon injury on supraspinatus and infraspinatus muscle passive tension and associated biochemistry. J Bone Joint Surg Am 2014;96(20):e175.

7. Hamer P, McGeachie J, Davies M, Grounds M. Evans Blue Dye as an in vivo marker of myofibre damage: optimising parameters for detecting initial myofibre membrane permeability. Journal of anatomy 2002;200(1):69-79.

8. Straub V, Rafael JA, Chamberlain JS, Campbell KP. Animal models for muscular dystrophy show different patterns of sarcolemmal disruption. The Journal of cell biology 1997;139(2):375-385.

9. Sigmund EE, Novikov DS, Sui D, Ukpebor O, Baete S, Babb JS, Liu K, Feiweier T, Kwon J, McGorty K. Time-dependent diffusion in skeletal muscle with the random permeable barrier model (RPBM): application to normal controls and chronic exertional compartment syndrome patients. NMR in biomedicine 2014;27(5):519-528.

10. Ababneh Z, Beloeil H, Berde CB, Gambarota G, Maier SE, Mulkern RV. Biexponential parameterization of diffusion and T2 relaxation decay curves in a rat muscle edema model: decay curve components and water compartments. Magnetic resonance in medicine 2005;54(3):524-531.

11. Bryant ND, Li K, Does MD, Barnes S, Gochberg DF, Yankeelov TE, Park JH, Damon BM. Multi-parametric MRI characterization of inflammation in murine skeletal muscle. NMR in biomedicine 2014;27(6):716-725.

12. Fan RH, Does MD. Compartmental relaxation and diffusion tensor imaging measurements in vivo in λ-carrageenan-induced edema in rat skeletal muscle. NMR in biomedicine 2008;21(6):566-573.

13. Heemskerk AM, Drost MR, van Bochove GS, van Oosterhout MF, Nicolay K, Strijkers GJ. DTI-based assessment of ischemia-reperfusion in mouse skeletal muscle. Magnetic resonance in medicine 2006;56(2):272-281.

14. Van Doom A, Bovendeerd P, Nicolay K, Drost M, Janssen J. Determination of muscle fibre orientation using diffusion-weighted MRI. Eur J Morphol 1996;34:5-10.

15. Van Donkelaar C, Kretzers L, Bovendeerd P, Lataster L, Nicolay K, Janssen J, Drost M. Diffusion tensor imaging in biomechanical studies of skeletal muscle function. Journal of anatomy 1999;194(1):79-88.

16. Deux J, Malzy P, Paragios N, Bassez G, Luciani A, Zerbib P, Roudot-Thoraval F, Vignaud A, Kobeiter H, Rahmouni A. Assessment of calf muscle contraction by diffusion tensor imaging. European radiology 2008;18(10):2303-2310.

17. Hatakenaka M, Yabuuchi H, Sunami S, Kamitani T, Takayama Y, Nishikawa K, Honda H. Joint position affects muscle proton diffusion: evaluation with a 3-T MR system. American Journal of Roentgenology 2010;194(2):W208-W211.

18. Schwenzer NF, Steidle G, Martirosian P, Schraml C, Springer F, Claussen CD, Schick F. Diffusion tensor imaging of the human calf muscle: distinct changes in fractional anisotropy and mean diffusion due to passive muscle shortening and stretching. NMR in biomedicine 2009;22(10):1047-1053.

19. Sinha S, Sinha U, Edgerton VR. In vivo diffusion tensor imaging of the human calf muscle. Journal of magnetic resonance imaging : JMRI 2006;24(1):182-190.

20. Sinha U, Sinha S, Hodgson JA, Edgerton RV. Human soleus muscle architecture at different ankle joint angles from magnetic resonance diffusion tensor imaging. Journal of applied physiology 2011;110(3):807-819.

21. Sciorati C, Esposito A, Campana L, Canu T, Monno A, Palmisano A, De Cobelli F, Del Maschio A, Ascheman DP, Manfredi AA. 7-Tesla magnetic resonance imaging precisely and noninvasively reflects inflammation and remodeling of the skeletal muscle in a mouse model of antisynthetase syndrome. BioMed research international 2014;2014.

22. Damon BM. Effects of image noise in muscle diffusion tensor (DT)-MRI assessed using numerical simulations. Magnetic resonance in medicine 2008;60(4):934-944.

23. Froeling M, Nederveen AJ, Nicolay K, Strijkers GJ. DTI of human skeletal muscle: the effects of diffusion encoding parameters, signal-to-noise ratio and T2 on tensor indices and fiber tracts. NMR in biomedicine 2013;26(11):1339-1352.

24. Damon BM, Gregory CD, Hall KL, Stark HJ, Gulani V, Dawson MJ. Intracellular acidification and volume increases explain R2 decreases in exercising muscle. Magnetic resonance in medicine 2002;47(1):14-23.

25. Esposito A, Campana L, Palmisano A, De Cobelli F, Canu T, Santarella F, Colantoni C, Monno A, Vezzoli M, Pezzetti G. Magnetic resonance imaging at 7T reveals common events in age-related sarcopenia and in the homeostatic response to muscle sterile injury. PloS one 2013;8(3).

26. Belton PS, Jackson RR, Packer KJ. Pulsed NMR studies of water in striated muscle: I. Transverse nuclear spin relaxation times and freezing effects. Biochimica et Biophysica Acta (BBA)-General Subjects 1972;286(1):16-25.

27. Cole WC, Leblanc AD, Jhingran SG. The origin of biexponential T2 relaxation in muscle water. Magnetic resonance in medicine 1993;29(1):19-24.

28. Ploutz-Snyder LL, Nyren S, Cooper TG, Potchen EJ, Meyer RA. Different effects of exercise and edema on T2 relaxation in skeletal muscle. Magnetic resonance in medicine 1997;37(5):676-682.

29. Hazlewood CF, Chang DC, Nichols BL, Woessner DE. Nuclear magnetic resonance transverse relaxation times of water protons in skeletal muscle. Biophysical Journal 1974;14(8):583.

30. Nikolaou PK, Macdonald BL, Glisson RR, Seaber AV, Garrett WE. Biomechanical and histological evaluation of muscle after controlled strain injury. The American journal of sports medicine 1987;15(1):9-14.

31. Fung B, Puon P. Nuclear magnetic resonance transverse relaxation in muscle water. Biophysical journal 1981;33(1):27.

32. Belton PS, Packer KJ. Pulsed NMR studies on water in striated muscle III. The effects of water content. Biochimica et Biophysica Acta (BBA)-General Subjects 1974;354(2):305-314.

33. Does MD. Multiexponential Relaxation Analysis. 2014.

34. Pierpaoli C, Basser PJ. Toward a quantitative assessment of diffusion anisotropy. Magnetic resonance in Medicine 1996;36(6):893-906.

35. Anderson AW. Theoretical analysis of the effects of noise on diffusion tensor imaging. Magnetic Resonance in Medicine 2001;46(6):1174-1188.

36. Farrell JA, Landman BA, Jones CK, Smith SA, Prince JL, van Zijl P, Mori S. Effects of signal-to-noise ratio on the accuracy and reproducibility of diffusion tensor imaging–derived fractional anisotropy, mean diffusivity, and principal eigenvector measurements at 1.5 T. Journal of Magnetic Resonance Imaging 2007;26(3):756-767.

37. Karampinos DC, King KF, Sutton BP, Georgiadis JG. Myofiber ellipticity as an explanation for transverse asymmetry of skeletal muscle diffusion MRI in vivo signal. Annals of biomedical engineering 2009;37(12):2532-2546.

38. Damon B. Effect of b-value and TE on the estimation of intramyocellular diffusion properties in the presence of edema. 2009.

39. Stiles JR, Bartol TM. Monte Carlo methods for simulating realistic synaptic microphysiology using MCell. Computational neuroscience: realistic modeling for experimentalists 2001:87-127.

40. Balls GT, Frank LR. A simulation environment for diffusion weighted MR experiments in complex media. Magnetic resonance in medicine 2009;62(3):771-778.

41. Berry DB, You S, Warner J, Frank LR, Chen S, Ward SR. A 3D tissue-printing approach for validation of diffusion tensor imaging in skeletal muscle. Tissue Engineering: Part A 2017.

42. Barmpoutis A, Vemuri BC. A unified framework for estimating diffusion tensors of any order with symmetric positive-definite constraints. 2010. IEEE. p 1385-1388.

43. Kent BR. 3D Scientific Visualization with Blender: Morgan & Claypool; 2015.

44. Crémillieux Y, Ding S, Dunn JF. High-resolution in vivo measurements of transverse relaxation times in rats at 7 Tesla. Magnetic resonance in medicine 1998;39(2):285-290.

45. Diakova G, Korb JP, Bryant RG. The magnetic field dependence of water T1 in tissues. Magnetic resonance in medicine 2012;68(1):272-277.

46. Fan RH, Does MD. Compartmental Relaxation and DTI Measurements In Vivo in λ-Carrageenan Induced Edema in Rat Skeletal Muscle. NMR in Biomedicine 2008;21(6):566.

47. Gefen A, Cornelissen LH, Gawlitta D, Bader DL, Oomens CW. The free diffusion of macromolecules in tissue-engineered skeletal muscle subjected to large compression strains. Journal of biomechanics 2008;41(4):845-853.

48. Moll W. The diffusion coefficient of myoglobin in muscle homogenate. Pflüger's Archiv für die gesamte Physiologie des Menschen und der Tiere 1968;299(3):247-251.

49. Papadopoulos S, Jürgens KD, Gros G. Protein diffusion in living skeletal muscle fibers: dependence on protein size, fiber type, and contraction. Biophysical Journal 2000;79(4):2084-2094.

50. Gilbert DL, Okano T, Miyata T, Kim SW. Macromolecular diffusion through collagen membranes. International journal of pharmaceutics 1988;47(1):79-88.

51. Ramanujan S, Pluen A, McKee TD, Brown EB, Boucher Y, Jain RK. Diffusion and convection in collagen gels: implications for transport in the tumor interstitium. Biophysical journal 2002;83(3):1650-1660.

52. d'ALBIS A, COUTEAUX R, JANMOT C, ROULET A, MIRA JC. Regeneration after cardiotoxin injury of innervated and denervated slow and fast muscles of mammals. European Journal of Biochemistry 1988;174(1):103-110.

53. Kobayashi J, Mackinnon SE, Watanabe O, Ball DJ, Ming Gu X, Hunter DA, Kuzon WM. The effect of duration of muscle denervation on functional recovery in the rat model. Muscle & nerve 1997;20(7):858-866.

54. Jozsa L, Kannus P, Thoring J, Reffy A, Jarvinen M, Kvist M. The effect of tenotomy and immobilisation on intramuscular connective tissue. A morphometric and microscopic study in rat calf muscles. Bone & Joint Journal 1990;72(2):293-297.

55. Smith LR, Lee KS, Ward SR, Chambers HG, Lieber RL. Hamstring contractures in children with spastic cerebral palsy result from a stiffer extracellular matrix and increased in vivo sarcomere length. The Journal of physiology 2011;589(10):2625-2639.

56. Armstrong R, Warren G, Warren J. Mechanisms of exercise-induced muscle fibre injury. Sports Medicine 1991;12(3):184-207.

57. Guo J, Zhang G. Effect of BMI and WHR on lumbar lordosis and sacrum slant angle in middle and elderly women. China journal of orthopaedics and traumatology 2008;21(1):30-31.

58. Tanner JE. Use of the stimulated echo in NMR diffusion studies. The Journal of Chemical Physics 1970;52(5):2523-2526.

59. Merboldt KD, Hänicke W, Frahm J. Diffusion imaging using stimulated echoes. Magnetic resonance in medicine 1991;19(2):233-239.

60. Minamoto VB, Hulst JB, Lim M, Peace WJ, Bremner SN, Ward SR, Lieber RL. Increased efficacy and decreased systemic-effects of botulinum toxin A injection after active or passive muscle manipulation. Developmental Medicine & Child Neurology 2007;49(12):907-914.

CHAPTER 5: A 3D TISSUE PRINTING APPROACH FOR VALIDATION OF DIFFUSION TENSOR IMAGING IN SKELETAL MUSCLE

5.1 ABSTRACT

The ability to non-invasively assess skeletal muscle microstructure, which predicts function and disease, would be of significant clinical value. One method that holds this promise is diffusion tensor MRI (DT-MRI), which is sensitive to the microscopic diffusion of water within tissues and has become ubiquitous in neuroimaging as a way of assessing neuronal structure and damage. However, its application to the assessment of changes in muscle microstructure associated with injury, pathology, or age remain poorly defined, because it is difficult to precisely control muscle microstructural features *in vivo*. However, recent advances in additive manufacturing technologies allow precision-engineered diffusion phantoms with histology informed skeletal muscle geometry to be manufactured. Therefore, the goal of this study was to develop skeletal muscle phantoms at relevant size scales in order to relate microstructural features to MRI-based diffusion measurements. A digital light projection based rapid 3D printing method was used to fabricate polyethylene glycol diacrylate based diffusion phantoms with; 1) idealized muscle geometry (no geometry; fiber sizes of 30μm, 50μm or 70μm; or fiber size of 50μm with 40% of walls randomly deleted) or 2) histology-based geometry (normal and after 30-days of denervation) containing 20% or 50% phosphate-buffered saline (PBS). Mean absolute percent error (8%) of the printed phantoms indicated high

conformity to templates when "fibers" were greater than 50μm. A multiple spin-echo EPI diffusion sequence capable of acquiring diffusion weighted data at several echo times, was used in an attempt to combine relaxometry and diffusion techniques with the goal of separating intracellular and extracellular diffusion signals. When fiber size increased (30μm to 70μm) in the 20% PBS phantom, fractional anisotropy (FA) decreased (0.32-0.26) and mean diffusivity increased ($0.44x10^{-3}$ mm^2/s-$0.70x10^{-3}$ mm^2/s). Similarly, when fiber size increased from 30 μm to 70 μm in the 50% PBS diffusion phantoms, a small change in FA was observed (0.18-0.22), but mean diffusivity increased from $0.86x10^{-3}$ mm^2/s-$1.79x10^{-3}$ mm^2/s). This study demonstrates a novel application of tissue engineering to understand complex diffusion signals in skeletal muscle. Through this work, we have also demonstrated the feasibility of 3D printing for skeletal muscle with relevant matrix geometries and physiologically relevant tissue characteristics.

5.2 INTRODUCTION

Skeletal muscle is a hierarchical tissue containing long contractile cells, bundled in extra-cellular matrix to form larger fascicles, which are then bundled to form whole muscle[1]. The microstructure of muscle is closely related to its performance capacity. For example, larger muscle fibers can produce greater contractile forces and elevated extra-cellular matrix concentrations (fibrosis) results in increased passive stiffness[2-4]. With injury and disease, changes in muscle microstructure directly effect a muscle's performance capacity, so muscle biopsy and histopathological examination is the gold standard tool for diagnosis. However, biopsy/histology is highly invasive and often semi-

quantitative, so it is not conducive to longitudinal assessment of muscle health and recovery.

Diffusion tensor magnetic resonance imaging (DT-MRI) is a method that has been used to non-invasively measure the anisotropic, restricted diffusion of water in tissue, which is related to its underlying microstructure[5-7]. For example, muscle cells are long columnar structures with a surrounding membrane (sarcolemma), which is believed to be the primary barrier to water diffusion[8, 9]. Because of this geometry, diffusion is more restricted perpendicular to the membrane than along the longitudinal axis of the cell, yielding anisotropic diffusion in muscle. Thus the geometric anisotropy in the structure of the muscle tissue is expected to result in a measured anisotropy in the directional dependence of the diffusion signal. Fractional anisotropy (FA) is a key variable in DT-MRI and is believed to be most sensitive to changes in fiber size (larger fiber diameters = smaller anisotropy (FA)). However, the relationship between the DT-MRI signals and the tissue microstructure and physiology is exceedingly complex. Thus, while DT-MRI parameters have been shown to be sensitive to skeletal muscle changes associated with injury, age, and chronic pathology,[7] these studies are non-specific, and therefore of limited clinical value. Microstructural and microfluidic changes associated with these conditions include fiber atrophy, fibrosis, edema and increased sarcolemma permeability, all of which theoretically change diffusion of water in muscle[7, 10-13].

In vivo, the presence of increased extra-cellular water due to edema/inflammation in injured muscle has been shown to strongly effect, and may dominate, the diffusion signal, even when concurrent microstructural changes have an opposing diffusion profile[10, 12, 14, 15]. Increased extra-cellular water content is normally observed on MRI as

an increase in the T_2 relaxation value of the tissue. Multi-echo DT-MRI techniques have been implemented to compartmentalize diffusion from intra- and extra-cellular water by combining traditional DT-MRI and T_2-relaxometry techniques[16, 17]. This technique leverages the difference in T_2-relaxation of water in the intra- and extra-cellular space, theoretically limiting the parameter estimate errors found in traditional single-compartment (single-echo) diffusion techniques. However, uncoupling local inflammation/edema from the underlying microstructural changes in muscle is nearly impossible *in vivo* because multiple biological processes occur in parallel.

Non-physiologically relevant anisotropic diffusion phantoms have been developed for DTI reliability studies and to validate complex data analysis techniques[18-21]. However, no diffusion phantoms have been designed to systematically evaluate how muscle microstructure is related to the underlying diffusion profile. Recent developments in additive manufacturing technologies have enabled the construction of complex, precision-engineered, 3D biomimetic scaffolds[22]. These methods include two-photon laser direct writing[23], inkjet 3D printing[24], extrusion based 3D printing[25], and digital light projection (DLP) based 3D printing[26, 27]. Two-photon laser direct writing can achieve 100 nm resolution, yet this process would take days to fabricate a millimeter-size structure due to its point-by-point writing process. Both inkjet 3D printing and extrusion based 3D printing have a coarse spatial resolution, typically over 50μm, rendering them impractical for fabricating skeletal muscle geometry, which is often smaller. DLP-based 3D printing, which is a mask-free, projection-style stereolithography technique, has the advantages of both high speed and high resolution: it takes seconds to photopolymerize a millimeter-size structure, and it has a micron scale resolution. Furthermore, unlike inkjet and

extrusion based methods which give rise to interfaces between droplets or lines, DLP-based 3D projection printing yields smooth surfaces for superior structural integrity due to scanningless printing in the x-y plane and continuous polymerization in the z-direction. This technique has recently developed to fabricate various functional materials and devices [28-30], and tissue engineering scaffolds [31-33]. Therefore, DLP-based 3D printing is an attractive technique to fabricate anisotropic phantoms with skeletal muscle geometry for DT-MRI.

The focus of this study is to employ new 3D printing strategies to develop a novel set of precision-engineered phantoms for characterizing the interrelationship between microstructural variables and MR-diffusion parameters in skeletal muscle. We hypothesize that physiologically relevant changes in muscle microstructure and microfluidics are separable and can be specifically identified using a novel application of multi-echo DT-MRI experiments.

5.3 METHODS

5.3.1 DLP-based 3D printing

A DLP-based 3D printing system was used to fabricate all phantoms (Fig. 1) [26]. Briefly, a collimated UV beam centered at 365nm wavelength illuminates the digital micromirror device (DMD), which contains an array of 2 million micromirrors, and is reflected toward the prepolymer solution. Digital masks are continuously loaded to the DMD chip to control the on/off state of each single micromirror. The projection optics images the patterned UV light onto the prepolymer solution and polymerizes it as the pattern defined by the digital mask. By changing the digital masks and moving the stage

in z direction simultaneously, a 3D structure can be printed within a few seconds. In the current setup, the overall size of the printed structure can be up to 4mm × 6mm in base area with a lateral resolution of 4μm, and several millimeters in height.

The prepolymer solution is a liquid state mixture of monomer or short-chain polymers, photoinitiators, and other additives. There are a large variety of photopolymerizable material that can be used for this DLP 3D printing system, such as polyethylene glycol diacrylate (PEGDA), poly-(methyl methacrylate) (PMMA), poly(acrylic acid) (PAA), poly(lactic acid) (PLA), and dipentaerythritol pentaacrylate (DPPA)[30, 31, 34, 35]. Common photoinitiators includes Irgacure 2959, Irgacure 651, Irgacure 819, 2-dimethoxy-2-phenylaceto-phenone (DMPA), and lithium phenyl-2,4,6-trimethylbenzoylphosphinate (LAP)[27].

Upon stimulation by UV light, the photoinitiator generates free radicals locally. Then the free radicals attack the C=C bonds and generates acrylic monomers with free electrons, which react with the monomers and crosslink them into polymer networks. This cures the places exposed to UV light. After exposure, the remaining liquid prepolymer is rinsed with phosphate-buffered saline (PBS), and a solid structure remains.

PEGDA (Sigma-Aldrich) was the main building material and LAP was the photoinitiator chosen for the phantoms, as they can be combined with water to form hydrogel structures, ranging from 0% to 80% water content. The prepolymer solution is prepared as follows: The 50%PEGDA/50%PBS prepolymer solution contains 50% (V/V) PEGDA (700 Da), 50% (V/V) PBS (Life Technologies), 0.25% (w/V) LAP, and 0.001% (w/V) Tempo (Sigma-Aldrich) as a free radical quencher. The 80%PEGDA/20%PBS

prepolymer solution contains 80% (V/V) PEGDA (700 Da), 20% (V/V) PBS, 0.25% (w/V) LAP, and 0.001% (w/V) Tempo .

5.3.2 Model Overview

As a first step, the complex geometry of skeletal muscle was reduced to simple, closely packed hexagons in order to systematically study the relationship between muscle microstructure and MR-diffusion. Skeletal muscle structure was simplified into a two compartment model: the intracellular space (the hexagons containing PBS only) and the sarcolemma + extracellular space (3D printed material; Fig. 1). Phantoms were printed in a 30μm, 50μm, or 70μm diameter hexagon array to approximate atrophic, normal, and hypertrophic human skeletal muscle respectively (Fig. 2). The effective extracellular spacing between fibers was 20μm. To replicate skeletal muscle permeability, additional phantoms were printed in a 50μm diameter hexagon array, with 40% of the fiber walls randomly deleted (Fig. 2). Solid phantoms with no geometry were also printed to assess the restricted diffusion profile of water within the extracellular material itself (Fig. 2). Additionally, to model increased extracellular water volume fraction associated with edema, the concentration of water in the 3D printed hydrogel was printed with 20% or 50% PBS. To demonstrate the ability to 3D print geometrically complex phantoms, separate models were printed with histology informed geometry from normal rat muscle (tibias anterior) and an atrophic rat muscle (30-day denervated tibias anterior muscle) (Fig. 3). Denervated skeletal muscle has smaller muscle fibers with increased fibrotic tissue deposition between fibers and is a common model of muscle atrophy[13]. In these phantoms, histology images were imported into Blender (Stichting Blender Foundation, Amsterdam, Netherlands), the contours of the muscle fibers were manually segmented,

and exported as a STereoLithography format (.stl) file . The outer dimensions of the phantoms were 3.8mm wide and 1mm tall.

5.3.3 Model Validation

For each phantom, cross sectional area of 20 "fibers" were randomly measured using ImageJ (NIH, Bethesda, MD). The mean absolute percent error was calculated between measured and expected "fiber" cross sectional area of each set of phantoms in order to assess how similar the printed phantoms were to the original template.

5.3.4 MRI Scanning

Phantoms were printed using the DLP-based 3D printing technique described above. After printing, phantoms were thoroughly rinsed with PBS to remove any remaining prepolymer solution, loaded in 4.3mm diameter tubes, filled with PBS, and carefully capped to ensure no air bubbles were present. Five phantoms of each model were scanned at once. MR experiments were carried out using a 7T Bruker small animal imaging system (BioSpec 70/30, Bruker, Billerica MA) with a 6cm high performance gradient insert capable of producing a maximum gradient amplitude of 1000mT/m, maximum slew rate of 11250T/m/s and a 300W quadrature transmit-receive volume coil. High-resolution structural scans of the samples were acquired using a 3D gradient recalled echo (FLASH) scan with the following parameters: echo time TE:7.3ms, repetition time TR:15ms, acquisition matrix: 450x450x66, voxel size:67x67x100μm^3, number of averages nex=4, bandwidth:50kHz, total acquistion time: 42:30. Then, samples underwent a series of diffusion weighted scans using a multi-shot spin-echo EPI sequence with the following parameters: b=500s/mm^2, 15 diffusion encoding directions, diffusion gradient pulse width δ=2ms, diffusion gradient separation Δ=9ms, number of k-space segments=4, 19 echo times at 10ms interval (22.9ms-202.9ms), and additional

echoes at 252.9ms, and 302.9ms, repetition time TR:5s, matrix size:100x100, in-plane resolution: 300x300 μm^2, slice thickness: 400μm, number of slices: 10, bandwidth 200kHz, total acquisition time: 1:52:00.

5.3.5 MRI Analysis

Registered FLASH images were used to place regions of interest on each of the diffusion phantoms. For each voxel, the diffusion tensor was calculated using single-echo data (Equation 1) or as two compartments in slow exchange (Equation 2) from multi-echo data using custom written software in Matlab (Mathworks, Natick MA).

$$S_i(b) = e^{(-bD_i)} + \varepsilon \qquad \text{Equation 1}$$

$$S_i(TE, b) = f_a e^{(-\frac{TE}{T_{2,a}})} e^{(-bD_{i,a})} + f_b e^{(-\frac{teTE}{T_{2,b}})} e^{(-bD_{i,b})} + \varepsilon \qquad \text{Equation 2}$$

Where $S_i(TE, b)$ is the signal along a certain gradient direction (S_i) at echo time (TE) and b-value (b), f is the volume fraction of the short (a) and long (b) transverse relaxation (T_2) compartments of the apparent diffusion coefficient (D_i) along the same gradient direction, such that $f_a + f_b = 1$.

The MERA 2.03 toolbox was used to determine the number of T_2 components present in a voxel from each of the 16 sets of echo magnitudes[36]. If only a single T_2 component was present, the voxel was processed using single echo data. If two T_2 components were found, the voxel was processed as two compartments in slow exchange, in which case, the MERA toolbox was used to solve for $f_a, f_b, T_{2,a}$, and $T_{2,b}$. A nonlinear least square fit was used to solve $D_{i,a}$ and $D_{i,b}$ using the *fit* function in Matlab. The diffusion tensor was solved for using AFNI[37, 38]. Diagnolization of the diffusion tensor yields the eigenvalues ($\lambda_1, \lambda_2, \lambda_3$), which were used to calculate mean diffusivity (MD)

and fractional anisotropy (FA) (Equations 3, 4). For single-echo analysis, data from the first recorded echo of the multi-echo DTI sequence was used.

$$MD = \frac{\lambda 1+\lambda 2+\lambda 3}{3} \quad \text{Equation 3}$$

$$FA = \sqrt{\frac{3}{2}}\sqrt{\frac{(\lambda 1-MD)^2+(\lambda 2-MD)^2+(\lambda 3-MD)^2}{\sqrt{\lambda 1^2+\lambda 2^2+\lambda 3^2}}} \quad \text{Equation 4}$$

Fractional anisotropy is a normalized scalar measure of how anisotropic the diffusion profile is and varies from 0 (perfectly isotropic) to 1 (perfectly anisotropic). Mean diffusivity is a measure of the average overall diffusion. Mean diffusivity of unrestricted water is $2.5x10^{-3}mm^2/s$. Generally, as the restricted diffusion profile increases (increased FA), there is less overall diffusion (decreased MD) and vice versa.

5.4 RESULTS

5.4.1 3D Printed Phantoms

We used 50%PEGDA/50%PBS and 80%PEGDA/20%PBS prepolymer solutions to successfully fabricate the five geometric designs (30μm hexagons, 50μm hexagons, and 70μm hexagons 50μm hexagon phantoms with 40% of walls randomly deleted, and phantoms with no geometry) and the two histology informed designs (control and 30-day denervation). Qualitatively, the five printed designs mimicked the input designs well based on microscopic image examination (Figs. 2 and 3). Quantitatively, mean percent error of the phantoms was largest (22.2%) for the 30μm phantoms and 7%-8% for all other phantoms. These microscopic images demonstrate the use of DLP-based 3D printing technology to fabricate phantoms of muscle tissue that reproduce the features of each muscle fiber.

5.4.2 MRI

Structural MRI images (3D FLASH) were of sufficient resolution to identify phantom structure (Fig. 4A). The non-diffusion weighted EPI image (b=0) demonstrated signal-to-noise (SNR) ratios (average 33.7 a.u.) above the minimum threshold for accurately calculating the diffusion tensor in skeletal muscle (Fig. 4B)[39, 40]. In general, the diffusion phantom with 50% PBS had effectively the same T_2 value as the phantoms with 20% PBS (Fig. 5A). However, the diffusion characteristics of the materials themselves had opposing diffusion characteristics; the diffusion phantom with 50% PBS had a lower FA and a higher MD than the phantoms with 20% PBS. Fractional anisotropy decreased as the diameter of the hexagons increased for both phantoms (Fig. 5B). However a FA of the 20% PBS phantoms was routinely higher than the 50% PBS phantoms, similar to the phantoms with no geometry. Interestingly, mean diffusivity nearly doubled as fiber size increased for the 50% PBS phantoms, but only a slight difference was observed between 50μm and 70μm diameter hexagons in the 20% PBS phantoms (Fig. 5C). When 50μm diameter hexagon models were printed with 40% of the walls deleted, decreased FA and slightly increased MD was observed only in the 20% PBS model. No decrease in MD was observed when 40% of walls were deleted for the 50% PBS model, which was unexpected. When comparing the histology informed muscle geometry models (normal and denervated), an increase in fractional anisotropy (Fig. 5B) and a decrease in mean diffusivity (Fig. 5C) was observed in the denervation-based sample, which is consistent with previous findings from the literature. The multi-echo DTI sequence was unable to define intra- and extra-cellular T_2 decay signals,

indicating that the 20% and 50% PBS phantoms did not yield complex T_2 signals that would theoretically obscure underlying microstructural changes.

5.5 DISCUSSION

This study demonstrated a technique to fabricate phantoms with physiologically relevant geometries. These phantoms were then used to explore the validity of DT-MRI as a method to measure microstructural changes in skeletal muscle. The FA and T_2 relaxation values of the phantoms were similar to what has previously been found in normal and edematous muscle, while MD was slightly below what has been previously reported (FA: 0.30±0.08; MD: $1.52\pm0.20*10^{-3}mm^2/s$; T_2: 28ms-96ms)[7, 17, 41]. Our results demonstrate that as fiber size decreased, a increase in the fractional anisotropy and a decrease in mean diffusivity was measurable, which is consistent with *in vivo* findings[13]. Similarly, the differences in measured diffusion parameters between phantoms generated from normal and denervated muscle geometries is consistent with expected results from the literature and further supports the idea that DLP based 3D printing can be used to fabricate realistic skeletal muscle phantoms or constructs. However, although differences in T_2 relaxation and diffusion properties were found for the phantoms containing different concentrations of intra- and extracellular PBS, we were unable to identify differences in the regional diffusion of water.

The main goal in phantom design was to mimic the spectrum of structural and biophysical states possible in skeletal muscle. The relative distribution of intra- and extracellular water in real skeletal muscle is currently unknown. Due to histological limitations, the best method to measure water distribution in skeletal muscle is with MRI.

However, measuring extracellular water volume fraction is extremely difficult when no edema is present. The best studies estimate extracellular water volume fraction to be around 5%-20% in healthy muscle, to 45% in edematous muscle. However these numbers have not been validated.

80%/20% PEGDA/PBS was experimentally shown to be the phantom with the lowest overall volume fraction of PBS that resulted in adequate SNR (25), and exhibited a short T_2 relaxation time in the regions where geometry was printed. The 50%/50% PEG/PBS models were deemed the largest volume fraction of water while still accurately being able to print accurate phantom geometries. As the overall volume fraction of PBS increases, there is a corresponding decrease in the structural stability of the models. Therefore, the different volume fractions of PBS and PEGDA were designed in order to replicate the minimum and the maximum extracellular water contents feasible to print with this method to simulate normal and edematous muscle respectively.

In edematous skeletal muscle, increased MD and decreased FA is observed, regardless of other underlying fiber atrophy[11]. In the phantom with the larger fraction of water in the phantom material itself, this same pattern was similarly detected. These findings support the idea that in edematous skeletal muscle, the contribution of extracellular water may be dominating the overall diffusion signal. In real tissue, intra- and extra-cellular diffusion has been separated based on differences in T_2 relaxation between the two compartments using a multi-echo DTI sequence[16, 17]. In our study, we attempted to replicate these findings using a similar sequence but were unsuccessful.

The different diameter sizes chosen for these models were designed to mimic a range of fiber sizes typically found in human muscles. Depending on the species,

function, fiber type, age, and injury, muscle fiber diameters can range from 20μm (mouse/human atrophic muscle) - 100μm (normal frog/ human hypertrophic muscle)[1]. Average muscle fiber diameter is approximately 40μm – 60μm, therefore 50μm diameter was chosen to be the average fiber diameter size. The atrophic (30μm) and hypertrophic (70μm) were chosen to be out of the average range of a muscle fiber, but still in a relevant fiber diameter range of skeletal muscle.

The structural features responsible for permeability in skeletal muscle are currently not well understood. Moreover, the actual definition of the term "permeability" has been used inconsistently. Permeability can either be referred to as the normal passage of water molecules through the sarcolemma, between the intra and extracellular spaces, or as a structural defect in the sarcolemma itself. However it is difficult to separate the contribution of either definition of permeability on the diffusion tensor as multiple microstructural changes are simultaneously occurring. Evans blue dye is commonly used to identify "permeable" fibers in histology of injured skeletal muscle[42]. For example, in an acute cardiotoxin animal model, Evans Blue dye is observed in skeletal muscle and the diffusion profile is less restricted (decreased FA and increased MD)[11]. The choice to represent permeability in our phantoms as randomly deleted walls is meant to represent a decreased overall diffusion environment. This was only observed for the phantoms printed with 20% PBS.

The development of a 3D printed scaffolds to mimic realistic muscle architecture and physiology testing represents a major step forward in the validation and testing of the application of DT-MRI methods to muscle. Early diffusion phantoms were mainly fibrous vegetables[43, 44]. These crude phantoms were used to measure variation in the

direction of the diffusion tensor using different pulse sequences and image processing techniques. More complicated diffusion phantoms have been used to model diffusion in white matter tracts of nerve. Lorenz et al., used simple hydrophilic fibers, like hemp and linen, to study the relationship between diffusion and microstructure[20]. However, they used solid fibers with fluid surrounding it, therefore diffusion measured was purely between fibers and would be inappropriate for skeletal muscle. Yanask and Allison used circular glass capillaries with 23μm, 48μm, and 82μm diameter that were filled with water as a model of nerve tissue to develop a diffusion phantom to test reproducibility of diffusion measurements[21]. An increase in MD and a decrease in FA were found with increasing capillary size, which is consistent with changes in fiber size measured *in vivo* and this study. Similarly, hollow electrospun fibers have been used to simulate diffusion in nerve (~10μm diameter), however it is difficult to control the size, shape and water properties of these fibers as they are being spun[18]. In fairness, these phantoms were not engineered with skeletal muscle in mind.

One complication that we encountered in this study was the inability to separate diffusion from different compartments based on the estimated T_2 of the different tissue compartments. The multi-exponential decay of skeletal muscle has been studied by several groups and the consensus is that the short T_2 component can be attributed to intracellular diffusion and the long T_2 component can be attributed to extracellular diffusion[45, 46]. We hypothesized that the water in the diffusion phantom would have a shorter T_2 decay due to interactions with the polymer substrate, which was observed (phantom T_2 ~200ms vs. free PBS ~480ms at 7T). One possible reason that we did not observe multiexponential decay in the 20% versus 50% PBS phantoms is that we did not

manipulate the composition of intra- and extra-cellular water in a way that would mimic extracellular water *in vivo*. The net effect is that the intra- and extra-cellular water had the same T_2 values, making them inseparable with multi-echo MRI, even though they were physically separated by the printed cell boundary.

This study demonstrated the fabrication and use of a precision-engineered phantom for DT-MRI. These constructs are especially attractive for tissue engineering as they can be used as 3D scaffolds for tissue-engineered muscle, with tight control over the geometry, mechanical properties, porosity, and biomimetic properties. Because muscle has such a strong structure-function relationship, having the ability to control geometry will be essential for designing muscle for future implantation. Furthermore, these scaffolds can be doped with cytokines, can be printed with different material properties (e.g. stiffness and chemical composition), and cells can be directly printed into the phantoms, which can provide more favorable environment for muscle cell proliferation. As these tissue-engineering constructs are developed, they have the potential to be used as tunable *in vitro* models for studying muscle injury and repair, or *in vivo* as a personalized construct for regeneration.

There are several limitations to the phantoms demonstrated in this study. First, the maximum diameter of the phantoms made using this machine is 3.8 mm, which is close to the in-plane voxel dimension of a DTI sequence on a clinical scanner. Therefore, these phantoms would be inappropriate for validating DT-MRI at clinical imaging resolutions. However, with slight modification of the optical system, the DLP 3D printing system should be able to print larger scale phantoms (e.g. 5 cm tall scaffolds). Also, with time, these hydrogel phantoms will begin to change shape due to swelling (~4days), creating

variability in the geometry of the phantom if not scanned relatively soon after fabrication. However, as phantoms take a few seconds to fabricate, it is relatively easy to print phantoms immediately before MRI experiments to minimize the time allowed for samples to become deformed.

The goal of developing these phantoms was originally to validate DT-MRI as a technique to measure different microstructural features of skeletal muscle. Currently, it is believed that DT-MRI is sensitive to changes in fiber size associated with age, pathology, or injury. However, multiple microstructural changes occur simultaneously in muscle, which all have the potential to influence the diffusion of water. We have demonstrated decreasing fiber diameter and increasing water content in the "extracellular" space effect the diffusion signal; decreasing fiber size increases fractional anisotropy and decreases mean diffusivity, increasing extracellular water content increases T_2 relaxation and results in more isotropic diffusion. However, in real muscle, permeability of the sarcolemma, fibrosis, and extracellular changes in fat fraction all contribute to the overall diffusion signal. Therefore, future iterations of these phantoms will investigate how these other structural features of muscle influence the DT-MRI signal individually, and in combination with one another. While advanced simulation environments exist to model diffusion in 3D complex structures, these diffusion phantoms are necessary to translate *in silico* experiments to *in vivo* results.

5.6 ACKNOWLEDGMENTS

The DLP based 3D printing method was supported by grants from the National Institutes of Health (R01EB021857), the National Science Foundation (1547005 and

1644967), and California Institute for Regenerative Medicine (RT3-07899). LRF is supported by grants from the National Institutes of Health (R01MH096100) and National Science Foundation (DBI-1147260, ACI-1550405, ACI-1440412, AA013419-12). SRW is supported by grants from the National Institutes of Health (HD073180) and Department of Defense (PR120576).

Chapter 5 is a reprint of the published article, “A 3D tissue-printing approach for validation of diffusion tensor imaging in skeletal muscle.” Berry DB, You S, Warner J, Chen S, Ward SR. *Tissue Engineering: Part A,* [E pub ahead of print], 2017. The dissertation author was the primary investigator and author of this paper.

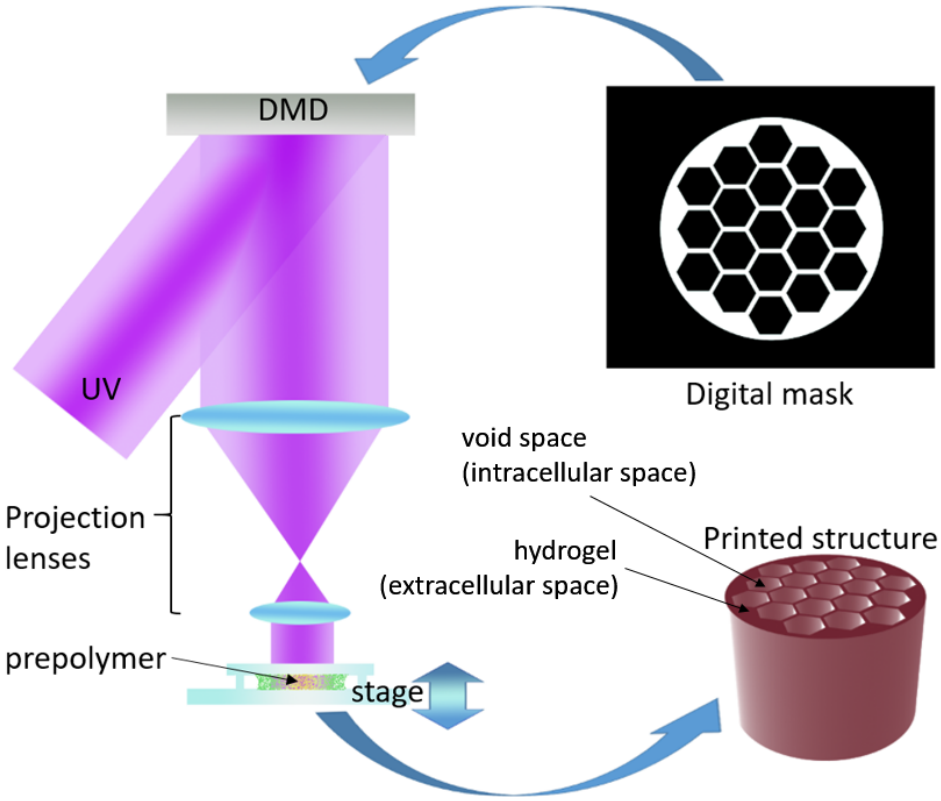

Figure 5-1. DLP based 3D printing system setup. A digital mask of the desired geometry is fed into a digital micromirror device (DMD). Digital masks control the on/off state of each mirror. A collimated UV beam at 365nm wavelength is reflected off of the DMD chip, through a series of projection lenses into the prepolymer solution. Where the UV light strikes, the prepolymer cures into the desired geometry. Excess prepolymer solution is then washed away so that just the printed structure remains. The printed structure is designed to simulate the "extracellular" space in muscle, and the void space in the structure designed to simulate the "intracellular" space in muscle.

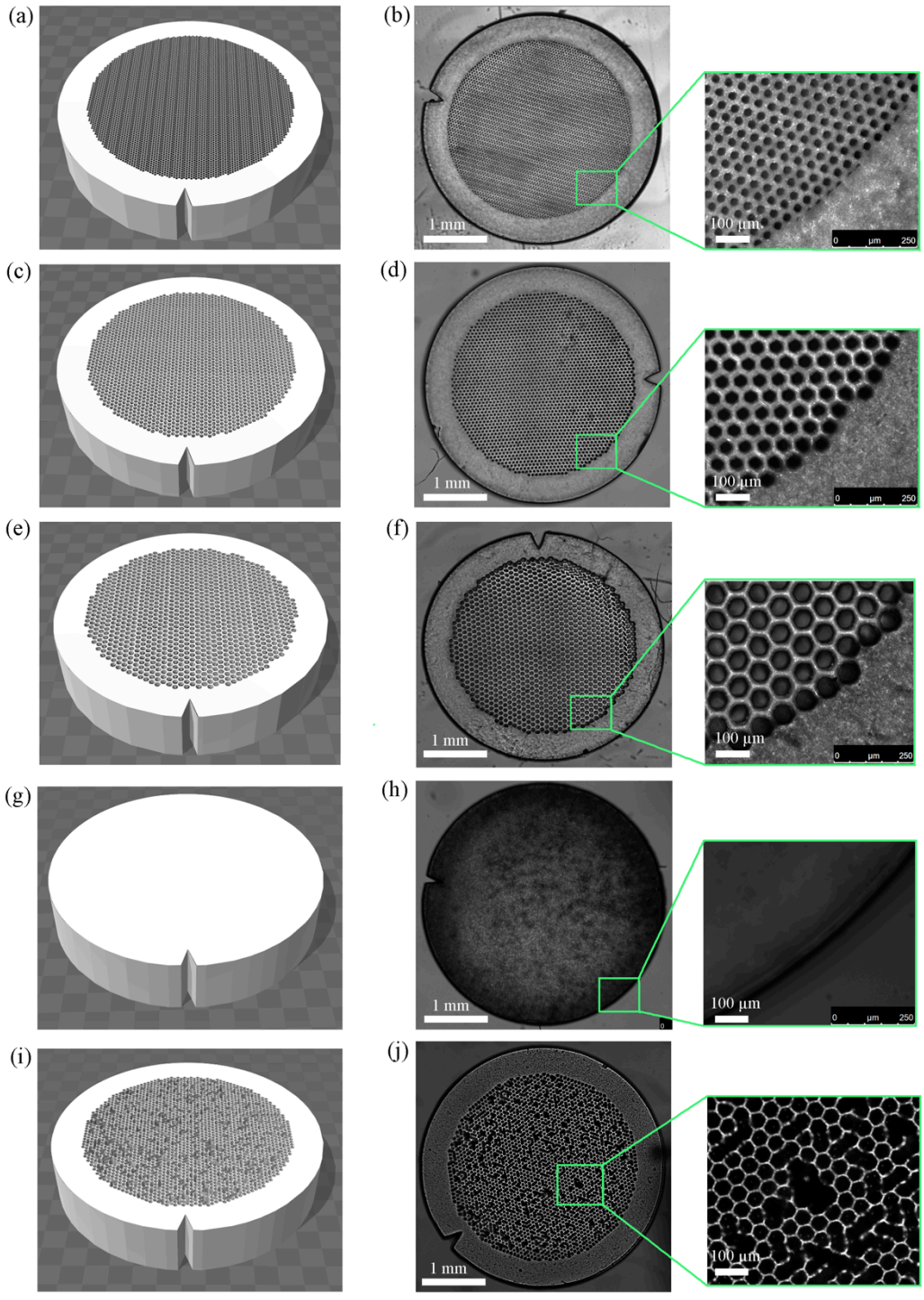

Figure 5-2. Phantom designs (left column) and printed phantoms (right column). (a) & (b): 30µm ideal geometry phantom. (c) & (d): 50µm ideal geometry phantom. (e) & (f): 70µm ideal geometry phantom. (g) & (h): phantom with no feature. (i) & (j): 50um ideal geometry phantom with 40% of walls randomly deleted.

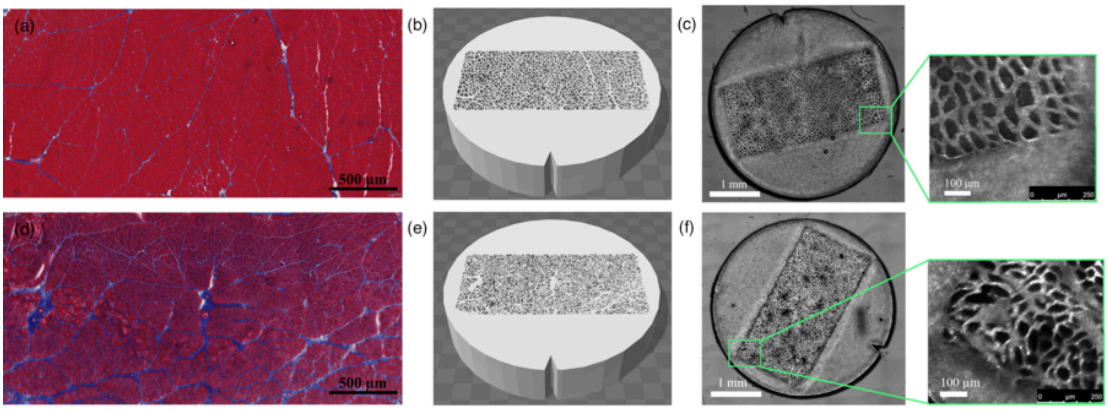

Figure 5-3. Histology informed geometry in 3D printed diffusion phantoms. Histology from control (a) and 30 day denervated (d) skeletal muscle in rat tibias anterior. 3D CAD reconstructions of skeletal muscle geometry for control (b) and denervated (e) samples. Light microscopy of control (c) and denervated (f) 3D printed diffusion phantoms.

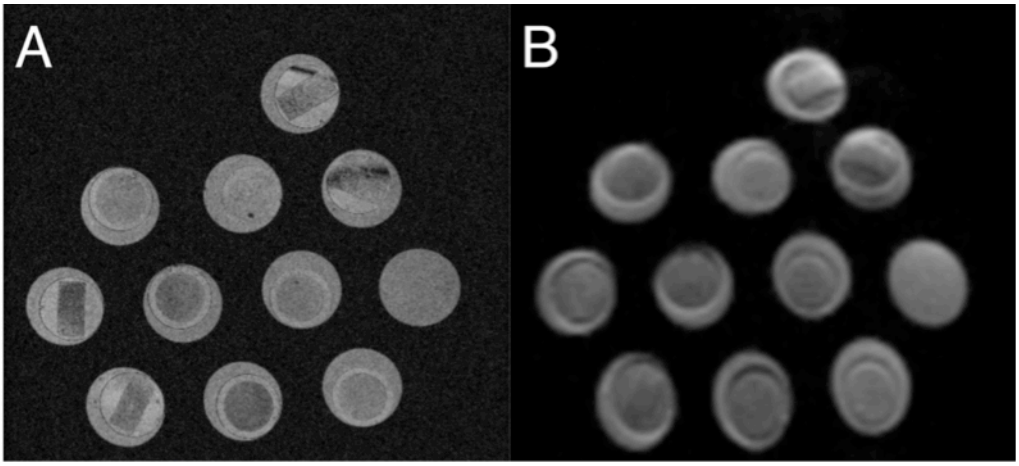

Figure 5-4. 3D FLASH (A) and non-diffusion weighted (b=0) (B) DT-MRI images of the diffusion phantoms.

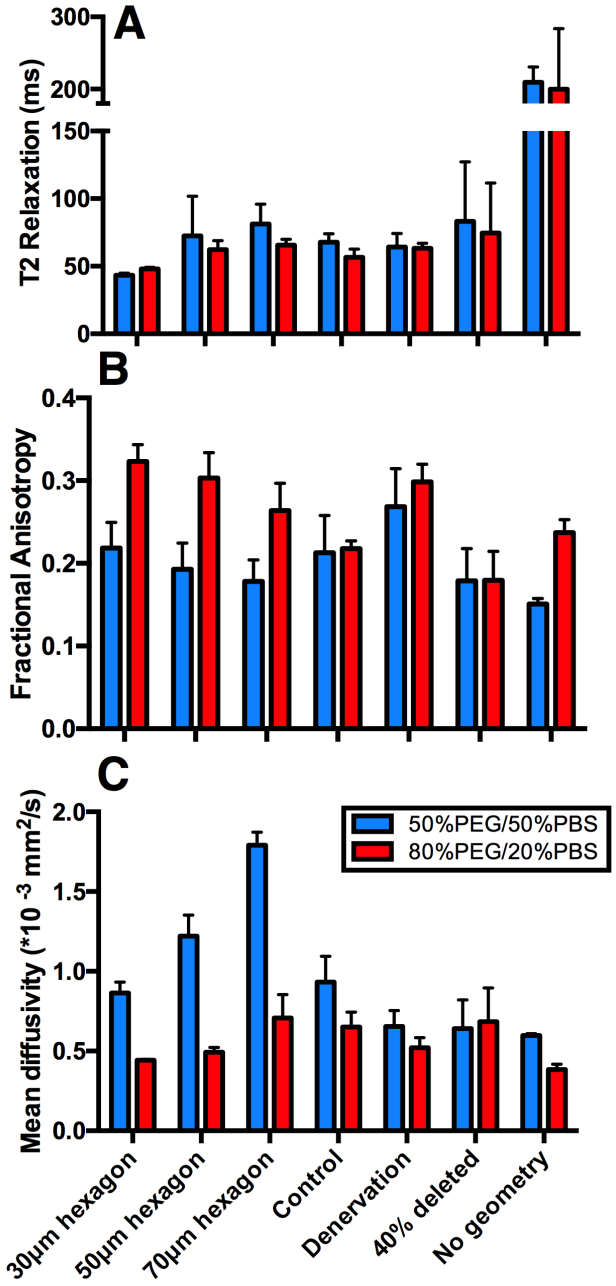

Figure 5-5. The relationships between phantom microstructure and the diffusion tensor. Increasing fractional anisotropy (A) indicates more restricted diffusion. Increasing mean diffusivity (B) indicates increased magnitude of diffusion. Increasing T_2 relaxation (C) indicates increased water content. Mean ± standard deviation is shown for five phantoms with each geometry.

5.7 REFERENCES

1. Adams M, Dolan P, Hutton W. The lumbar spine in backward bending. Spine. 1988;13:1019-1026.

2. Adams MA, Burton K, Bogduk N. The biomechanics of back pain. Elsevier health sciences; 2006.

3. Andersson GB. Epidemiological features of chronic low-back pain. The lancet. 1999;354:581-585.

4. Damon BM. Effects of image noise in muscle diffusion tensor (DT)-MRI assessed using numerical simulations. Magnetic resonance in medicine. 2008;60:934-944.

5. Danielle DOL EJ. Absolute and relativemorbidity burdens attributable to various illnesses andinjuries, U.S. Armed Forces, 2013. MSMR. 2014;21:2-7.

6. Danneels L, Vanderstraeten G, Cambier D, Witvrouw EE, Bourgois J, Danakerts W, De Cuyper HJ. Effects of three different training modalities on the cross sectional area of the lumbar multifidus muscle in patients with chronic low back pain. British journal of sports medicine. 2001;35:186-191.

7. Eng CM, Abrams GD, Smallwood LR, Lieber RL, Ward SR. Muscle geometry affects accuracy of forearm volume determination by magnetic resonance imaging (MRI). Journal of biomechanics. 2007;40:3261-3266.

8. Fieremans E, Lemberskiy G, Veraart J, Sigmund EE, Gyftopoulos S, Novikov DS. In vivo measurement of membrane permeability and myofiber size in human muscle using time-dependent diffusion tensor imaging and the random permeable barrier model. NMR in biomedicine. 2016;

9. Gans C. Fiber architecture and muscle function. Exercise and sport sciences reviews. 1982;10:160-207.

10. Hubbard PL, Zhou FL, Eichhorn SJ, Parker GJ. Biomimetic phantom for the validation of diffusion magnetic resonance imaging. Magnetic resonance in medicine. 2015;73:299-305.

11. Jeong EK, Kim SE, Parker DL. High-resolution diffusion-weighted 3D MRI, using diffusion-weighted driven-equilibrium (DW-DE) and multishot segmented 3D-SSFP without navigator echoes. Magnetic resonance in medicine. 2003;50:821-829.

12. Knox J, Orchowski J, Scher DL, Owens BD, Burks R, Belmont PJ. The incidence of low back pain in active duty United States military service members. Spine. 2011;36:1492-1500.

13. Lavdas I, Behan KC, Papadaki A, McRobbie DW, Aboagye EO. A phantom for diffusion-weighted MRI (DW-MRI). Journal of Magnetic Resonance Imaging. 2013;38:173-179.

14. Le Bihan D, Mangin JF, Poupon C, Clark CA, Pappata S, Molko N, Chabriat H. Diffusion tensor imaging: concepts and applications. Journal of magnetic resonance imaging. 2001;13:534-546.

15. Lieber RL, Ward SR. Cellular mechanisms of tissue fibrosis. 4. Structural and functional consequences of skeletal muscle fibrosis. American Journal of Physiology-Cell Physiology. 2013;305:C241-C252.

16. Lieber RL, Ward SR. Skeletal muscle design to meet functional demands. Philosophical Transactions of the Royal Society B: Biological Sciences. 2011;366:1466-1476.

17. Lorenz R, Bellemann M, Hennig J, Il'yasov K. Anisotropic phantoms for quantitative diffusion tensor imaging and fiber-tracking validation. Applied Magnetic Resonance. 2008;33:419-429.

18. Luoma K, Riihimäki H, Luukkonen R, Raininko R, Viikari-Juntura E, Lamminen A. Low back pain in relation to lumbar disc degeneration. Spine. 2000;25:487-492.

19. Merboldt K-D, Hanicke W, Frahm J. Self-diffusion NMR imaging using stimulated echoes. Journal of Magnetic Resonance (1969). 1985;64:479-486.

20. Minamoto VB, Hulst JB, Lim M, Peace WJ, Bremner SN, Ward SR, Lieber RL. Increased efficacy and decreased systemic-effects of botulinum toxin A injection after active or passive muscle manipulation. Developmental Medicine & Child Neurology. 2007;49:907-914.

21. Oudeman J, Nederveen AJ, Strijkers GJ, Maas M, Luijten PR, Froeling M. Techniques and applications of skeletal muscle diffusion tensor imaging: A review. Journal of Magnetic Resonance Imaging. 2015;

22. Perrin M, Poupon C, Rieul B, Leroux P, Constantinesco A, Mangin JF, Lebihan D. Validation of q-ball imaging with a diffusion fibre-crossing phantom on a clinical scanner. Philosophical Transactions of the Royal Society of London B: Biological Sciences. 2005;360:881-891.

23. Poupon C, Rieul B, Kezele I, Perrin M, Poupon F, Mangin JF. New diffusion phantoms dedicated to the study and validation of high-angular-resolution diffusion imaging (HARDI) models. Magnetic Resonance in Medicine. 2008;60:1276-1283.

24. Rockel C, Noseworthy MD. An exploration of diffusion tensor eigenvector variability within human calf muscles. Journal of Magnetic Resonance Imaging. 2016;43:190-202.

25. Rodriguez-Soto AE, Berry DB, Jaworski R, Gombatto SP, Shahidi B, Palombo L, Chung C, Jensen A, Kelly KR, Ward SR. The effect of training on lumbar spine posture and intervertebral disc degeneration in active-duty Marines. Ergonomics. 2016;1-9.

26. Rodriguez-Soto AE, Berry DB, Palombo L, Valaik E, Kelly KR, Ward SR. The Effect of Load Magnitude and Distribution on Lumbar Spine Posture in Active-Duty Marines. Spine. 2016;

27. Rodriguez-Soto AE, Jaworski R, Jensen A, Niederberger B, Hargens AR, Frank LR, Kelly KR, Ward SR. Effect of load carriage on lumbar spine kinematics. Spine. 2013;38:E783-791.

28. Schoenfeld AJ, Nelson JH, Burks R, Belmont Jr PJ. Incidence and risk factors for lumbar degenerative disc disease in the United States military 1999-2008. Military medicine. 2011;176:1320-1324.

29. Shirazi-Adl A. Biomechanics of the lumbar spine in sagittal/lateral moments. Spine. 1994;19:2407-2414.

30. Shirazi-Adl A, El-Rich M, Pop D, Parnianpour M. Spinal muscle forces, internal loads and stability in standing under various postures and loads—application of kinematics-based algorithm. European spine journal. 2005;14:381-392.

31. Sigmund EE, Song Y-Q. Multiple echo diffusion tensor acquisition technique. Magnetic resonance imaging. 2006;24:7-18.

32. Tanner JE. Use of the stimulated echo in NMR diffusion studies. The Journal of Chemical Physics. 1970;52:2523-2526.

33. Teruel JR, Cho GY, Moccaldi R, Goa PE, Bathen TF, Feiweier T, Kim SG, Moy L, Sigmund EE. Stimulated echo diffusion tensor imaging (STEAM-DTI) with varying diffusion times as a probe of breast tissue. Journal of Magnetic Resonance Imaging. 2017;45:84-93.

34. Tournier J, Calamante F, Connelly A. Resolving crossing fibres using constrained spherical deconvolution: validation using DWI phantom data. Proceedings of the 15th Annual Meeting of ISMRM. 2007.

35. Trudeau J, Dixon WT, Hawkins J. The effect of inhomogeneous sample susceptibility on measured diffusion anisotropy using NMR imaging. Journal of Magnetic Resonance, Series B. 1995;108:22-30.

36. Waterman BR, Belmont PJ, Schoenfeld AJ. Low back pain in the United States: incidence and risk factors for presentation in the emergency setting. The spine journal. 2012;12:63-70.

37. Yanasak N, Allison J. Use of capillaries in the construction of an MRI phantom for the assessment of diffusion tensor imaging: demonstration of performance. Magnetic resonance imaging. 2006;24:1349-1361.

CHAPTER 6: CONCLUSIONS

The work presented in this dissertation provides a theoretical and experimental basis for understanding the complex relationships between diffusion tensor imaging (DTI), muscle microstructure, and functional lumbar spine postures in a highly active population. Using 0.6T upright and 3T supine MRI, the capacity of erector spinae fractional anisotropy to predict lumbar posture in active-duty Marines was established. To better understand the physical origins of fractional anisotropy, the relationship between muscle microstructure and the diffusion tensor was systematically evaluated using sophisticated *in silico* and *in vitro* techniques. These studies support previous assumptions that the diffusion tensor is related to muscle fiber size. However, these studies have quantitatively demonstrated that other microstructural elements of muscle contribute to the overall diffusion signal, and must be taken into account when interpreting diffusion results. Additionally, these experiments demonstrate the differential effects of muscle microstructure on the diffusion tensor when measured with single- and multi-echo diffusion tensor imaging pulse sequences.

6.1 Lumbar spine postures that put Marines at risk for injury

Low back pain is a common musculoskeletal complaint, affecting 70%-85% of the population at any given time and is a particularly large problem in the military [3, 5]. The incidence of low back pain in military members is 29 times greater than in civilians and leads to more medical encounters than any other medical condition [12, 36]. Low back pain does not affect all branches of the military equally; development of low back pain is

highest for members in the Marine Corps [12]. External load carriage and wearing body armor for long durations of time during training and in combat have been identified as some of the factors associated with low back pain development in Marines [18, 28].

The lumbar spine experiences constant axial loading and shear force from the upper trunk when a person is upright. The intervertebral disc is responsible for the majority of axial load transmission and the facet joint is responsible for protecting the intervertebral segment from anterior shear force [2]. However, both of these elements do undergo axial and shear loading to some extent [1, 29]. When an external load is applied, postural adaptations of the spine result in relative changes in the magnitude and direction of forces being transmitted throughout the lumbar spine, which have the potential to result in injury [2, 30]. Repetitive loading of the intervertebral disc and facet joint may result in the development of low back pain. Therefore, the posture of the spine under operationally relevant loads is of interest to the military.

Previous studies have investigated the effect of load magnitude, load distribution, temporal effects of load carriage and training on how to carry load on lumbar spine posture [25-27]. The lumbar spine reacts to load carriage of operationally relevant magnitudes (50.8kg) by moving into forward flexion and decreasing lordosis [27]. These changes occur immediately and are not exacerbated by time. However, changing the distribution of load from a posteriorly biased configuration, to more evenly distributed anterior/posterior about a person's center of mass can reverse these changes [26].

In chapter 2, large position dependent changes in global lumbar spine posture were found for lumbosacral extension, lumbar lordosis, and sacral slope in simulated, operationally relevant positions. The magnitude of these changes was equal to if not

greater than postural responses to heavy loading when Marines went into sitting or prone on elbows positions. Interestingly, the decrease in lumbar lordosis from standing unloaded to sitting with body armor observed was more than double (30°) than that measured when Marines were standing with 50.8kg of load (13°) when compared to standing unloaded [27]. Additionally, level dependent changes in intervertebral angle resulting from positional changes are commensurate with those observed resulting from heavy load, especially at the lower lumbar levels. The findings from chapter 2 support that operationally relevant positions cause large postural perturbations in the lumbar spine, which has the potential to alter the pattern of load transmission throughout the lumbar spine and may be related to the abnormally high rates of reported low back pain. These findings were made using a novel application of upright MRI to measure operationally relevant postures, which previously had not been described.

6.2 Relating lumbar posture to muscle structure

Lumbar posture, lumbar muscle structure, and intervertebral disc health are all well studied individually, and are known to influence one another. However the combination of all three have not been quantitatively studied. Chapter 3 was thus completed to assess the predictive capacity of lumbar muscle structure and intervertebral disc degeneration on lumbar posture in a variety of relevant, operational positions. The capacity of fractional anisotropy of the erector spinae, a measure of muscle microstructure, to significantly predict lumbar posture and not muscle volume suggests that muscle quality, not quantity may be a better determinant of muscle posture. In chapters 4 and 5, the relationship between the diffusion tensor and fiber size was

established; fractional anisotropy is nonlinearly, inversely related to fiber size, and is relatively insensitive to fibers that are greater than 60μm in diameter. As fiber size and isometric force generating capacity of muscle fibers are directly related [20], it follows that fractional anisotropy and force generating capacity are also inversely related. Therefore, when interpreting the main finding in chapter 3, smaller, weaker muscle fibers in the erector spinae resulted in decreased lordosis, decreased extension and decreased pelvic tilt in the lumbar spine in a highly active population.

6.3 Physiologic interpretation of the diffusion tensor

Histology is the gold standard tool to study muscle microstructure. This tool is highly invasive, not conducive for serially monitoring muscle health, is semi-quantitative, and often difficult to extrapolate to the entire muscle. Many studies have used diffusion tensor imaging to measure changes in diffusion in injured skeletal muscle, and have theorized how microstructure relates to the diffusion model [21]. However these relationships have never been explicitly tested nor carefully validated, and therefore are a current focus of DTI research. In chapters 4 and 5, we assessed the direct relationship between microstructure and anisotropic diffusion in skeletal muscle in a series of highly controlled experiments. These experiments are significant because they are the fundamental experiments missing from the literature that describe the relationship between diffusion physics and muscle physiology.

By identifying key features of muscle microstructure, the models in chapters 4 and 5 were developed. Edema was identified as a feature of muscle microstructure that has the potential to complicate the resultant diffusion tensor. Multi-echo DTI was

implemented to attempt to remove the complexity of a diffusion signal arising from intra-cellular and extra-cellular compartments within muscle as it utilizes the differences in magnetic relaxation properties of water in the different compartments. This was accomplished *in silico* and failed *in vitro*, possibly due to difficulties in controlling magnetic properties of phosphate buffered saline inside and outside of the phantom material itself. Additionally, the inability to separate intra and extra-cellular diffusion in the diffusion phantom may be an issue relating to signal-to-noise, however we did not calculate the minimum required signal-to-noise ration required to separate intra- and extra-cellular diffusion.

The most significant contribution to the literature concerning diffusion tensor imaging is the quantitative validation of predictive capacity of muscle microstructure features using single-echo and multi-echo DTI pulse sequences in chapter 4. Fractional anisotropy was validated as being an important predictor of fiber diameter in idealized, and histology informed models of skeletal muscle. Additionally, the plateau effect of the diffusion tensor when muscle fibers are greater than 60μm has not been previously described in the literature. However, 60μm should not be set as a standard across all diffusion experiments. The plateau at this fiber diameter is likely representative of the duration and separation of the diffusion gradients, which were relatively short in this study. However, these same exact diffusion models can be resimulated under a variety of diffusion pulse sequence parameters, which is one of the advantages of performing *in silico* modeling before *in vivo* imaging. The techniques described in aims 4 and 5 can be used to optimize diffusion pulse sequence parameters to be most sensitive to microstructural features that are of interest.

6.4 Advancements in diffusion phantom fabrication

Early diffusion phantoms were mainly fibrous vegetables such as celery [11, 35]. The goals of these early studies were to measure variation in the direction of the diffusion tensor using different diffusion pulse sequences and data processing analysis. As diffusion tensor imaging became more popular, phantoms used for diffusion did not advance as quickly as the technique. As recently as 10 years ago, vegetables such as asparagus were still being used as simple diffusion phantoms [31]. Early, non-vegetable diffusion phantoms were first designed to model diffusion in white matter tracts. Early phantoms for these models were based on interwoven textile fibers [17, 22, 23], non-biologic capillaries [34, 37], or biological tissues themselves [34]. These phantoms all provide little *a priori* control over microstructure organization, size, and magnetic properties. In 2013, Lavadas developed a phantom with variable relaxation and diffusion coefficients, but with no microstructural restrictions, which are now being sold commercially [13]. To date, the best diffusion phantom uses electrospinning to fabricate fibers with nerve size geometry (~10μm) [10]. However these techniques do not allow for precise control over geometry, nor T2 relaxation. The diffusion phantoms developed in chapter 4 represent the first diffusion phantoms that are designed for validation of diffusion tensor imaging that allow for precise tunable geometry at nanometer scale resolution, and control of the magnetic properties of the phantom itself. These phantoms have the potential to be used to validate pulse sequences, compare diffusion measurements across MRI scanners, and have potential to function as tissue engineered scaffolds for muscle regeneration after injury.

6.5 Challenges in diffusion tensor imaging

Diffusion tensor imaging is inherently difficult in skeletal muscle. Muscle has a short T2 relaxation coefficient, often shorter than the echo time in many preprogrammed DTI pulse sequences [21]. Since the T2 signal decays exponentially, minimizing echo time is required in order to collect data with an adequate signal to noise ratio. Shortening the echo time in a pulse sequence is complicated by many factors, including hardware limitations, the duration of the diffusion gradients, and spatially encoding the diffusion signal with echo planar imaging. It is possible to decrease echo time by shortening the duration or separation of the diffusion gradients, however this limits the effective diffusion length that can be probed during an experiment. One solution is to use a stimulated echo diffusion tensor imaging technique, which allows for sampling long diffusion times without compromising echo time by temporarily storing transverse magnetization in the longitudinal plane to prevent decay, then recovering it back into the transverse plane [19, 32, 33]. This technique is often used to sample diffusion at a variety of diffusion lengths, which can be used to approximate fiber size [8]. However this technique has not been validated in complex models of muscle injury or pathology. Another technique that can be used to decrease echo time is to split up collection of k-space MR data into several excitations, referred to as multi-shot echo planar imaging. The main drawback for this technique is that total imaging time scales with the number of excitations collected. Finally, across nearly all diffusion experiments, there is a lack of validation of microstructural measurements with the gold standard, histology. Future

studies must perform tissue specific histology in order to reconcile diffusion measurements with actual muscle microstructure.

6.6 Limitations

There are several limitations in this study. In chapters 2 and 3, we did not selectively recruit Marines with low back pain, IVD degeneration, and the overall age of the cohort was relatively young. From an older cohort, displaying more pathology, we might expect to see a more severe presentation of muscle atrophy, fatty infiltration, disc degeneration, and different degrees of lumbar posture. The predictive capacity of muscle volume on lumbar lordosis may become more significant when muscle volume loss associated with age and pathology is present; the spine may adopt stereotypic posture when there is little to no contractile tissue available to support it. Therefore, it is necessary to interpret the findings of these studies in the context of a young, highly active population, with relatively little pathology. In chapter 4, we did not evaluate the effect of varying diffusion pulse sequence parameters and signal-to-noise ratio. As described above, the diffusion distances probed in this study were relatively small, and were likely not in the range of the radial diffusion limit. Other studies have explored the relationship between diffusion time and radial diffusivity to estimate muscle fiber diameters. However, the goal of these studies was not to separate and measure diffusion from the intra- and extra-cellular compartments of muscle. One of abilities of DifSim is to simulate diffusion experiments with noise. The effect of noise on the diffusion tensor in skeletal muscle has been previously studied [4, 14, 24]. The major findings from these studies indicate that fractional anisotropy increases as signal to noise ratio increases, and suggest

implementing a minimum signal to noise ratio in diffusion experiments of muscle at 25 [4]. However these findings were determined for normal, single-echo DTI pulse sequences. The minimum required threshold in order to accurately estimate diffusion from the intra- and extra-cellular compartments in skeletal muscle needs to be further explored *in silico* and validated *in vivo*. Evidence of this was observed in chapter 5, where diffusion inside and outside of the diffusion phantom was unable to be separated, even though signal to noise ratio was 33.7. However, this also may have been complicated by the use of PBS both inside the phantom material and in the pores of the phantom. An additional limit of chapter 5 is the small size of the diffusion phantoms (3.8mm diameter). However, by changing the optical setup and modulating the z-axis of the fabrication stage, it is theoretically possible to make diffusion phantoms up to 5cm tall.

6.7 Summary

The major outcome of chapter 2 is the description of a stereotypic set of postural adaptations that a male Marine undergoes during functional tasks, which have the potential to impair performance in training or in combat. In chapter 3, a quantitative connection between lumbar posture and muscle microstructure was established. While changes in muscle structure and lumbar posture have been well studied individually, chapter 3 is the first study to provide a quantitative link between the two. The outcomes of chapters 4 and 5 are significant because they provide a framework into the complex relationships between microstructure and diffusion in muscle. A more comprehensive understanding of this tool has the potential to yield a quantitative tool for clinicians and researchers to non-invasively quantify muscle microstructure to determine diagnosis,

disease progression, and treatment effectiveness in a wide range of patient's muscular disorders including muscular dystrophy, myositis, and orthopaedic patients with suspicion of degenerative muscle wasting.

6.8 References

1. Andersson GB. Epidemiological features of chronic low-back pain. The lancet. 1999;354:581-585.

2. Danielle DOL EJ. Absolute and relativemorbidity burdens attributable to various illnesses andinjuries, U.S. Armed Forces, 2013. MSMR. 2014;21:2-7.

3. Knox J, Orchowski J, Scher DL, Owens BD, Burks R, Belmont PJ. The incidence of low back pain in active duty United States military service members. Spine. 2011;36:1492-1500.

4. Waterman BR, Belmont PJ, Schoenfeld AJ. Low back pain in the United States: incidence and risk factors for presentation in the emergency setting. The spine journal. 2012;12:63-70.

5. Schoenfeld AJ, Nelson JH, Burks R, Belmont Jr PJ. Incidence and risk factors for lumbar degenerative disc disease in the United States military 1999-2008. Military medicine. 2011;176:1320-1324.

6. Luoma K, Riihimäki H, Luukkonen R, Raininko R, Viikari-Juntura E, Lamminen A. Low back pain in relation to lumbar disc degeneration. Spine. 2000;25:487-492.

7. Adams MA, Burton K, Bogduk N. The biomechanics of back pain: Elsevier health sciences; 2006.

8. Shirazi-Adl A. Biomechanics of the lumbar spine in sagittal/lateral moments. Spine. 1994;19:2407-2414.

9. Adams M, Dolan P, Hutton W. The lumbar spine in backward bending. Spine. 1988;13:1019-1026.

10. Shirazi-Adl A, El-Rich M, Pop D, Parnianpour M. Spinal muscle forces, internal loads and stability in standing under various postures and loads—application of kinematics-based algorithm. European spine journal. 2005;14:381-392.

11. Rodriguez-Soto AE, Berry DB, Jaworski R, Gombatto SP, Shahidi B, Palombo L, Chung C, Jensen A, Kelly KR, Ward SR. The effect of training on lumbar spine posture and intervertebral disc degeneration in active-duty Marines. Ergonomics. 2016:1-9.

12. Rodriguez-Soto AE, Berry DB, Palombo L, Valaik E, Kelly KR, Ward SR. The Effect of Load Magnitude and Distribution on Lumbar Spine Posture in Active-Duty Marines. Spine. 2016.

13. Rodriguez-Soto AE, Jaworski R, Jensen A, Niederberger B, Hargens AR, Frank LR, Kelly KR, Ward SR. Effect of load carriage on lumbar spine kinematics. Spine. 2013;38:E783-791.

14. Minamoto VB, Hulst JB, Lim M, Peace WJ, Bremner SN, Ward SR, Lieber RL. Increased efficacy and decreased systemic-effects of botulinum toxin A injection after active or passive muscle manipulation. Developmental Medicine & Child Neurology. 2007;49:907-914.

15. Oudeman J, Nederveen AJ, Strijkers GJ, Maas M, Luijten PR, Froeling M. Techniques and applications of skeletal muscle diffusion tensor imaging: A review. Journal of Magnetic Resonance Imaging. 2015.

16. Jeong EK, Kim SE, Parker DL. High-resolution diffusion-weighted 3D MRI, using diffusion-weighted driven-equilibrium (DW-DE) and multishot segmented 3D-SSFP without navigator echoes. Magnetic resonance in medicine. 2003;50:821-829.

17. Trudeau J, Dixon WT, Hawkins J. The effect of inhomogeneous sample susceptibility on measured diffusion anisotropy using NMR imaging. Journal of Magnetic Resonance, Series B. 1995;108:22-30.

18. Sigmund EE, Song Y-Q. Multiple echo diffusion tensor acquisition technique. Magnetic resonance imaging. 2006;24:7-18.

19. Lorenz R, Bellemann M, Hennig J, Il'yasov K. Anisotropic phantoms for quantitative diffusion tensor imaging and fiber-tracking validation. Applied Magnetic Resonance. 2008;33:419-429.

20. Perrin M, Poupon C, Rieul B, Leroux P, Constantinesco A, Mangin JF, Lebihan D. Validation of q-ball imaging with a diffusion fibre-crossing phantom on a clinical scanner. Philosophical Transactions of the Royal Society of London B: Biological Sciences. 2005;360:881-891.

21. Poupon C, Rieul B, Kezele I, Perrin M, Poupon F, Mangin JF. New diffusion phantoms dedicated to the study and validation of high-angular-resolution

diffusion imaging (HARDI) models. Magnetic Resonance in Medicine. 2008;60:1276-1283.

22. Yanasak N, Allison J. Use of capillaries in the construction of an MRI phantom for the assessment of diffusion tensor imaging: demonstration of performance. Magnetic resonance imaging. 2006;24:1349-1361.

23. Tournier J, Calamante F, Connelly A. Resolving crossing fibres using constrained spherical deconvolution: validation using DWI phantom data. Proceedings of the 15th Annual Meeting of ISMRM. Vol 9022007.

24. Lavdas I, Behan KC, Papadaki A, McRobbie DW, Aboagye EO. A phantom for diffusion-weighted MRI (DW-MRI). Journal of Magnetic Resonance Imaging. 2013;38:173-179.

25. Hubbard PL, Zhou FL, Eichhorn SJ, Parker GJ. Biomimetic phantom for the validation of diffusion magnetic resonance imaging. Magnetic resonance in medicine. 2015;73:299-305.

26. Teruel JR, Cho GY, Moccaldi R, Goa PE, Bathen TF, Feiweier T, Kim SG, Moy L, Sigmund EE. Stimulated echo diffusion tensor imaging (STEAM-DTI) with varying diffusion times as a probe of breast tissue. Journal of Magnetic Resonance Imaging. 2017;45:84-93.

27. Merboldt K-D, Hanicke W, Frahm J. Self-diffusion NMR imaging using stimulated echoes. Journal of Magnetic Resonance (1969). 1985;64:479-486.

28. Tanner JE. Use of the stimulated echo in NMR diffusion studies. The Journal of Chemical Physics. 1970;52:2523-2526.

29. Fieremans E, Lemberskiy G, Veraart J, Sigmund EE, Gyftopoulos S, Novikov DS. In vivo measurement of membrane permeability and myofiber size in human muscle using time-dependent diffusion tensor imaging and the random permeable barrier model. NMR in biomedicine. 2016.

30. Damon BM. Effects of image noise in muscle diffusion tensor (DT)-MRI assessed using numerical simulations. Magnetic resonance in medicine. 2008;60:934-944.

31. Le Bihan D, Mangin JF, Poupon C, Clark CA, Pappata S, Molko N, Chabriat H. Diffusion tensor imaging: concepts and applications. Journal of magnetic resonance imaging. 2001;13:534-546.

32. Rockel C, Noseworthy MD. An exploration of diffusion tensor eigenvector variability within human calf muscles. Journal of Magnetic Resonance Imaging. 2016;43:190-202.